

Functional Extension of Atmospheric Radar with Digital Receiver Array

Koji Nishimura

September, 2006

Abstract

High-resolution radar observation is of great importance for advanced analysis of the dynamical system of the atmosphere. In this thesis, studies are presented on functional extension over high-gain atmospheric radars using a multistatic Doppler observation technique realized by digital receiver arrays. Conventional monostatic atmospheric radar, which consists of one high-gain array, has a limitation in its spatial resolution of 3D wind velocity field estimation. Since radar can only measure the line-of-sight Doppler velocity of the atmospheric field, it is necessary for the radar to spot several separate volumes of the atmosphere to estimate the mean wind velocity under an assumption of spatial uniformity of the field. Multistatic radar, which is composed of one high-gain radar and several passive receivers, can observe multiple line-of-sight velocities of a single minimum resolution volume simultaneously. With this method, a three-dimensional velocity vector can be thus retrieved without assuming a spatial uniformity between separate scattering volumes. To realize a multistatic atmospheric radar system, post-set beam steering technique using digital receiver array is practically essential to hold wide coverage of observable region. For atmospheric radar, strong ground clutters is a persistent problem that degrades an estimation of the wind velocity. An adaptive technique to form a spatial filter for canceling the clutter can reduce the affection on an estimate of the wind velocity. First, an adaptive clutter rejection technique under a partially adaptive array system with the MU radar is demonstrated. On a multistatic system with a small low-gain receiver array, conventional frequency spectral processing for rejecting a clutter leads to a bias in the estimate of a wind velocity spectrum since it has a much higher ground clutter level compared to a high-gain radar. A technical fusion of a post-set beam steering to follow the transmitted pulse wave and an adaptive clutter rejection is introduced. In conventional atmospheric radar applications, antenna arrays were constructed with a periodical arrangement due to its low sidelobe gain. For adaptive beamforming arrays, an arrangement of antennas must be optimally designed to avoid having grating-lobes even if the main-lobe is largely tilted off zenith. For a two-dimensional planer application, however, practical criteria to design an array have not been proposed and due to its large number of degrees of freedom. In this study, a systematic method based on a trial-and-error algorithm and an evaluation criterion for the beam pattern is presented. Extending this algorithm, a novel fast optimization method is proposed employing potential functions around antennas based on a mathematical interpretation of a beam-space mean-square sidelobe evaluation function. Introducing these techniques, we have successfully performed a series of multistatic observations of the troposphere at the Equatorial Atmosphere Radar, West Sumatra, Indonesia. Resulting 3D wind vector fields with a horizontal samples of about a 1000 m interval exhibit existing irregularity conventionally ignored.

Acknowledgments

The opportunity to work on this study is provided by my supervisor Professor T. Sato. I am above all indebted to him for his patience, constant guidance and support without which this thesis should not have accomplished.

I would also like to express my grateful thanks to Drs. S. Norimatsu, T. Matsuo and T. Sakamoto for their consistent interest and valuable comments given at intramural meetings in our laboratory.

I was helped directly or indirectly by many colleagues. Especially, I would like to express my sincere thanks to Messrs. K. Fukuo, E. Gotoh and T. Harada for their theoretical and experimental work on the multistatic atmospheric radar, and Mr. K. Kamio for his work on adaptive clutter rejection algorithms.

For the observations, I owed some pivotal software for digital receivers to Dr. J. Hagen, Arecibo Observatory. Also, the observations were supported in software by Mr. Y. Osawa, and in hardware by Mr. S. Sugitani. I would like to express my gratitude to them for their excellent work.

This thesis is examined by Professors S. Fukao and T. Tsuda, from a technical point of view, to be finalized. I am deeply grateful to them for their insightful advices and productive comments.

This work was partly supported by the 21st century center of excellence (COE) program (Grant No. 14213201).

Contents

1	General Introduction	1
1.1	Adaptive Array Techniques for Undesired Signal Cancellation	1
1.2	Adaptive Array Processing for Atmospheric Radar	5
1.3	Early Study on Bistatic/Multistatic Observation for 3D Wind Field	8
1.4	High-Resolution Doppler Observation at the Equatorial Region	9
1.5	Contents of This Thesis	14
2	Multistatic Radar Technique	15
2.1	Introduction	15
2.2	Doppler Velocity Estimation	15
2.3	Multi-Doppler Observation Technique	18
2.4	Multistatic Observation Technique	20
2.4.1	Principle	20
2.4.2	Shape of targets	23
3	Adaptive Clutter Rejection	29
3.1	Introduction	29
3.2	Proposed Algorithm	30
3.3	Application to High Gain Arrays	31
3.4	Observations	33
3.5	Clutter Suppression Using Real Data	35
3.6	Considerations on the Constraints	37
3.7	Suppression of Clutter from Moving Targets	39
3.8	Averaging of the Covariance Matrix	42
3.9	Summary	43
4	Arrangement of Antenna Array	47
4.1	Introduction	47
4.2	System Definition	49
4.3	Evaluation Function	51
4.4	An Optimization Algorithm in Beam Space	52

4.5	Fast Evaluation Algorithm based on Potential Function	54
4.6	Resulting Arrays by the Trial-end-Error Algorithm	57
4.7	Optimization by the Steepest Descent Method	59
4.8	Summary	60
5	Multistatic Observation of the Atmosphere	67
5.1	Settings of Receiver Arrays	67
5.2	Design of Digital Receivers	71
5.3	Observational scheme	75
5.4	Post-observational signal processing	76
	5.4.1 Pre-processing	76
	5.4.2 Array Signal Processing	78
5.5	Resulting 3D wind field	80
5.6	Observation for CPEA-II in 2005	89
5.7	Summary	93
6	Concluding Remarks	95

List of Tables

3.1	Basic parameter of the MU radar.	33
5.1	System parameters for digital receivers.	74
5.2	Observational modes of EAR. NCOH, NICOH and NFFT are the parameters used in the EAR side. (IPP: Inter-Pulse Period, PL: Pulse Length, SPL: Sub-Pulse Length, NCOH: Number of Coherent Integration, NICOH: Number of Incoherent Integration, NFFT: FFT data length)	75
5.3	The number of antennas at each site for observations in 2005.	91
5.4	Observational modes in 2005.	92

List of Figures

1.1	System model of an array consisting of N antennas. The output s is constructed by a linear sum of all the signals from s_1 to s_N with adaptively controlled coefficients from w_1 to w_N	2
1.2	A typical response of the MVDR algorithm. An interference arrives from of the direction of 30° with a power of 30 dB compared to the noise level.	3
1.3	Geometrical representation of MVDR algorithm illustrated in two-dimensional space. Dashed-dot lines show the contours of the evaluation function. The solid line shows the constraint plane orthogonal to \mathbf{c} . The MVDR solution points at which the gradient of the evaluation function matches $\gamma\mathbf{c}$ where γ is a scalar.	4
1.4	Comparison of the resolving power of the different methods used in range profile estimation as a function of SNR from 0 to 30 dB. The normalized brightness is represented for two infinitely thin layers separated by 75 m. .	6
1.5	Brightness distribution average over the velocity range $\pm 1 \text{ ms}^{-1}$ within $\pm 4^\circ$ above the middle and upper atmosphere (MU) radar wite at eight arbitrary altitudes. Red colors correspond to highest brightness. As shown, images on the left and right of each pair were obtained using Fourier-based and Capon imaging techniques, respectively. Notice that Capon's method seems to exhibit better resolution than the Fourier-based method. (Palmer, 1998)	7
1.6	A brightness distribution along the range direction using a five frequency FDI imaging with Capon's method. The beam direction is (0,0). The x-axis is time in minute.	8
1.7	East-west vertical slice through weak convective cell. Vectors show slice parallel wind vectors calculated using CP-2 and bistatic data only (left) and CP-2 and MHR data only (right). Shading in both panels is CP-2-measured reflectivity. Updraft is visible in both calculations at the eastern (rightmost) edge of the cell. Downdraft is visible in both calculations in the high-reflectivity region of the cell. The downdraft is stronger in the CP-2/bistatic retrieval. Inset labeled B, C, M with horizontal line indicates location of plot area relative to the three radar sites.	10

1.8	Horizontal section of 3D wind field measured by a bistatic dual-Doppler radar. (Wurman, 1994)	11
1.9	The concept of 3D wind velocity measurement with a monostatic radar (left, with the Doppler Beam Swing method) and with a multistatic radar (right). Each cubic cell represents a unit volume in which a 3D wind velocity can be determined.	12
2.1	Variation of the estimation error of the Doppler shift versus signal-to-noise ratio. The number of incoherent integrations is 5. Circles and crosses show results for spectral widths of $W = 2$ and $W = 10$, respectively, which are normalized by the spectral interval. Solid and dashed lines correspond to the errors obtained by the fitting and moment methods, respectively. . . .	17
2.2	Measurement principles in a dual-Doppler radar. The line-of-sight Doppler velocities measured by the radars correspond to u_0 and u_1	19
2.3	Error ellipses of a two-dimensional dual-Doppler radar system. Two radars are placed at 0 and 1 in the x-axis.	21
2.4	Measurement principles in a bistatic atmospheric radar system. The line-of-sight Doppler velocities measured by the radar and the receiver correspond to u_0 and u_1 , respectively.	22
2.5	Error ellipses for a bistatic radar system in a two-dimensional representation. The main radar and the receiver are set at 0 and 1 in the x-axis, respectively.	24
2.6	Horizontal component of the estimation error of the wind with a bistatic radar. The main radar is placed at 0 and the bistatic receiver is assumed to be set at 1,300m in the x-axis, according to the observations made in this study.	25
2.7	Vertical component of the estimation error of the wind under the same condition as in Fig. 2.6.	25
2.8	Shapes of the target in a bistatic and a monostatic radar. Illustrated for a case: altitude= 2000m, beam width is 3.4° , bistatic receiver position $x = 1300$ m, and the zenith angles of the beam are -30,0 and 30 degrees. Solid lines and dashed lines which pass the horizontal line at the center of the volumes indicate the line-of-sight from the radar and the receiver, respectively. Shaded boxes show the thickness of 150m, which corresponds to the pulse width of $1\mu s$ that is used in this study.	26
2.9	Vertical resolution for a bistatic radar. The beam width and the receiver position are assumed to be 3.4° and $x = 1300$ m, respectively. An omnidirectional beam pattern is assumed for the receiver, to determine the edges of the volume.	27
2.10	Vertical resolution for a monostatic radar. The beam width is assumed to be 3.4° . Only 1-way gain is utilized to calculate this graph.	27

3.1	Configuration of a high-gain antenna with a peripheral receive-only sub-array.	32
3.2	Receiver and signal processing system at the MU radar.	34
3.3	Antenna field configuration and antenna positions for the observation in this study.	35
3.4	Doppler echo power spectrum at 2.4km range raw main beam data (dashed) and processed with conventional DCMP algorithm (solid). The y-axis indicates received power in arbitrary units.	36
3.5	Doppler echo power spectrum at 2.4km range raw main beam data (dashed) and processed with the proposed DCMP-CN algorithm (solid).	36
3.6	SNR loss as a function of constrained norm value U	39
3.7	Example of the Doppler echo power spectrum with strong aircraft echo at a sampling interval of 76ms from raw main beam data (dashed) and with proposed DCMP-CN algorithm (solid). The y-axis indicates received power in arbitrary units.	41
3.8	Same as Fig.3.7, but for a sampling interval of 7.6ms.	41
3.9	Gain in direction of interferer for monochromatic signals with different Doppler velocities.	44
3.10	Same as Fig.3.9, but for the interferer with spectral width of 0.33m/s.	44
3.11	Gain in direction of interferer for signals with different spectral width when no mean motion is present.	45
4.1	Definition of θ (zenith angle) and ϕ (azimuth). An array is placed within x-y plane.	49
4.2	The visible region in $b_0(\boldsymbol{\eta})$ in $\boldsymbol{\eta}$ -space. The origin means the direction of the main beam. The solid circle corresponds to the horizon along the plane in which the array is placed when the main beam is assumed to be steered toward the zenith. The smaller dashed circle is the horizon appears when the mainlobe is horizontally tilted. The inside of the larger dashed circle thus corresponds to the entire visible area when all the possible mainlobe directions are allowed.	52
4.3	Weight function $\Psi(\boldsymbol{\eta})$. R_0 and R_1 should be set to the size of visible region and mainlobe region, respectively.	53
4.4	Flow chart of the optimization algorithm with beam-space evaluation.	54
4.5	A potential function $\psi(\mathbf{x})$ in \mathbf{x} -space as a Fourier transform of $\Psi(\boldsymbol{\eta})$ corresponding to $R_0 = 1$	55
4.6	The equivalence in antenna space and beam space is illustrated. According to Parseval's theorem, the squared integration of the total potential field, which is a convolution of the potential function and a antenna function, is guranteed to be equivalent to the squared integration of a beam function multiplied with the kernel function.	56

4.7	A resulting array that the most usually appears as 12-element array with the trial-and-error algorithm. This type of array has grating-lobes because of uniform spacing. In each figure, "DMIN" indicates minimum distance of antennas, "MS" and "PK" indicate mean-square sidelobe within the radius $R \leq 1$ except for the mainlobe region $R \leq 0.1$ and the peak sidelobe level (in power ratio to the main-lobe) within $0.2 < R < 2$	58
4.8	Resulting arrays generated by the try-and-error algorithm. The performance of each array is evaluated by mean-square sidelobe response and the peak sidelobe response which are noted on top of its left panel. Top panels show a triangular array that has the minimum mean-square sidelobe response and appears most frequently as a result.	61
4.9	The scattering diagram for the peaks vs. mean-square sidelobe responses of 10,000 arrays generated by the iteration algorithm.	62
4.10	Resulting arrays generated by the same algorithm in Fig.4.8 but under the constraint of 3-fold (120 degrees) rotational symmetry.	63
4.11	The scattering diagram for the peaks vs. mean-square sidelobe responses of 10,000 arrays generated by the iteration algorithm.	63
4.12	The scattering diagram for the peaks vs. minimum distance of adjacent antennas in the array. The data is the same as for Fig.4.11. The corner at the right-bottom is the best.	64
4.13	An example of 12-element array generated under the condition of 3-fold symmetry. This type of array has remarkably low sidelobe response.	64
4.14	A scattering diagram of peak-sidelobe vs minimum distance between antennas. The array of Fig. 4.13 is located at around the right bottom corner.	65
4.15	Antenna displacement ($N = 12$) generated by proposed algorithms. Circles indicate antenna positions. Lines which link two adjacent antennas closer than 1λ are put for visibility. Left and right panel show the case $R_0 = 1.5$ without and with potential barriers, respectively.	66
5.1	Estimation error of the horizontal wind velocity in a vertical beam versus the length of the baseline.	68
5.2	Signal-to-noise ratio profile measured by the EAR in a monostatic observation using Spano code (dashed). The solid line shows an SNR which is shifted by -17.5dB ($=10 \log_{10}(560/10)$) from the dashed line assuming 10 antennas are used in a receiver site.	69
5.3	A plan view of the EAR, site-A and B.	70
5.4	Arrangement of the antenna at Site-A and Site-B.	71
5.5	Schematic diagram of a digital receiver board and the entire digital receiver system.	72
5.6	Block diagram of a 1-stage Cascaded-Integration-Comb filter. Rectangles show delay elements.	74

5.7	Phases measured at ground pulses by the antenna No.1. The right panel magnifies the first 6 s of the left panel. A periodical leap with an interval of 1 s appears overlaid with long time fluctuation.	77
5.8	Phases measured at ground pulses by several antennas. The right panel magnifies the first 6 s of antenna No.1. Sporadic phase variations are observed which seem to be caused by transitions of sets of the GPS satellites.	77
5.9	Phase of ground pulses after the compensation process. Fluctuations are removed compared to Fig. 5.7(right).	77
5.10	The beam pattern of MU radar.	79
5.11	A beam pattern of a two-dimensional array with 10 antennas.	79
5.12	Doppler spectra (altitude=2136m) observed by Site-B made with no adaptation (dashed) and with the adaptive clutter suppression technique. The conspicuous clutter component at the center of Doppler velocity has been cancelled by the algorithm.	81
5.13	Spatial responses of the array with no adaptation (dashed) and with the adaptive clutter suppression technique (solid) corresponding to the data utilized in Fig.5.12. This pattern is swept in the plane including the receiver (site-B) the target (shown as desired) and a clutter. This clutter is found by Capon's imaging algorithm. A clear null is formed by the adaptation.	82
5.14	Doppler spectra (altitude=3295m) observed by Site-B made with no adaptation (dashed) and with the adaptive clutter suppression technique. A case that the Doppler velocity of the atmospheric echo is around the zero.	83
5.15	An altitude-velocity spectrum observed at site-B at 12:00 LT 26,Sep,2004, in mode-A for the direction (225,30), after a coherent sum of 8 antennas out of 10. (For reasons of the stability of the equipment, only 8 antennas worked at this period.)	84
5.16	The same as Fig.5.15 but with the adaptive spatial filtering procedure.	85
5.17	Example of a horizontal section of the wind velocity field at three consecutive observation cycles. The origin of each arrow is the center of the target volume. The arrow with solid line shows a 2D horizontal velocity vector (u,v) , and that with a dashed line shows a vertical component w . In the top panel, the small circle at the origin shows the 3dB diameter of The transmitted beam (one way) and the two crosses show the position of the receiver sites.	86
5.18	Estimation error of u, v and w in a horizontal section at 3800 m in altitude. Estimation error of each radial velocities is assumed to be 0.104 ms^{-1}	88
5.19	Vertical profiles of the zonal (top row) and the meridional (bottom row) wind components estimated by the two observation methods. The solid line is by the monostatic method using the data of the EAR alone, and the dotted line is by the proposed multistatic method.	90

5.20 Antenna displacement of Site-A and Site-B in the observations for CPEA-II. Open and closed circles show positions of Yagi and dipole antennas, respectively. Closed squares are the reference points used for the measurement. 91

Chapter 1

General Introduction

1.1 Adaptive Array Techniques for Undesired Signal Cancellation

Adaptive array techniques have been the center of interest in applications, such as radar, sonar and communications, where a desired signal should be extracted suppressing the other undesired signals, namely various types of clutters, undesired wireless communication channels, intentional jammers and so on. Figure 1.1 illustrates the system model utilized in this chapter in which the output is defined by linear sum of observed signals as,

$$\begin{aligned} s(t) &= \sum_n w_n^* s_n(t) \\ &= \mathbf{w}^H \mathbf{s}, \end{aligned} \tag{1.1}$$

where w_n , $s_n(t)$ are the weight and received signal of n th antenna, respectively, have several different principles according to criteria.

The Minimum Mean-Square Error (MMSE) estimation criterion is the most classical technique first studied by Widrow (1967), Riegler (1973) and Compton (1978). This algorithm is also the most commonly employed algorithm for certain type of applications, in which the desired signal can be regarded as known, and is well suited especially for communications. In a real applications, this optimization is performed taking advantage of prescribed training sequences. Given the covariances between the desired signal and observed signals as $\mathbf{r} = (r_1, r_2, \dots, r_N)^T$ (superscript T denotes matrix or vector transpose), the optimum weight is derived as

$$\mathbf{w}_{\text{MMSE}} = \frac{R_{ss}^{-1} \mathbf{r}}{\mathbf{r}^T R_{ss}^{-1} \mathbf{r}},$$

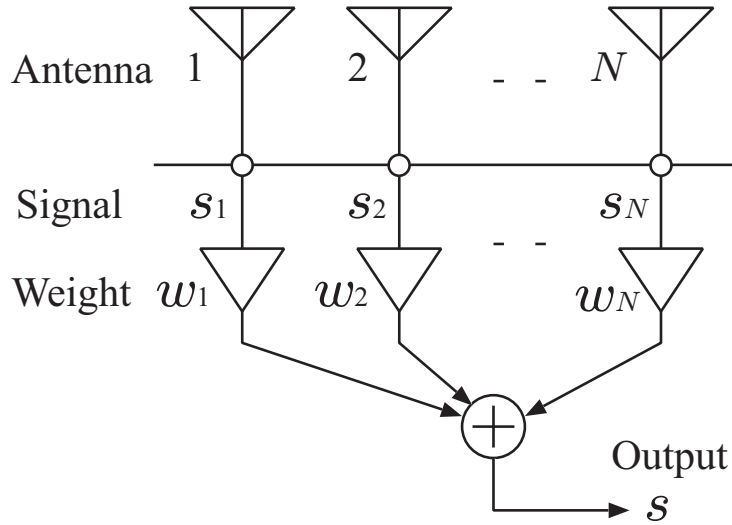


Figure 1.1: System model of an array consisting of N antennas. The output s is constructed by a linear sum of all the signals from s_1 to s_N with adaptively controlled coefficients from w_1 to w_N .

where R_{ss} is the covariance matrix defined as

$$R_{ss} = \begin{pmatrix} \Sigma s_1 s_1^H & \Sigma s_1 s_2^H & \dots & \Sigma s_1 s_N^H \\ \Sigma s_2 s_1^H & \Sigma s_2 s_2^H & \dots & \Sigma s_2 s_N^H \\ \vdots & \vdots & \dots & \vdots \\ \Sigma s_N s_1^H & \Sigma s_N s_2^H & \dots & \Sigma s_N s_N^H \end{pmatrix}. \quad (1.2)$$

In a scenario that the desired signal arrives from a known direction and undesired signals come from other directions, a principle called *Minimum Variance Distortionless Response* (MVDR) is employed to retrieve the desired signal. Utilizing vector representation, the principle is described as a linear constraint minimization problem given by

$$\text{minimize } [P = \mathbf{w}^H R_{ss} \mathbf{w}] \quad (1.3)$$

$$\text{subject to } \mathbf{w}^H \mathbf{c} = N, \quad (1.4)$$

where R_{ss} is the $N \times N$ signal covariance matrix. This algorithm is known for its excellent performance in rejecting undesired signals. Adaptively, the output weight vector \mathbf{w}_{MVDR} forms null responses toward the undesired signals while it maintains a constant response to the desired signal. An output beam pattern made with this method is shown Fig.1.2. A geometrical description of this algorithm is also presented in Fig. 1.3.

However, it is known that this algorithm results in a poor response in case the covariance matrix is not sufficiently averaged. A robust clutter rejection algorithm is proposed and demonstrated in a real observation in Chapter 3.

1.1. ADAPTIVE ARRAY TECHNIQUES FOR UNDESIRE SIGNAL CANCELLATION 3

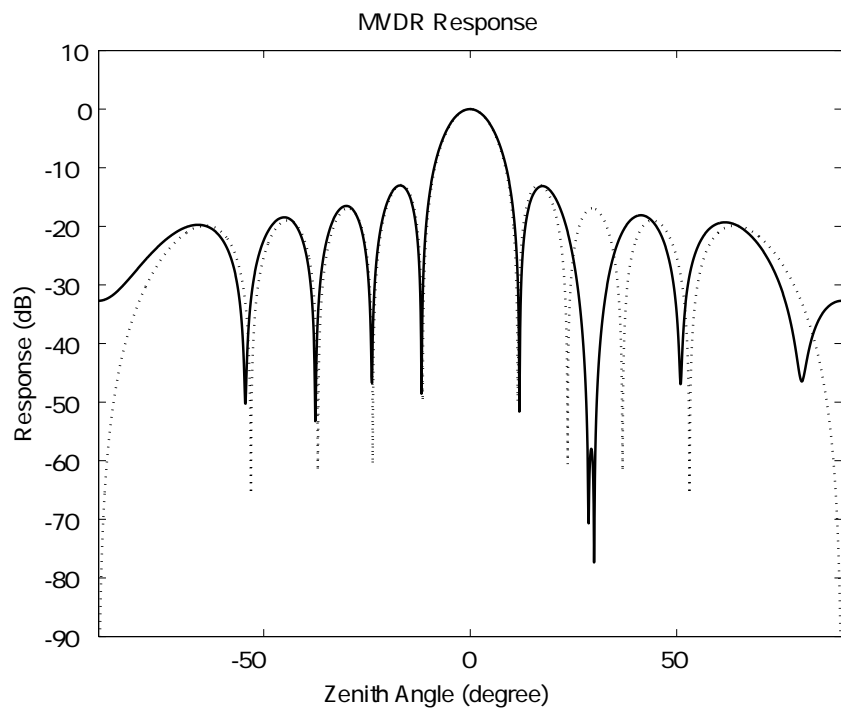


Figure 1.2: A typical response of the MVDR algorithm. An interference arrives from of the direction of 30° with a power of 30 dB compared to the noise level.

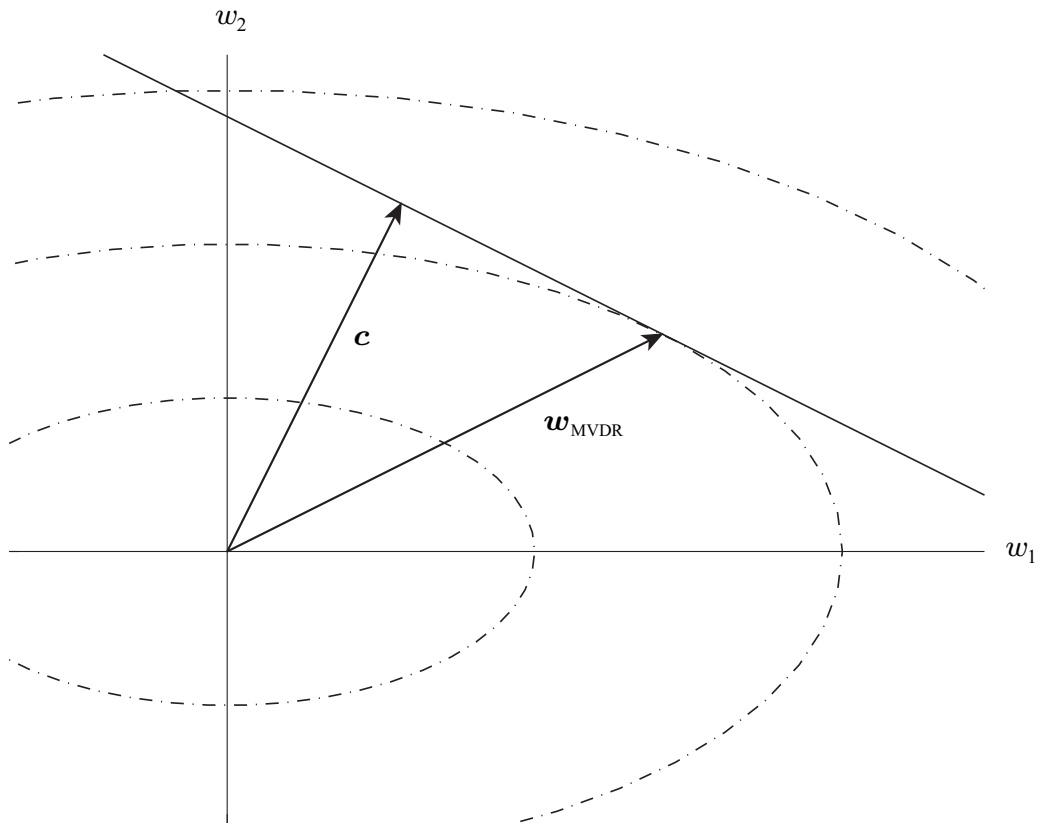


Figure 1.3: Geometrical representation of MVDR algorithm illustrated in two-dimensional space. Dashed-dot lines show the contours of the evaluation function. The solid line shows the constraint plane orthogonal to \mathbf{c} . The MVDR solution points at which the gradient of the evaluation function matches $\gamma\mathbf{c}$ where γ is a scalar.

1.2 Adaptive Array Processing for Atmospheric Radar

These years, among radar atmospheric observations, high-resolution observation and/or analysis techniques have been put into practice in parallel with growth in digital radio technology. Every high-resolutional observation techniques using radio wave is achieved owing to its phase. The most elementary technique is the *Radar Interferometry*, which has been commonly used to find a direction of arrival (DOA) of a point-source wave in radio astronomy and radar. Being extended to a multiple channel scenario, this technique has various representation according to usage of the signals. *Capon's method*, *the Multiple Signal Classification* (MUSIC) are the ones widely known for this purpose. These algorithms are referred to as "adaptive algorithm" because, from the point of view as a filter, their response adaptively changes corresponding to input data.

MUSIC (Schmidt, 1986) is most often used for signal source location problems. Schmidt presented its outstanding spectral resolution using audio spectrum estimation in frequency domain. Since this method is categorized in a class of null steering method, however, source power distribution can not be well estimated. In addition, for retrieving the signal found in this method, it is needed to employ some other signal estimation methods. A similar approach using eigen vector system was shown by Bienvenu et al. (1983).

Capon's method (Capon, 1969) is probably the most well-known spectral estimation method and is widely utilized in image reconstruction problems in radar. This method is quite a stable due to its optimality criterion, which is given by a least mean square. However, in a spectral estimation context, this method does not match the power distribution of the signals fed in the system. Lagunas and Gasull (1984) modified the Capon estimator to obtain *true* power distribution of the given signal spectrum. Although the limitation of this method for signal separation is basically the same as Capon's method, the estimated spectrum has a better appearance. Smaïni (2002) showed the difference of these estimator (Fig.1.4) in a frequency domain high-resolution imaging for atmospheric radar discussed later in this chapter.

In an atmospheric radar application, Palmer et al.(1998) made several works on high-resolution reflectivity imaging of the atmosphere using adaptive algorithms. Figure 1.5 shows reflectivity images constructed by Fourier (non-adaptive) method and Capon's method. He also showed Doppler velocity distributions within a beam circle which can not be demonstrated with a low-resolution Fourier method.

The same principle is employed for a high range resolution observation using multiple frequency radar and this technique is called *frequency domain interferometry* (FDI). Luce (2001) demonstrated an FDI imaging technique using Capon's method over the MU radar's data. In his paper, it is introduced that Lagunas-Gasull method exhibits a better range resolution comparing to Capon's method. Figure 1.6 shows a recent result made with this FDI method using five adjacent frequencies spanning a bandwidth of 2 MHz (Hassenpflug, a private document, 2006).

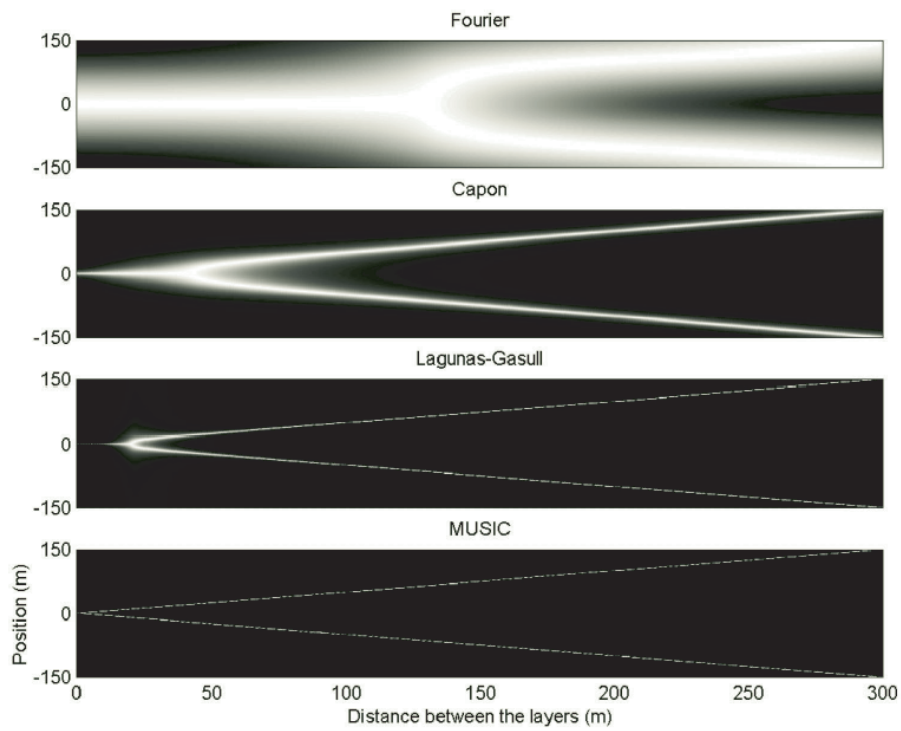


Figure 1.4: Comparison of the resolving power of the different methods used in range profile estimation as a function of SNR from 0 to 30 dB. The normalized brightness is represented for two infinitely thin layers separated by 75 m.

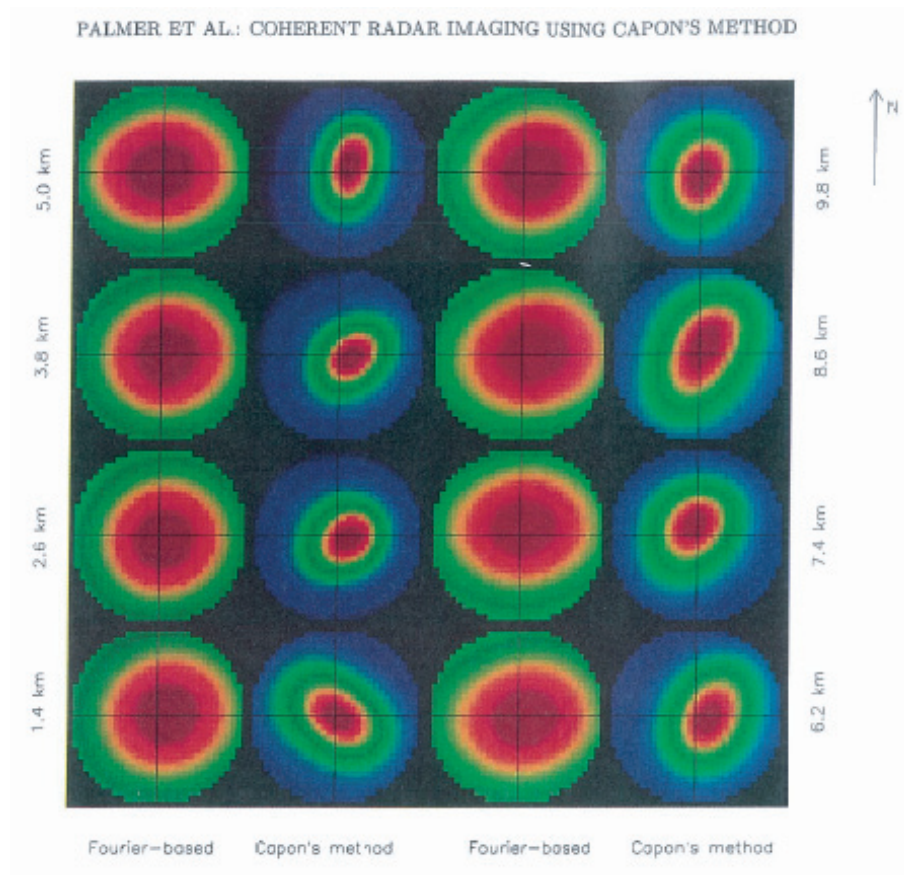


Figure 1.5: Brightness distribution average over the velocity range $\pm 1 \text{ ms}^{-1}$ within $\pm 4^\circ$ above the middle and upper atmosphere (MU) radar wite at eight arbitrary altitudes. Red colors correspond to highest brightness. As shown, images on the left and right of each pair were obtained using Fourier-based and Capon imaging techniques, respectively. Notice that Capon's method seems to exhibit better resolution than the Fourier-based method. (Palmer, 1998)

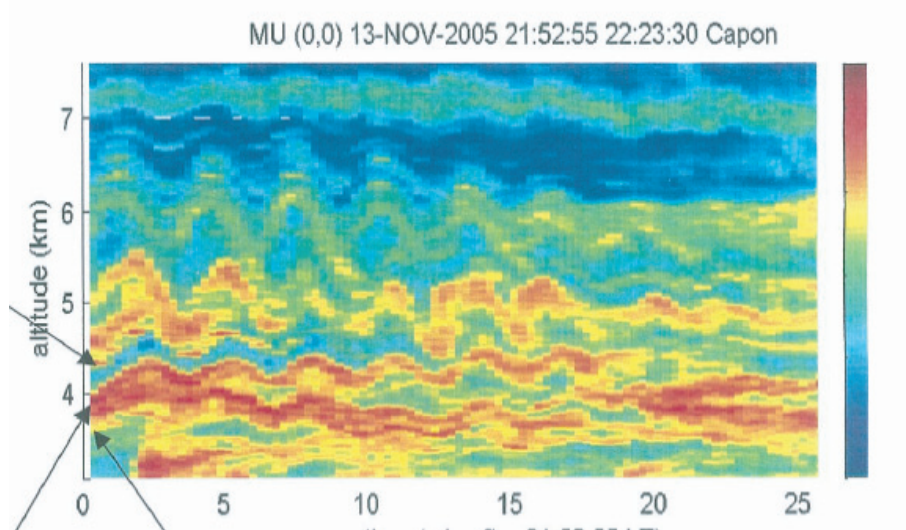


Figure 1.6: A brightness distribution along the range direction using a five frequency FDI imaging with Capon's method. The beam direction is $(0,0)$. The x-axis is time in minute.

1.3 Early Study on Bistatic/Multistatic Observation for 3D Wind Field

Of all the atmospheric radars utilized, including the widely distributed mesosphere-stratosphere-troposphere (MST) radar network such as Jicamarca radar (Woodman and Guillen, 1974), MU radar (Fukao et al., 1985) as well as the Equatorial Atmosphere Radar (EAR) (Fukao et al., 2003), monostatic radar systems are the type that have consistently been employed. A monostatic system is superior from the points of view of sensitivity, maintainability and economics, because it has a single large aperture antenna or array.

In order to estimate the velocity of the atmosphere, Doppler shift of atmospheric echo is utilized. However, this is just one projection component the 3D wind velocity and we must measure at least three linearly independent components. For monostatic atmospheric radars, which have high gain and high speed electronic steering capability, array Doppler Beam Swing (DBS) is the method most commonly utilized for the wind velocity estimation. This method is performed by scanning several different direction around the zenith – it also means spatially different parts – and estimating each line-of-sight (LOS) velocity. From the point of view of spatial resolution, it is fairly restricted because a monostatic radar system requires an assumption of homogeneity of an observed wind field, and thus it mainly provides a vertical profile of the wind velocity and turbulence intensity. This is because monostatic radar can only observe the radial components of the wind field, and that a 3D wind velocity needs to be estimated from several radial velocities of horizontally separate target volumes.

1.4. HIGH-RESOLUTION DOPPLER OBSERVATION AT THE EQUATORIAL REGION⁹

Bistatic radar is one that is equipped with a receiver, together with a main radar (transmitter/receiver), simultaneously to receive obliquely scattered echoes from a target. A conceptual illustration of monostatic radar and bistatic (a *multistatic* is hereafter used for one that has two or more receivers) radar is shown in Fig.1.9. The first bistatic radar observation of the atmosphere was started from 1970 at the Valley Forge-Wallops Island radar (Doviak, 1972). At this time, radar atmospheric observation of the lower stratosphere was a pioneering work, and the main purpose of this system was to obtain a more gain to detect a clear-air atmospheric echo from high-altitude target using non-coherent radars.

Bistatic/multistatic radar is the most powerful when it is equipped with a coherent radar capability. Measuring multiple Doppler velocity components from one target volume, the radar can determine a 3D wind vector without assuming spatial uniformity. First studies on bistatic/multiple-Doppler radar observation for high-resolution vector wind field observation are made by Wurman (1993, 1994). His system consisted of two high-power rapid scanning S-band Doppler radar and one passive omni-directional receiver with no scanning capability. The study successfully exhibited three-dimensional wind vector field and an existence of strong up/downdraft wind with a resolution of as precise as 250m^3 grid (Figures 1.7 and 1.8).

1.4 High-Resolution Doppler Observation at the Equatorial Region

The tropical Pacific region especially the Indonesian Archipelago in which the Equatorial Atmosphere Radar (EAR) is located, is considered a major source of global atmospheric circulation. The convection generated in this region is considered to be essential for this energy flow through the process that is currently being examined by a program called "Coupling Processes in the Equatorial Atmosphere (CPEA)". Compared to a layered current, however, a convective current, which is accompanied by turbulence, shows remarkably complex motion with changes in its momentum vectors. The restrictive resolution of a monostatic radar system imposes potential limitations in the spatial scale of these motions. The horizontal scale of the vertical current appears in a developing state of cumulonimbus is less than 2 km and this process is not sufficiently observed in the history of observations of the tropical atmosphere.

Figure 1.9 (left) shows the concept of monostatic radar. Monostatic radars with DBS method can thus observe a single 3D wind velocity within a volume scanned to obtain velocities utilized for the estimation. The directions utilized for 3D velocity estimation is usually set to a symmetric arrangement to the zenith angle. The horizontal scale of spatial resolution achieved by this method is, for example, approximately $1000\text{ m} \times 1000\text{ m}$ and $2000\text{ m} \times 2000\text{ m}$ at 3000 m and 6000 m in altitude, respectively, when the zenith angle for symmetric beams is set to 10° as a typical value. This means the DBS method can

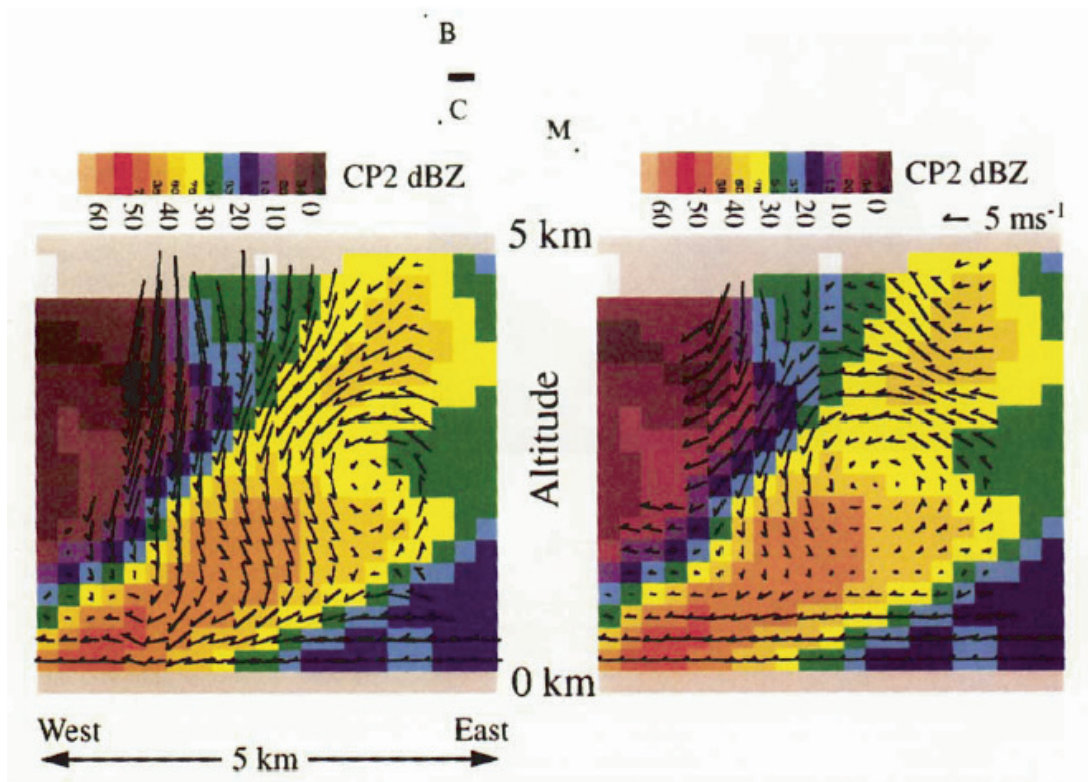


Figure 1.7: East-west vertical slice through weak convective cell. Vectors show slice parallel wind vectors calculated using CP-2 and bistatic data only (left) and CP-2 and MHR data only (right). Shading in both panels is CP-2-measured reflectivity. Updraft is visible in both calculations at the eastern (rightmost) edge of the cell. Downdraft is visible in both calculations in the high-reflectivity region of the cell. The downdraft is stronger in the CP-2/bistatic retrieval. Inset labeled B, C, M with horizontal line indicates location of plot area relative to the three radar sites.

1.4. HIGH-RESOLUTION DOPPLER OBSERVATION AT THE EQUATORIAL REGION 11

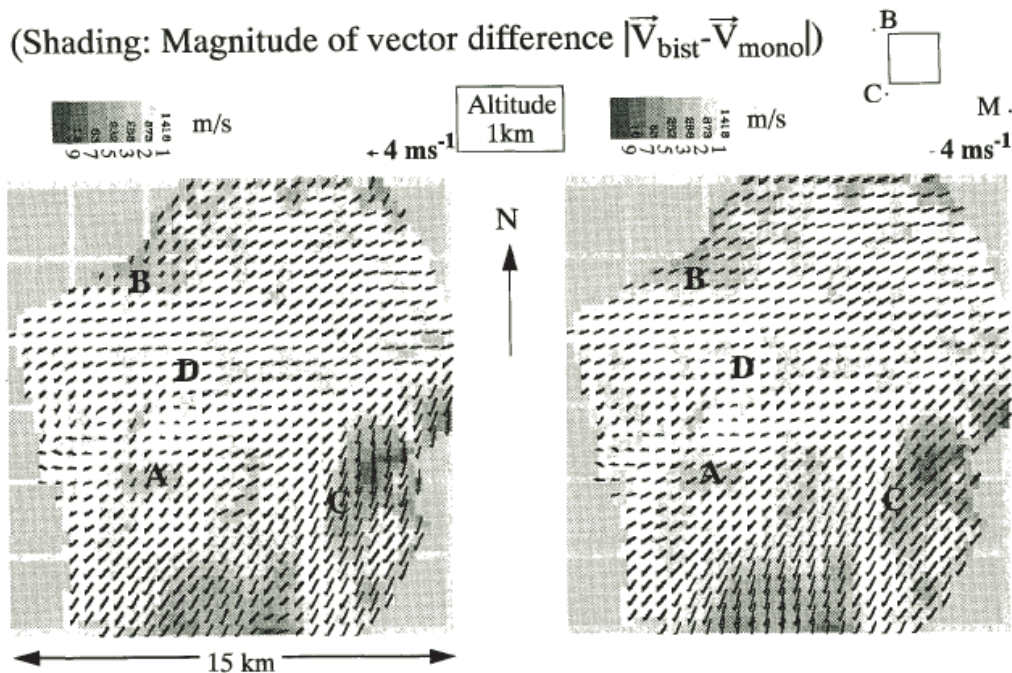


Fig. 7. Horizontal slice at 1 km above ground level through hail-producing storm complex. Same plot area as in Fig. 6. Shading in both panels is magnitude of vector difference between CP-2/bistatic and CP-2/MHR horizontal dual-Doppler wind vectors. Vectors are CP-2/bistatic (left) and CP-2/MHR (right) horizontal dual-Doppler wind vectors. Throughout much of the cell, the difference between the bistatic and monostatic horizontal wind vectors is less than 2 m s^{-1} . Higher discrepancies are visible in regions A, B, and C, corresponding to the regions of reflectivity differences noted in Fig. 6. Inset labeled B, C, M with square indicates location of plot area relative to the three radar sites.

Figure 1.8: Horizontal section of 3D wind field measured by a bistatic dual-Doppler radar. (Wurman, 1994)

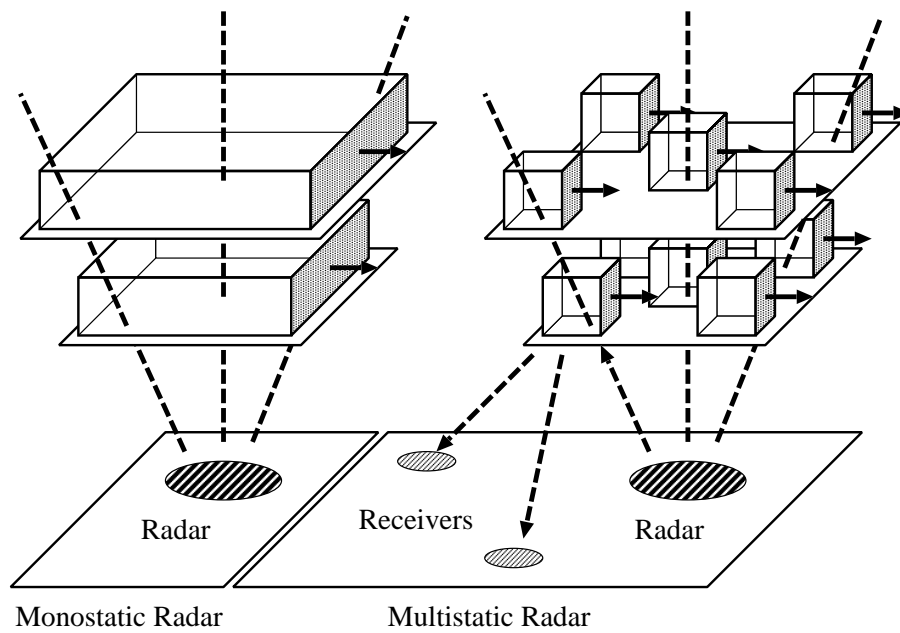


Figure 1.9: The concept of 3D wind velocity measurement with a monostatic radar (left, with the Doppler Beam Swing method) and with a multistatic radar (right). Each cubic cell represents a unit volume in which a 3D wind velocity can be determined.

only observe the wind perturbation that has a larger scale than these values.

Multistatic radar is a progressive modification of monostatic radar that is ideally suited for high-gain MST radars. This system is equipped with multiple receiver arrays to simultaneously observe obliquely scattered echoes from a single target volume, together with the main radar. Hence it is possible to determine 3D velocity vectors in every single target volume as discussed in section 2.4. Figure 1.9 (right) shows an outline of multistatic radar. Employing this method, the horizontal resolution is much improved than the monostatic radar and it reaches the scale of beam width of the radar, namely, with the EAR, approximately $200 \text{ m} \times 200 \text{ m}$ and $400 \text{ m} \times 400 \text{ m}$ at 3000 m and 6000 m in altitude, respectively.

In contrast to these advantages, there are several technical issues to be dealt with such as synchronization and maintainability to realize a practical multistatic radar. Historically, multistatic atmospheric radar, including bistatic radar, has mainly been employed for the study of the ionosphere with large incoherent scatter radars such as at the St. Santin (Amayenc et al., 1973) and EISCAT (Alcayde et al., 1982) facilities. In the neutral atmosphere region, Doviak et al. (1972) and Woodman (1980) succeeded in obtaining preliminary results of tropospheric and stratospheric observations using a S-band non-Doppler bistatic receiver aimed to enhance its layered scattering structure. Wurman et al. (1993) developed a bistatic and dual-monostatic S-band Doppler weather radar and showed comparable wind fields measured by both schemes. In these observations, however, strong clutters caused by the low-gain broad beam of the receiver appeared. For our MST observations in which the signal-to-noise ratio is severe, this clutter is a vital issue that needs to be addressed.

The current study is thus the first attempt to measure the wind velocity of the MST region with multistatic atmosphere radar. In this study, the transmitter antenna beam direction is steered in the zenith angle region of 30° . In traditional multistatic radars, the transmitter beam direction has been fixed, because it is difficult to simultaneously match the receiving beam direction to the target volume illuminated by the transmitter beam at multiple heights when the transmitter beam direction is altered. This problem is resolved by the use of post beam steering with digital receiver arrays, as described in section 2.4.

In the following sections, we first briefly examine the principles of wind velocity measurement with a multistatic radar system, focusing on a quantitative assessment of its accuracy. We next describe the system configuration, observational setups and data processing schemes, which include adaptive clutter rejection. We finally present some examples of wind velocity fields obtained by the first series of experiments that took place in September 2004.

1.5 Contents of This Thesis

In this chapter, background of adaptive array processing techniques and early study of multistatic observation of the atmosphere are discussed. The scope of this thesis is to present technical consideration for realizing multistatic radar constructed on top of existing large atmospheric radar/wind-profiler. We briefly review the contents of each chapter.

In Chapter 2, some aspect of multistatic atmospheric radar which must be considered for practical observations. Correlated error effect in estimated wind vector is particularly discussed. For a better clarification, the properties are discussed in a bistatic representation being compared with a dual-Doppler radar system that has two independent radars.

In Chapter 3, a norm-constraint stabilization method for adaptive clutter rejection is discussed. On a partial-adaptive basis, this method is applied to a practical observation with the MU radar. Using real data, it is shown that the norm constrained algorithm reduces noise in synthesized signals.

In Chapter 4, a novel method is discussed for two-dimensional array optimization, especially for adaptive array processing into consideration. Some results that have practically preferable properties in this respect are presented. Also, a fast algorithm for this algorithm which becomes important for a practical large array design is discussed.

In Chapter 5, the first multistatic observations made in 2004 with the EAR are presented, including system design, real-time and post-observation processes and analysis based on the discussion made through Chapters 2–4. The recent observation made in 2005 with modified equipment, software and observation schemes are also presented.

Chapter 2

Multistatic Radar Technique

2.1 Introduction

Multistatic radar observation is one of the most effective method to measure the three-dimensional wind velocity fields. In spite of its simplicity, however, the error distribution and the shape of target volumes are deformed due to its asymmetric structure. In this chapter, we study these properties based on its principle of observation rather than technical consideration. To clarify the characteristics, a bistatic radar system are examined comparing to a dual-Doppler radar systems (consisting of two radars) which has a symmetric structure.

2.2 Doppler Velocity Estimation

Atmospheric radar is a method that measures 3D motion of the atmosphere utilizing its faint scatter of radio waves. This scattering is caused by spatial difference of the refractive index in the atmosphere. In fact, various mechanisms produce the spatial difference of the refractive index; the difference of the density or the humidity in the atmosphere, raindrops, mist, and so on. We target the ones by the spatial difference of the density and the humidity, which can be the most effectively observed by VHF radar, to measure the motion of the atmosphere.

In order to observe the 3D dynamics of the atmosphere, which boundlessly spreads, it is necessary spatially to sample the atmosphere within the space of interest. We utilize time gating of radio waves to slice the space along the range direction, and a narrow beam for cross-range separation. By observing Doppler velocities of the wind within volumes divided into pieces, the entire 3D wind field can be obtained.

Doppler velocity v_d is the radial component of target velocity, which is the only component that is measured with radar. v_d is calculated by Doppler shift f_d of a returned

signal based on the relation

$$v_d = \frac{cf_d}{2f_0} \quad (2.1)$$

where f_0 is the carrier frequency and c is the velocity of light. In order to estimate a 3D wind vector, it is necessary to measure three linearly independent components of the wind. We have some variations of method to obtain the three components by using radar.

First, we discuss the way for monostatic atmospheric radar, which has the only one antenna array for both of transmission and reception. The Doppler Beam Swing (DBS) is the simplest method that is most commonly employed for this type of radar. This method can determine the three components of the wind velocity by observing at least three different radial components toward spatially separate target volumes. To estimate a 3D wind vector with this method, it is necessary to make an assumption of homogeneity of the wind field within the space of interest that includes the observed target volumes. Figure 1.9 (left) outlines the concept of the method with a monostatic radar. The DBS has been realized by introducing rapid scanning radar with a large antenna array that has an electronically-controlled beam steering capability.

While it has a simple principle, monostatic radar with the DBS method has a drawback in its spatial resolution that is caused by the homogeneity assumption. In general, horizontal homogeneity is assumed for this observation based on the continuity of the horizontal motion of the atmosphere. However, any smaller scale dynamics than the smeared volume and rotational components of the field can not be observed. This problem is severe for a tropospheric observation of the tropical atmosphere in which strong convective motions are expected.

Directly to observe the 3D components within a minimum resolution volume, we can conceptually propose a method with multiple Doppler radars that are separately placed to measure different projection of the wind vector. This method is called the multi-Doppler radar. While this method is almost ideal for three-dimensional measurement, it is quite costly to maintain multiple radar. For some weather radar network applications in which the cost requirement is not very severe this method has been practically employed.

Multistatic radar, which has a multiple receiver facilities in addition to a radar, is a method that can also observe multiple radial components simultaneously from several different places to determine a 3D wind vector at each minimum resolution volume. Since receivers cost by far smaller than a radar, this method is much more feasible compared to multi-Doppler radar.

The signal of atmospheric echo is a stochastic process whose power spectrum is well approximated by a Gaussian distribution function with a standard deviation of σ_f and a fluctuation proportional to its power spectral density. In a real analysis, incoherent integrations or a smoothing of the spectra must be done to obtain an accurate estimate of the Doppler shift.

Yamamoto et al. (1988) showed the estimation accuracy of the Doppler velocity does

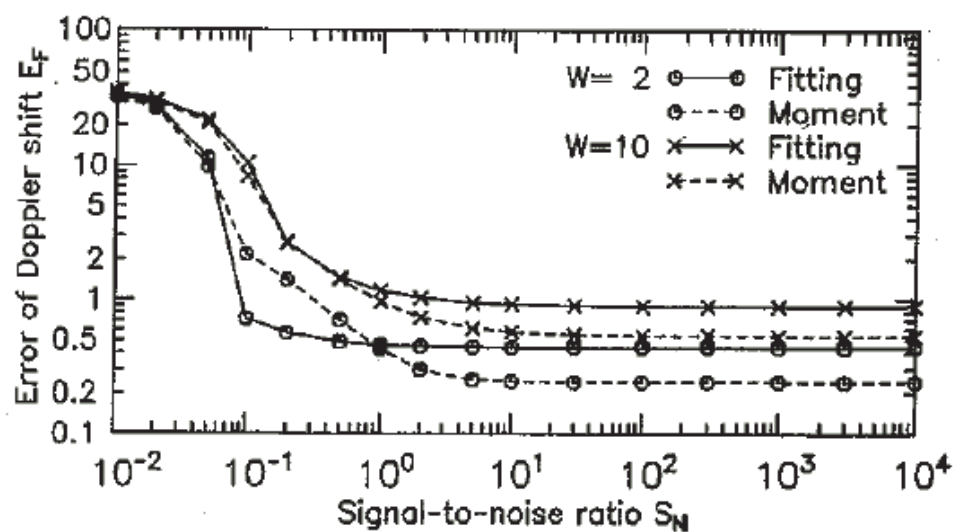


Figure 2.1: Variation of the estimation error of the Doppler shift versus signal-to-noise ratio. The number of incoherent integrations is 5. Circles and crosses show results for spectral widths of $W = 2$ and $W = 10$, respectively, which are normalized by the spectral interval. Solid and dashed lines correspond to the errors obtained by the fitting and moment methods, respectively.

not mainly depend on the signal-to-noise ratio when the SNR is sufficient. Figure 2.1 shows the dependence of the accuracy on the SNR. In this region of SNR, estimation error of the radial velocity, from the Doppler spectrum measured with each receiver array, is described by spectral resolution δ_f , spectral width of the signal σ_r and the number of incoherent integration N as follows:

$$E = k \sqrt{\frac{\lambda \sigma_r \delta_f}{2N}} \quad (2.2)$$

where λ is the wave length of the radio that is 6.38 m and k is a constant characteristic of an estimation method. According to Yamamoto, the constant k is 0.38 and 0.63 for the moment and the fitting methods, respectively.

To determine the radial velocity, we employed a fitting method of a parabolic function in a logarithmic spectrum. In some part, however, manual corrections have done to obvious misfits to compensate algorithmical instabilities. Therefore, it is rather unclear which k is best to chose. Erring on the side of safety, we chose the larger constant of 0.63 to represent k for our entire fitting process. In our data processing process, we divide a single period of 81.6 sec into 8 of 10.2 sec periods which corresponds to δ_f of 0.098 Hz and N of 8. Substituting $\lambda = 6.38$ m, $N = 8$, $\delta_f = 0.098$ Hz, and $\sigma_r = 0.7$ m/s which is typical for tropospheric observations, into eq.(2.2), $E = 0.104$ ms⁻¹.

The accuracy of wind vector estimation depends not only on the accuracy of each observed component, but also on the positions of the targets, the radar and the receiver. In following sections, we discuss the estimation accuracy comparing the system structures.

2.3 Multi-Doppler Observation Technique

Multi-Doppler radar is an ideal method for direct measurement of the 3D wind field. As mentioned in section 2.2, this method is quite costly and thus never employed for a wind profiler application. In this section, we briefly view some characteristics of this method for the sake of clarification of multistatic radar that is introduced in the following section. The measurement principle is quite simple. First, we discuss a two-dimensional observation model of multi-Doppler radar. Let \mathbf{e}_0 and \mathbf{e}_1 be normalized direction vectors from radars to a target.

The Doppler velocities that are measured with two radars are given by,

$$u_0 = \mathbf{e}_0^t \mathbf{v}_{\text{target}} \quad (2.3)$$

$$u_1 = \mathbf{e}_1^t \mathbf{v}_{\text{target}} \quad (2.4)$$

where $\mathbf{v}_{\text{target}}$ is the target wind velocity vector.

Employing the notation in Fig. 2.2, we set \mathbf{e}_0^t and \mathbf{e}_1^t to $(\cos \phi_0, \sin \phi_0)$ and $(\cos \phi_1, \sin \phi_1)$ respectively. Then, the observation equation can be written as,

$$\begin{pmatrix} u_0 \\ u_1 \end{pmatrix} = \begin{pmatrix} \cos \phi_0 & \sin \phi_0 \\ \cos \phi_1 & \sin \phi_1 \end{pmatrix} \mathbf{v}_{\text{target}} . \quad (2.5)$$

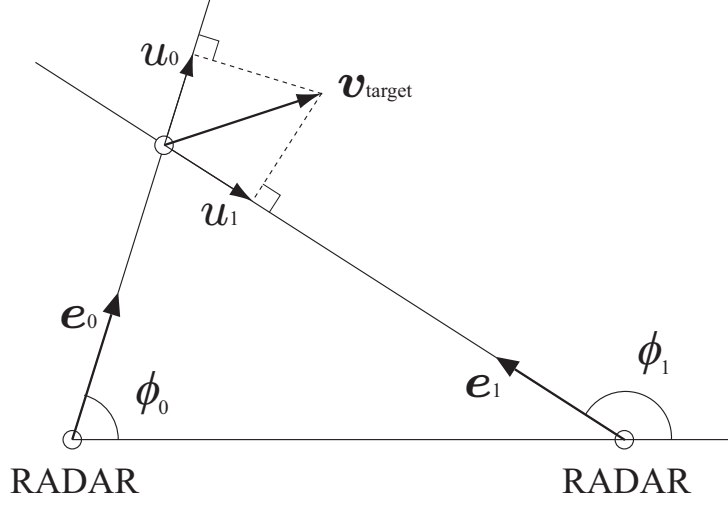


Figure 2.2: Measurement principles in a dual-Doppler radar. The line-of-sight Doppler velocities measured by the radars correspond to u_0 and u_1 .

For a non-singular observation matrix, the target velocity vector $\mathbf{v}_{\text{target}}$ can be obtained as a solution of the observation equation as,

$$\mathbf{v}_{\text{target}} = \frac{1}{\sin(\phi_1 - \phi_0)} \begin{pmatrix} \sin \phi_1 & -\sin \phi_0 \\ -\cos \phi_1 & \cos \phi_0 \end{pmatrix} \begin{pmatrix} u_0 \\ u_1 \end{pmatrix}. \quad (2.6)$$

Second, we discuss accuracy of the velocity estimation. Assuming estimation errors to be additive in each observed component, estimation equation should be given as

$$\mathbf{v}_{\text{target}} + \mathbf{v}' = \frac{1}{\sin(\phi_1 - \phi_0)} \begin{pmatrix} \sin \phi_1 & -\sin \phi_0 \\ -\cos \phi_1 & \cos \phi_0 \end{pmatrix} \begin{pmatrix} u_0 + \varepsilon_0 \\ u_1 + \varepsilon_1 \end{pmatrix} \quad (2.7)$$

where \mathbf{v}' is an error of the estimated velocity, and ε_0 and ε_1 are errors for each component. These errors can be therefore related as

$$\mathbf{v}' = \begin{pmatrix} v'_x \\ v'_y \end{pmatrix} = \frac{1}{\sin(\phi_1 - \phi_0)} \begin{pmatrix} \sin \phi_1 & -\sin \phi_0 \\ -\cos \phi_1 & \cos \phi_0 \end{pmatrix} \begin{pmatrix} \varepsilon_0 \\ \varepsilon_1 \end{pmatrix}, \quad (2.8)$$

and equally

$$\begin{pmatrix} \varepsilon_0 \\ \varepsilon_1 \end{pmatrix} = \begin{pmatrix} \cos \phi_0 & \sin \phi_0 \\ \cos \phi_1 & \sin \phi_1 \end{pmatrix} \begin{pmatrix} v'_x \\ v'_y \end{pmatrix}. \quad (2.9)$$

Here we assume ε_0 and ε_1 as iid with the mean and the covariance of

$$E \left[\begin{pmatrix} \varepsilon_0 \\ \varepsilon_1 \end{pmatrix} \right] = \mathbf{0}, \quad E \left[\begin{pmatrix} \varepsilon_0^2 & \varepsilon_0 \varepsilon_1 \\ \varepsilon_1 \varepsilon_0 & \varepsilon_1^2 \end{pmatrix} \right] = \sigma_r^2 I. \quad (2.10)$$

Then the error ellipses can be derived as

$$\begin{pmatrix} v'_x & v'_y \end{pmatrix} \begin{pmatrix} \cos^2 \phi_0 + \cos^2 \phi_1 & \frac{\sin 2\phi_0 + \sin 2\phi_1}{2} \\ \frac{\sin 2\phi_0 + \sin 2\phi_1}{2} & \sin^2 \phi_0 + \sin^2 \phi_1 \end{pmatrix} \begin{pmatrix} v'_x \\ v'_y \end{pmatrix} = \sigma_r^2. \quad (2.11)$$

Detailed derivation of this equation is described in Appendix. Figure 2.3 shows the error ellipses calculated by eq.(2.11).

2.4 Multistatic Observation Technique

2.4.1 Principle

Multistatic radar is referred to as a system that has a couple of receiver set together with a transmission/receiving radar. Being different from conventional monostatic radar, a multistatic radar can thus observe an echo from a target simultaneously at separate places and therefore, it can determine a 3D wind vector at each minimum resolution volume of the target. Hereafter, a *multistatic* is referred to as being one accompanied with one receiver array, and a *bistatic* as one with at least two receiver arrays. First, we make qualitative examination on bistatic radar. Note that the accuracies of velocity estimation at both of a radar and a bistatic receiver are assumed to be the same owing to the discussion in the introduction.

Let \mathbf{e}_0 be a normalized direction vector toward the target from the radar, and \mathbf{e}_1 be that from the receiver. The Doppler velocity, measured from the backscattering of the target (denoted v_0) is described as,

$$v_0 = \mathbf{e}_0^t \mathbf{v}_{\text{target}}, \quad (2.12)$$

where $\mathbf{v}_{\text{target}}$ is the true wind velocity vector. On the other hand, the Doppler velocity v_1 measured by the bistatic subsystem has a different nature that is described as,

$$v_1 = \frac{1}{2}(\mathbf{e}_0 + \mathbf{e}_1)^t \mathbf{v}_{\text{target}}. \quad (2.13)$$

This equation states the bistatic velocity corresponds to the time-variation of the length of the two line segments between the transmitter and the target, and the target and the receiver. One should notice that the eq.(2.13) consistently matches eq.(2.12) in case the transmitter and the receiver be placed at the same position.

When we set the components of \mathbf{e}_0^t and \mathbf{e}_1^t as $(\cos \phi_0, \sin \phi_0)$ and $(\cos \phi_1, \sin \phi_1)$ respectively, the observation equation can be written as,

$$\begin{pmatrix} u_0 \\ u_1 \end{pmatrix} = M \mathbf{v}_{\text{target}} \quad (2.14)$$

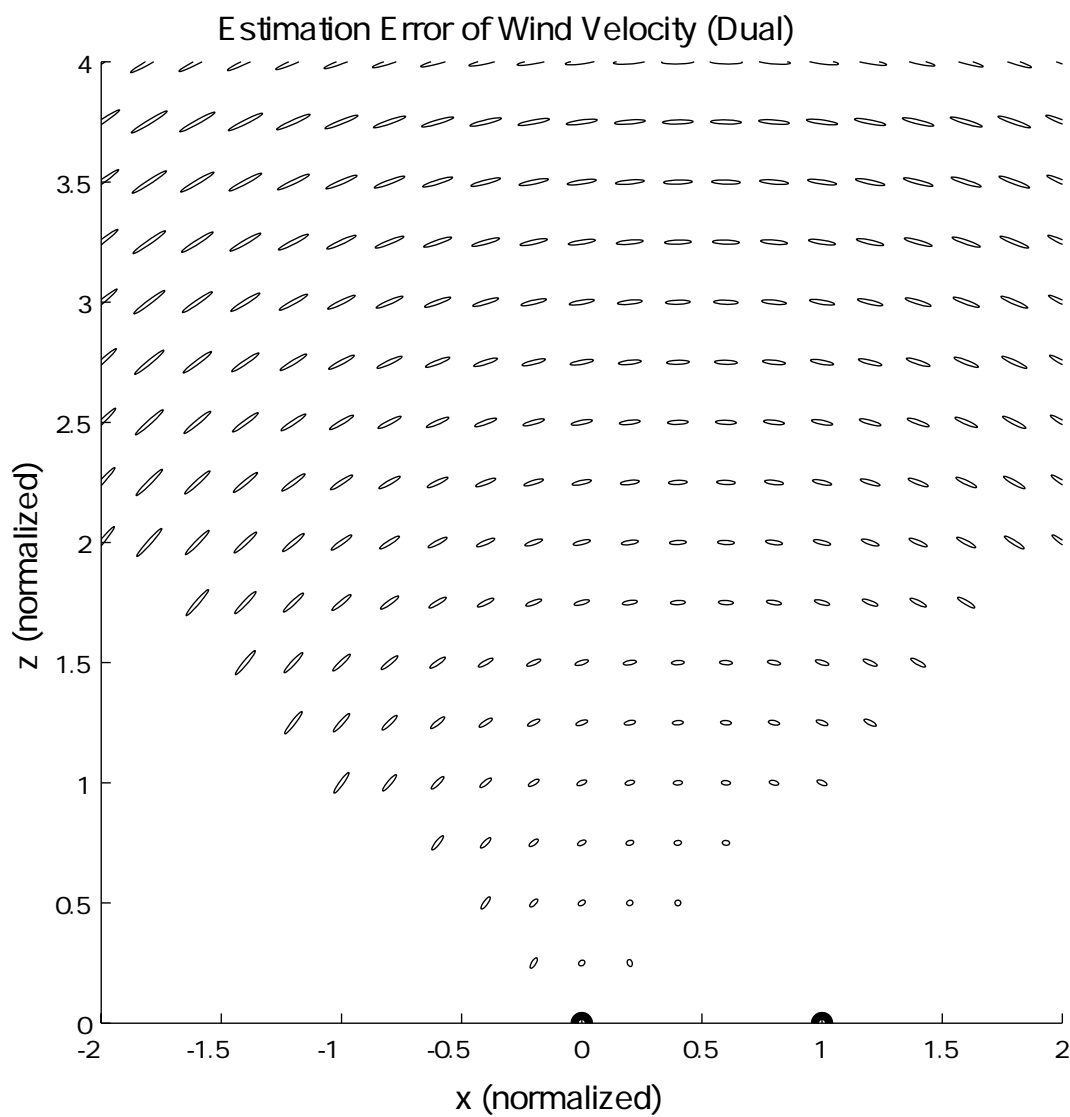


Figure 2.3: Error ellipses of a two-dimensional dual-Doppler radar system. Two radars are placed at 0 and 1 in the x-axis.

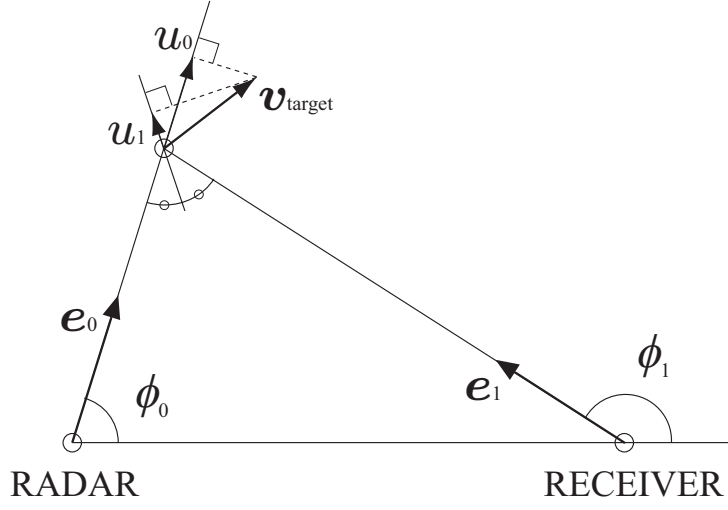


Figure 2.4: Measurement principles in a bistatic atmospheric radar system. The line-of-sight Doppler velocities measured by the radar and the receiver correspond to u_0 and u_1 , respectively.

where M is an observation matrix

$$M = \begin{pmatrix} \cos \phi_0 & \sin \phi_0 \\ \frac{\cos \phi_0 + \cos \phi_1}{2} & \frac{\sin \phi_0 + \sin \phi_1}{2} \end{pmatrix}. \quad (2.15)$$

Therefore, the estimation equation is

$$\mathbf{v}_{\text{target}} = \frac{1}{\det M} \begin{pmatrix} \frac{\sin \phi_0 + \sin \phi_1}{2} & -\sin \phi_0 \\ -\frac{\cos \phi_0 + \cos \phi_1}{2} & \cos \phi_0 \end{pmatrix} \begin{pmatrix} u_0 \\ u_1 \end{pmatrix}. \quad (2.16)$$

where $\det M$ is

$$\det M = \frac{\cos \phi_0 \sin \phi_1 - \sin \phi_0 \cos \phi_1}{2} \quad (2.17)$$

$$= \frac{\sin(\phi_1 - \phi_0)}{2} \quad (2.18)$$

As in the previous section, Figure 2.5 shows error ellipses of the wind velocity estimations by a bistatic radar. Compared to Fig. 2.3, this result shows horizontal components much worse than that of a dual-Doppler system due to the sharper angle between the projection axes for u_0 and u_1 . This effect also appears the vertical errors that rapidly become worse in the region off-zenith.

To evaluate receiver positions for real observation with the EAR, Figure 2.6 and 2.7 show a horizontal and a vertical error of the velocity estimation in which the radar is placed at (0,0), the receiver position is (0,1300) m, and the estimation error of the radial velocity $\sigma_r = 0.104 \text{ ms}^{-1}$ is assumed.

2.4.2 Shape of targets

In general, continuity of the vertical motion of the atmosphere is considered to be much lower than the horizontal motion. In this regard, the vertical spatial resolution of an atmospheric radar is required to be high.

A transmitted wave is approximately a spherical wave in which the range is sufficiently longer than the diameter of the array. For monostatic radar, a scattering volume which affects a snap-shot in the receiver forms a part of spherical shell. This corresponds to the fact that the set of points where the return travel from the radar during τ forms a sphere that has a radius $r = c\tau/2$.

While the thickness of the volume, which is determined by the transmitted pulse length, does not change depending on the range, the vertical resolution becomes worse as the range gets longer when the beam is off-vertical.

For bistatic radar, a scattering volume forms a part of the shell of an ellipsoid of revolution that has two foci at the transmitter and the receiver. It is because this shape corresponds to the set of points via which light travels between the two facilities during certain time. The scattering volume has rather an inclined shape and the vertical resolution tends to become worse, especially in case the beam is tilted backward from the receiver side. Figure 2.8 shows shapes of the scattering volume. In terms of the shapes, we can evaluate the vertical resolution by $\Delta h = (\text{top} - \text{bottom})$ within each scattering volume; Figure 2.9 and 2.10 show the vertical resolutions of a bistatic radar and a monostatic radar, respectively, versus altitude. As a monostatic system is symmetric, obviously the vertical resolution of 30° and -30° take the same values. On the other hand, a bistatic system is asymmetric and these result do not match each other. While resolutions at zenith angle of 0° and -30° are better than those of the monostatic system, resolution at 30° is much worse.

For monostatic radar, it is clarified that a systematic error which is because of the inclination of the target volumes (Fukao, 1988) exists. The same phenomena appears in bistatic systems, however, the effect must be asymmetric to the vertical.

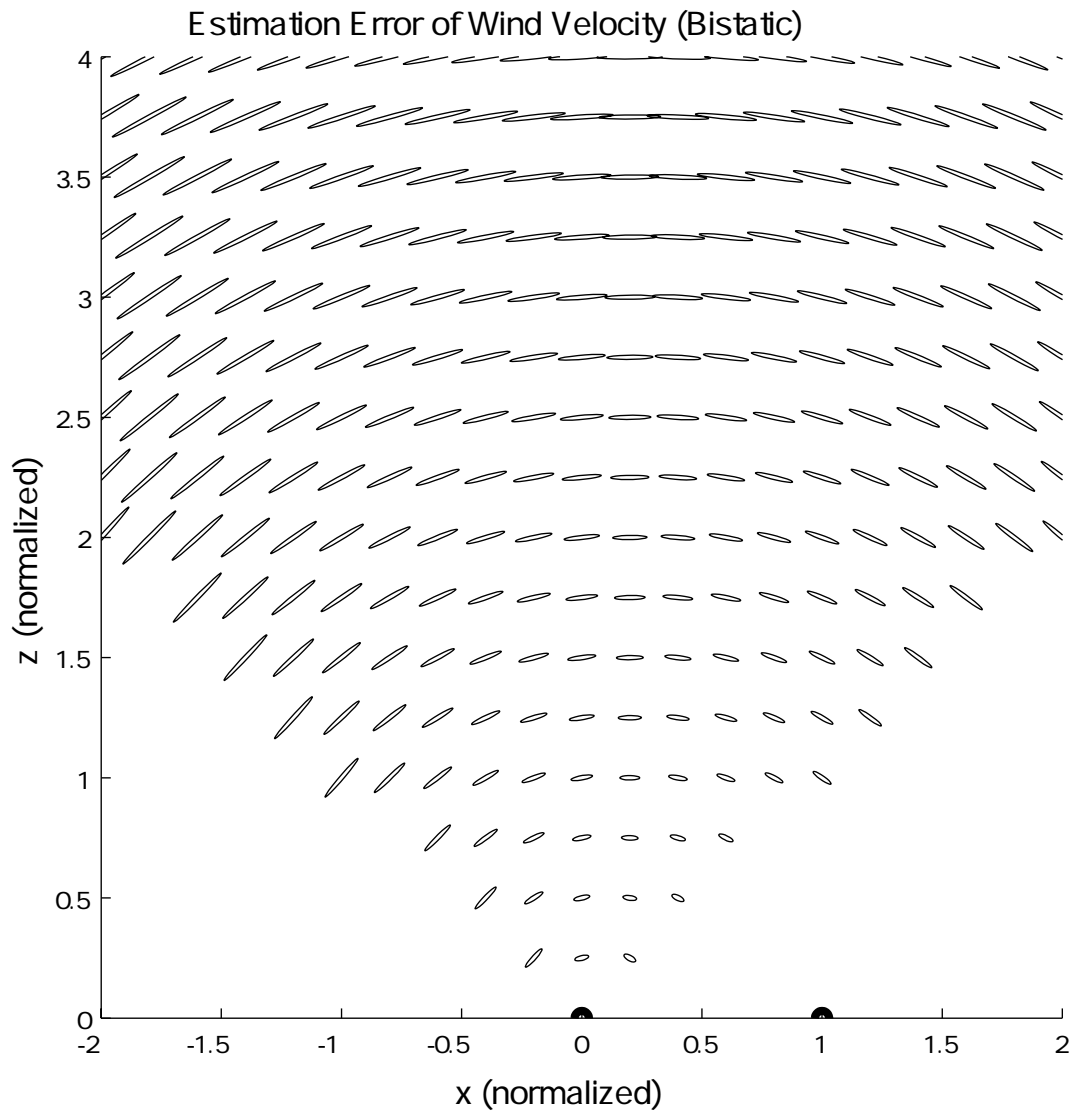


Figure 2.5: Error ellipses for a bistatic radar system in a two-dimensional representation. The main radar and the receiver are set at 0 and 1 in the x-axis, respectively.

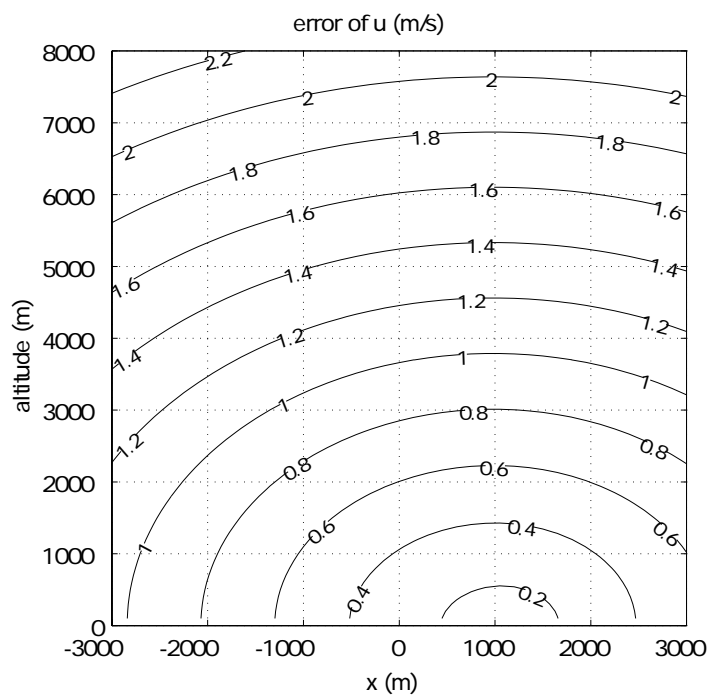


Figure 2.6: Horizontal component of the estimation error of the wind with a bistatic radar. The main radar is placed at 0 and the bistatic receiver is assumed to be set at 1,300m in the x-axis, according to the observations made in this study.

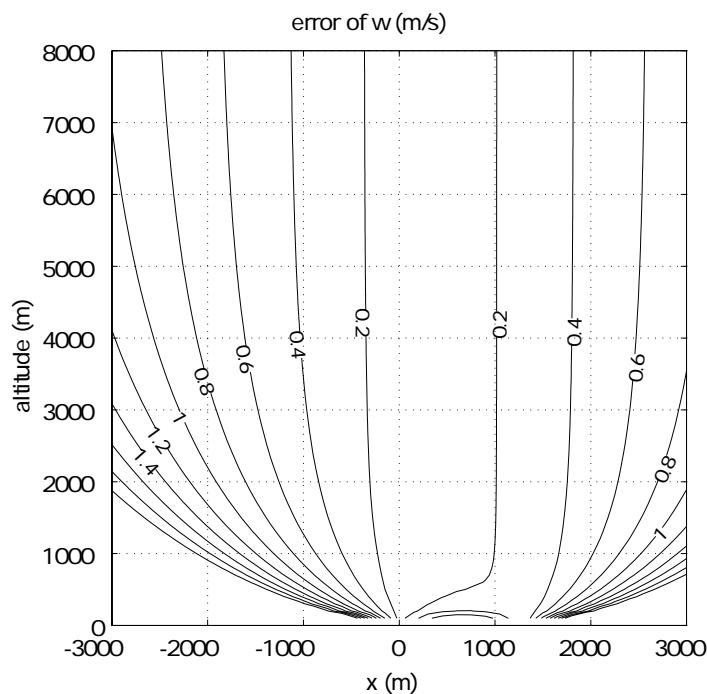


Figure 2.7: Vertical component of the estimation error of the wind under the same condition as in Fig. 2.6.

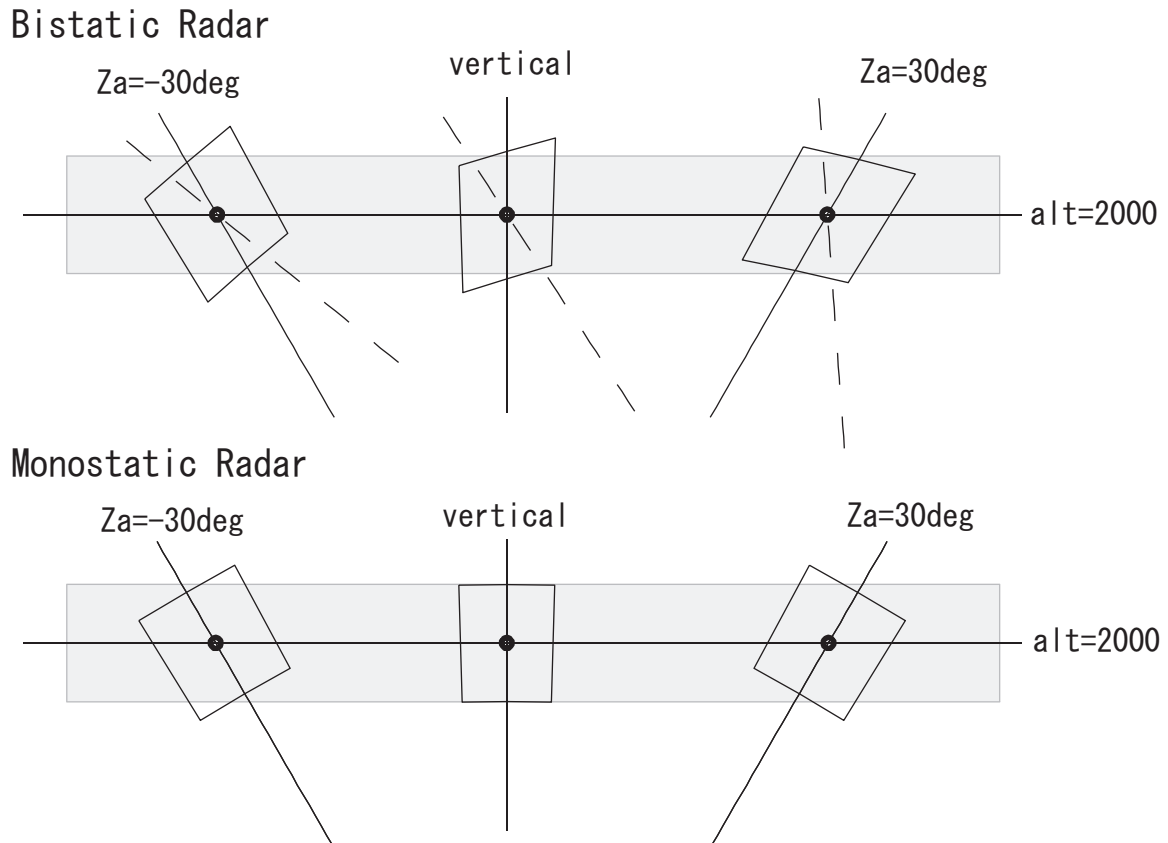


Figure 2.8: Shapes of the target in a bistatic and a monostatic radar. Illustrated for a case: altitude= 2000m, beam width is 3.4° , bistatic receiver position $x = 1300\text{m}$, and the zenith angles of the beam are -30,0 and 30 degrees. Solid lines and dashed lines which pass the horizontal line at the center of the volumes indicate the line-of-sight from the radar and the receiver, respectively. Shaded boxes show the thickness of 150m, which corresponds to the pulse width of $1\mu\text{s}$ that is used in this study.

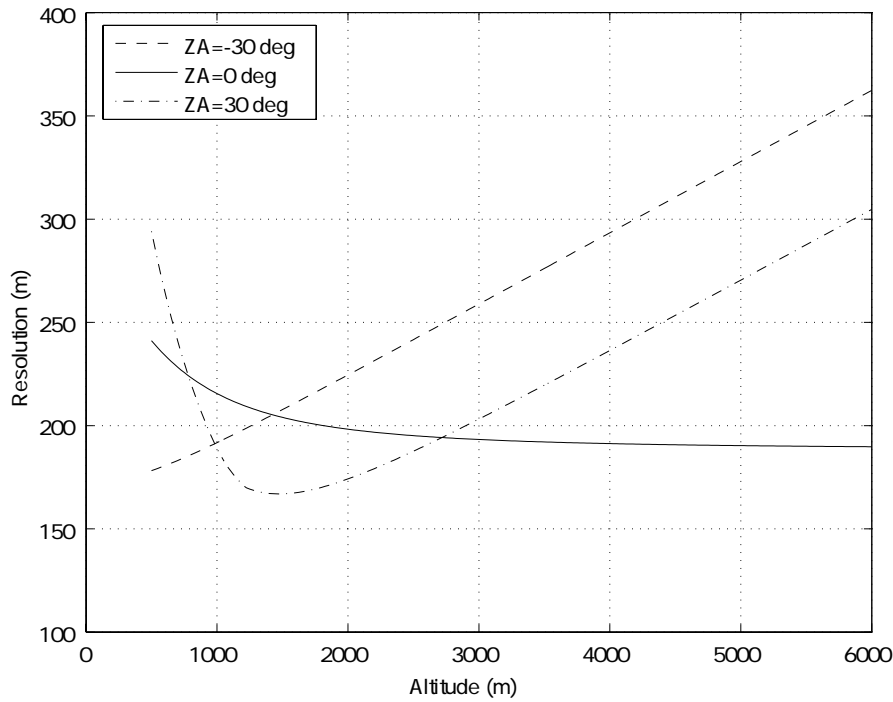


Figure 2.9: Vertical resolution for a bistatic radar. The beam width and the receiver position are assumed to be 3.4° and $x = 1300$ m, respectively. An omni-directional beam pattern is assumed for the receiver, to determine the edges of the volume.

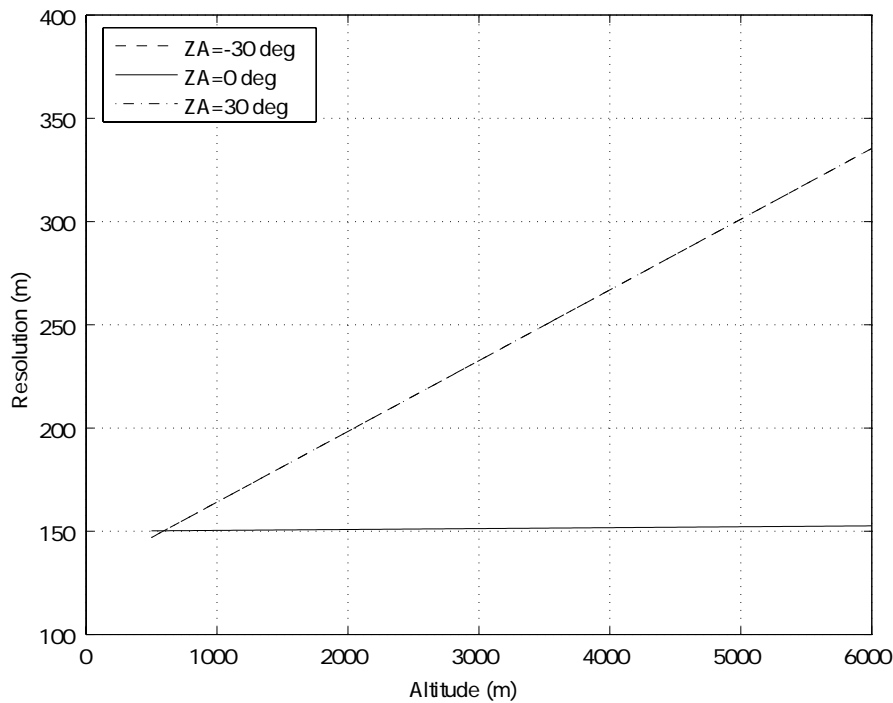


Figure 2.10: Vertical resolution for a monostatic radar. The beam width is assumed to be 3.4° . Only 1-way gain is utilized to calculate this graph.

Chapter 3

Adaptive Clutter Rejection

3.1 Introduction

Sidelobe canceling, or in a more general sense, adaptive antenna technique, has been an important issue in various fields of antenna engineering. It is now gathering a wide attention since the speed of signal processing devices has reached the level that enables real time processing required to practice the theory.

In atmospheric radar applications, where a sharp antenna beam is usually configured by a large array or aperture antenna, strong clutter echoes from surrounding mountains are the major source of interference. As the desired echoes from the atmosphere are so weak, even very weak echoes entering low level sidelobes can become a serious problem especially when they contain fluctuating components (Sato and Woodman, 1982). It has been a common practice to remove such undesired echoes in the off-line signal processing after the data is recorded.

A clear advantage of the adaptive antenna is that it makes use of extra information about the direction of arrival in discriminating undesired echoes in contrast to other clutter rejection schemes based on signal processing of the received echoes, such as adaptive filtering. As the adaptive filtering technique tries to remove the clutter after it is mixed with the desired echo, it cannot completely remove the clutter when the clutter has fading component. It also tends to "over-kill" the DC component of the desired echo, as is the case of observing the vertical direction. It is thus quite effective to cancel the clutter echo before it is mixed with the desired echo by modifying the antenna pattern adaptively.

However, conventional algorithms for the adaptive antenna have the serious defect of distorting the antenna main beam pattern when they are directly applied to atmospheric radars. The original sidelobe canceller by Howells (1965) may cancel the output of the main beam under extremely strong interference signal. This effect is mitigated by adding a limiter in its feedback loop (Abe *et al.*, 1995), but the threshold should be controlled according to the interference level. Since the sidelobe canceller is regarded as a type of adaptive antenna, Directionally Constrained Minimum Power (DCMP) algorithm (Takao

et al., 1976) can be used to suppress the sidelobe echoes while maintaining the desired signal. The same principle is also known as Minimum Variance Distortionless Response (MVDR) (Haykin, 2001). This idea is further utilized in a variety of Generalized Sidelobe Canceling (GSC) algorithms (Griffiths and Jim, 1982), which assure the response in the desired direction by controlling the weight of an output which does not contain desired signal. Efforts have been made to effectively delete the desired signal in this output by means of block filters (Fudge and Linebarger, 1996, Chu and Fang, 1999, Wang and Fang, 2000).

Performance of these algorithms depend on the characteristics of the desired signal, and the shape of the main beam may be altered when the cancellation is not complete. The main beam pattern is an essential design factor in the atmospheric radars since the target is widely distributed in space, and the ‘desired signal’ is defined as the echoes which return from the main lobe region. Even a slight change of the shape of the main beam will result in an offset of the estimated wind velocity.

Here we introduce a new sidelobe canceling algorithm (Kamio and Sato, 2003), which extends DCMP by introducing an additional constraint on the weight of the receiving array so that the main beam pattern of the radar is conserved. We demonstrate its effectiveness by applying the technique to actual data taken with the MU (Middle and Upper atmosphere) radar as the first attempt to introduce the adaptive antenna technique to atmospheric radar. Its performance and limitations for various types of clutters are examined with actual data as well as numerical simulations. We further examine the feasibility of rejecting non-stationary clutter such as reflection echoes from aircraft.

3.2 Proposed Algorithm

Received signal of a phased array is given by

$$y = W^H X \quad (3.1)$$

where X and W are the complex input signal vector and the weight vector, respectively. The output power is expressed in terms of the covariance matrix R_{xx} as

$$P = \frac{1}{2}[|y|^2] = \frac{1}{2}W^H X X^H W = \frac{1}{2}W^H R_{xx} W \quad (3.2)$$

Principle of DCMP algorithm(Takao *et al.*, 1976) is to minimize the output power under the constraint

$$W^H C = H^* \quad (3.3)$$

where C is the desired direction vector, and H is the constraint. Here we further apply an alternate condition

$$W^H W \leq U \quad (3.4)$$

which forces that the norm of the weight should be less than a given value U , which is set to be sufficiently lower than the main lobe level, but not so low as to affect the weight control of the sidelobe region. This second constraint assures that the entire main lobe pattern is not affected by the weight control. Here we call this algorithm as ‘DCMP Constrained Norm’ (DCMP-CN) in contrast to conventional DCMP.

The principle of DCMP-CN is thus expressed as

$$\min_W \left(P_{\text{out}} = \frac{1}{2} W^H R_{xx} W \right) \quad (3.5)$$

$$\text{subject to } C^T W^* = H \ \& \ W^H W \leq U \quad (3.6)$$

This minimization problem with an equality constraint and an inequality condition is solved by using penalty function method. The cost function is expressed as

$$Q_k(x) = f(x) + \rho_k \left(\sum_{i=1}^r (g_i(x))^2 + \sum_{r+1}^m (g_i(x))_-^2 \right) , \quad (3.7)$$

where $f(x)$ is the function to be minimized, $g_i(x) = 0$ gives an equality constraint, and $g_i(x)_- = 0$ gives an inequality constraint. Here $(a)_- = \min\{0, a\} = (a - |a|)/2$, r is the number of equality constraints, and $(m - r)$ is the number of inequality constraints.

We choose an arbitrary increasing series $\{\rho_k\}$ of the penalty factor which goes to infinity with increasing k . For each k , we minimize $Q_k(x)$ with a non-linear unconstrained optimization algorithm to obtain x_k starting from x_{k-1} . In actual processing, we set ρ_0 to the received signal power of a subarray element with randomly chosen weight value within the limit of the norm constraint for U , and let $\rho_k = 10\rho_{k-1}$ for $k = 1, \dots, 4$. We terminate the iteration at $k = 4$, where we obtain sufficiently stable solution.

The cost function for the current case is given by

$$\begin{aligned} Q_k(W) &= \frac{1}{2} W^H R_{xx} W + \rho_k [|W^H C - H|^2 + (U - W^H W)_-^2] \\ &= \frac{1}{2} W^H R_{xx} W + \rho_k [(W^H C - H)(C^H W - H^*) + (U - W^H W)_-^2] . \end{aligned} \quad (3.8)$$

The gradient of $Q_k(W)$ in terms of the weight vector W is given by

$$\nabla_w Q_k(W) = R_{xx} W + \rho_k [2C(C^H W - H^*) - 4W(U - W^H W)_-] . \quad (3.9)$$

3.3 Application to High Gain Arrays

Here we consider the application of DCMP-CN to the case of a high-gain antenna array consisting of several hundred elements. In such a case, it is not practical to control all of the elements. Instead, we select several antennas at the outer edge of the array to

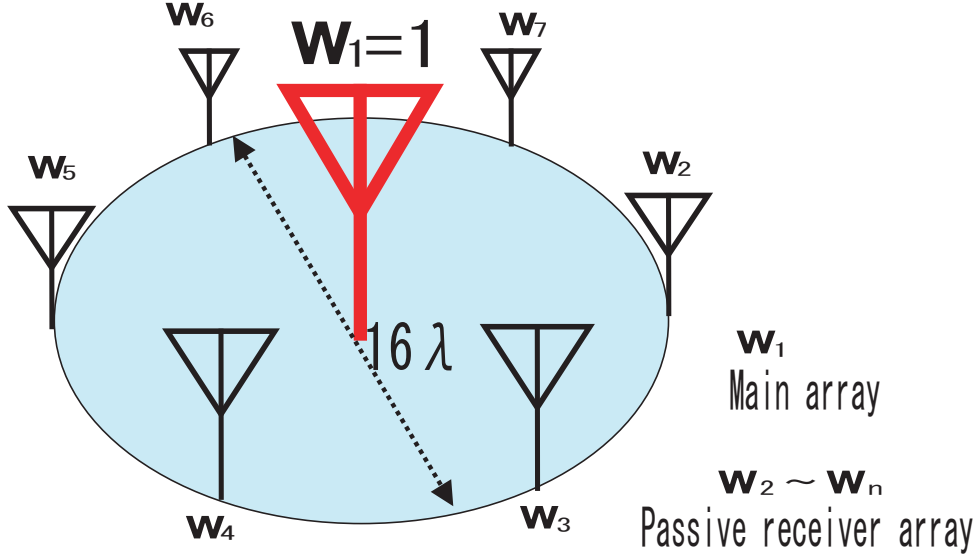


Figure 3.1: Configuration of a high-gain antenna with a peripheral receive-only sub-array.

configure a sub-array, and only control the weights of its elements as shown in Fig. 3.1, keeping the weight of the main array output to 1. In the radar application, the main array is used both for transmission and reception, and the sub-array is used only for reception. This configuration is useful in suppressing the clutter echoes of existing radar by adding several receiving antenna elements. In this case, the output power is rewritten as

$$P_{\text{out}} = \frac{1}{2} \mathbf{W}^H \mathbf{R}_{xx} \mathbf{W} = \frac{1}{2} (x_1 x_1^* + \mathbf{W}_{2:n}^H \mathbf{X}_{2:n} x_1^* + x_1 \mathbf{X}_{2:n}^H \mathbf{W}_{2:n} + \mathbf{W}_{2:n}^H \tilde{\mathbf{R}}_{xx} \mathbf{W}_{2:n}) \quad , \quad (3.10)$$

where subscript 1 denotes the output of the main array, and 2 to n correspond to sub array. Since the constraints are given only to the sub-array elements, the problem is expressed as

$$\begin{aligned} \min_{\mathbf{W}} \left(P_{\text{out}} = \frac{1}{2} (x_1 x_1^* + \mathbf{W}_{2:n}^H \mathbf{X}_{2:n} x_1^* + x_1 \mathbf{X}_{2:n}^H \mathbf{W}_{2:n} + \mathbf{W}_{2:n}^H \tilde{\mathbf{R}}_{xx} \mathbf{W}_{2:n}) \right) \\ \text{subject to } \mathbf{C}_{2:n}^T \mathbf{W}_{2:n}^* = \mathbf{H} \ \& \ \mathbf{W}_{2:n}^H \mathbf{W}_{2:n} \leq \mathbf{U} \quad . \end{aligned} \quad (3.11)$$

The cost function is then given by

$$\begin{aligned} Q_k(\mathbf{W}) = \frac{1}{2} (x_1 x_1^* + \mathbf{W}_{2:n}^H \mathbf{X}_{2:n} x_1^* + x_1 \mathbf{X}_{2:n}^H \mathbf{W}_{2:n} + \mathbf{W}_{2:n}^H \tilde{\mathbf{R}}_{xx} \mathbf{W}_{2:n}) \\ + \rho_k [(\mathbf{W}_{2:n}^H \mathbf{C}_{2:n} - \mathbf{H})(\mathbf{C}_{2:n}^H \mathbf{W}_{2:n} - \mathbf{H}^*) + (\mathbf{U} - \mathbf{W}_{2:n}^H \mathbf{W}_{2:n})^2] \quad . \end{aligned} \quad (3.12)$$

Table 3.1: Basic parameter of the MU radar.

Parameter	Value
Location	Shigaraki, Shiga, Japan (34.85°N, 136.10°E)
Radar system	monostatic pulse radar; active phased array system
Operational frequency	46.5 MHz
Antenna	circular array of 475 crossed Yagi's
aperture	8330 m ² (103 m in diameter)
beam width	3.6° (one way; half power for full array)
steerability	steering is completed in each IPP
beam directions	1657; 0°–30° off zenith angle
polarizations	linear and circular
Transmitter	475 solid state amplifiers
peak power	1 MW (maximum)
average power	50 kW (duty ratio 5%) (maximum)
bandwidth	1.65 MHz (maximum) (pulse width: 1–512 μ s variable)
Range resolution	150 m

3.4 Observations

We applied this algorithm to the data taken with the MU (Middle and Upper Atmosphere) radar. It is a large atmospheric radar with a flexible active phased array antenna consisting of 475 Yagi-Uda antennas (Fukao *et al.*, 1985a, b). Its main parameters are summarized in Table. 3.1.

The antenna array consists of 25 groups of hexagonal sub-array with 19 crossed 3-element Yagi antennas. A transmit/receive module is connected to each Yagi antenna. On reception, the RF signal at 46.5 MHz is converted to IF of 5 MHz at each module, and the output of 19 modules are combined at each group. Combined IF signals from 25 groups are sent to the control building, divided for 4 receiver channels. Each receiver can select and combine output from 25 groups at an arbitrary selection. Fig. 3.2 shows the outline of the signal processing system.

We made an experiment making use of this flexibility. Output from all groups except for 3 groups at the outer edge of the array is fed to a receiver as shown in Fig. 3.3. For the rest of 3 groups, only one antenna is activated in each group, and connected to three receivers.

Observation was made for about two hours of 6:45–7:56 JST and 17:18–18:21 JST on 26 December 2002 with 1- μ sec pulse transmissions at 400 μ sec intervals. The antenna beam was tilted 10° from the zenith, and tropospheric echoes were sampled from 1.5 km to

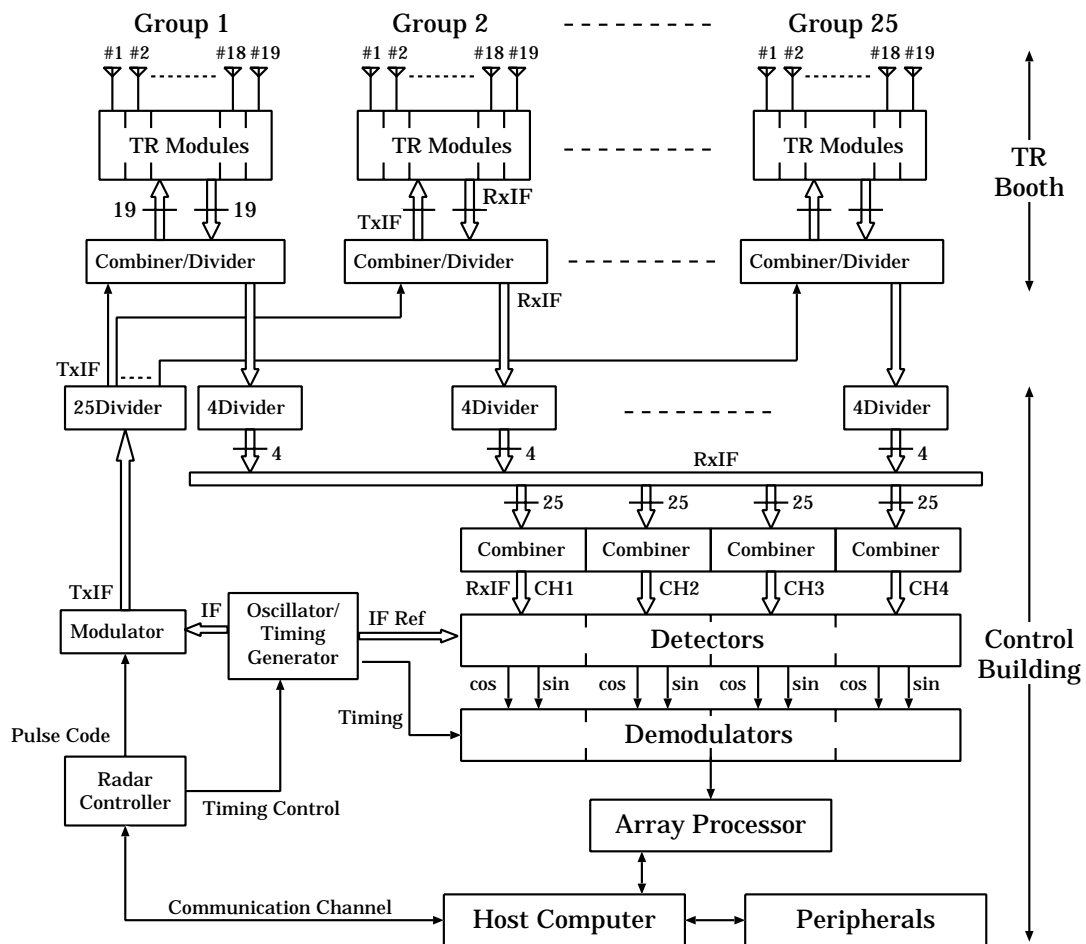


Figure 3.2: Receiver and signal processing system at the MU radar.

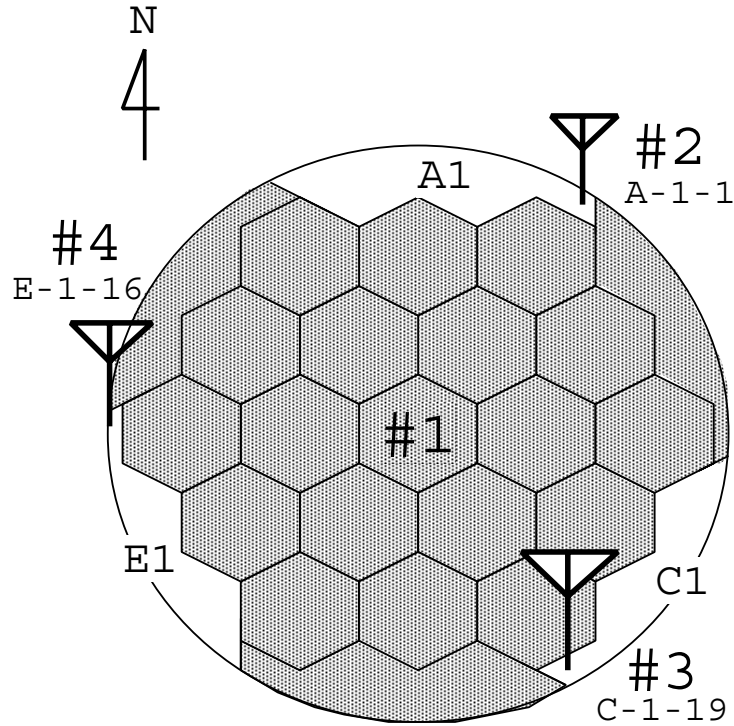


Figure 3.3: Antenna field configuration and antenna positions for the observation in this study.

9.6 km height region at 150-m sampling intervals. The received time series was averaged over 19 pulses for each range gate and recorded for off-line processing.

3.5 Clutter Suppression Using Real Data

Here we use the above data to examine the effectiveness of our proposed algorithm. The entire antenna array is regarded as the main antenna, and three antennas connected to other three receivers constitute the sub-array. The weight of the main channel is fixed, and the complex weight of the output from other three channels are varied so that the clutter echo is suppressed. By controlling the weight of only the sub-array, complexity of the adaptive processing is drastically reduced. Also, this system can be easily applied to existing radar systems.

The maximum constraint of the weight norm U is set to 0.5. In generating the covariance matrix R_{xx} , instantaneous samples are averaged with a decay factor of $\beta=0.997$, which is roughly equivalent to take the average of 1,000 samples. The appropriate values of U and β are discussed in more details in sections 3.6 and 3.7, respectively.

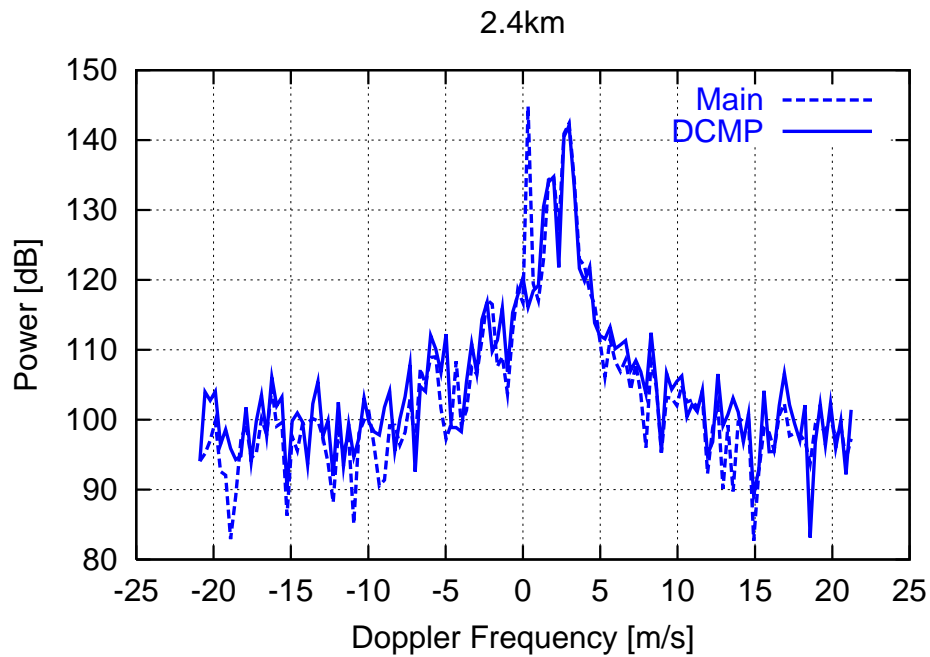


Figure 3.4: Doppler echo power spectrum at 2.4km range raw main beam data (dashed) and processed with conventional DCMP algorithm (solid). The y-axis indicates received power in arbitrary units.

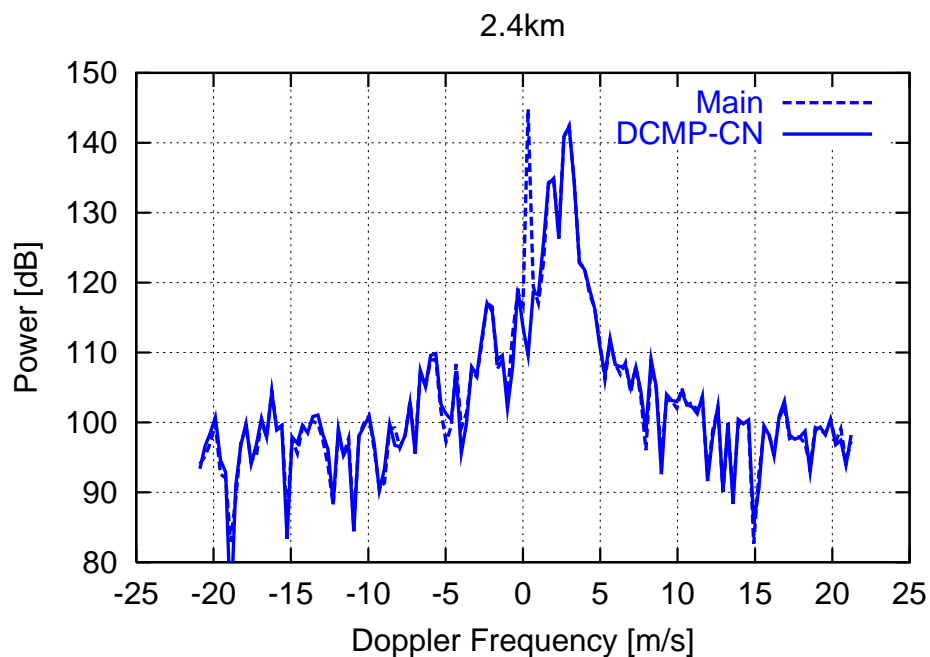


Figure 3.5: Doppler echo power spectrum at 2.4km range raw main beam data (dashed) and processed with the proposed DCMP-CN algorithm (solid).

Fig. 3.4 shows an example of the echo power spectrum. The spectrum was generated by applying 128-point FFT to a time series of 9.7 s after coherent integration of 190 pulse samples. No incoherent integration is applied. The vertical scale is in an arbitrary unit, and the galactic background noise level is about 100dB. The dashed line shows the original spectrum with the main antenna. The sharp spike at zero Doppler velocity is the clutter component, while a broad peak with positive Doppler shift is the desired echo. The solid line shows the result of conventional DCMP, with which the clutter is suppressed with a penalty of increased noise level.

Fig. 3.5 shows the same spectrum processed with the proposed DCMP-CN algorithm. The solid line exactly follows the desired signal component by rejecting the clutter component only. It should be noted that we assume no information on the echo power spectrum such as the narrow clutter spectrum. It is therefore possible to cancel not only the DC clutter, but also clutters with fading as far as its time constant is long enough compared to the time required to obtain the covariance matrix.

The increased noise level with the conventional algorithm is due to large weight of the sub-array elements, which enhanced the galactic noise level and also atmospheric echoes entering low elevation sidelobes, which spreads out in a broad Doppler spectrum. On the other hand, the proposed DCMP-CN algorithm effectively suppresses such increase by controlling the weight of the sub-array elements. This example clearly demonstrates the usefulness of adaptively controlling the antenna pattern with a sub-array configuration.

It should be noted that the adaptive cancellation needs to be applied separately for different range gates and beam directions. In this manner, clutters from various directions can be suppressed with a small number of sub-array elements, as far as they have different range from the radar. As the computational load of the proposed algorithm is very light, more than 1,000 time series corresponding to different range gates and beam directions can be handled simultaneously with a personal computer.

3.6 Considerations on the Constraints

In the previous section, we set the maximum norm constraint U to 0.5. Here we examine the appropriate range of this value, and also the relative importance of the norm constraint over the directional constraint.

The proposed DCMP-CN algorithm has the advantage that the control parameter U can be chosen regardless of the strength of the desired and undesired signals, since it is determined simply by the relative pattern of the main and sub-array antennas. However, there is a certain range of U that gives the best performance.

If we set U to a too large value, the DCMP-CN algorithm approaches to DCMP, and thus becomes unable to suppress the increase of the noise level as shown in Fig. 3.4. On the other hand, if we set U to a too small value, the algorithm may not be able to cancel the clutter component by the combined output of sub-array elements.

We first consider a case where the output of a sub-array element is added to that of the main array consisting of M elements. We assume that the sub-array element is the same as that of the main array, and the output is in phase for the main beam direction. Also, in Eq. (3.10) we implicitly assumed that the output of the sub-array element is normalized to that of the main array at the isotropic-gain level. In the VHF range, where the noise is dominated by the galactic background radiation, it is equivalent to normalize them by their noise level.

In this case, the signal power after adding the sub-array element increases by $(\sqrt{M} + 1)^2/M$ times, while the noise level increases by a factor of 2. The gain of the signal-to-noise ratio by adding a sub-array element is thus given by

$$G_{\text{SNR}} = \frac{(\sqrt{M} + 1)^2}{2M}, \quad (3.13)$$

which is roughly -3dB for a large M .

Next we consider a more general case where the sub-array element has a relative gain of G_s in the main beam direction of the main-array element, the output power of the sub-array element is multiplied by U before addition, and it may not be in phase with the main array. In this case, Eq. (3.13) becomes

$$G_{\text{SNR}} = \frac{(\sqrt{M} + \alpha\sqrt{G_s U})^2}{(1 + U)M}, \quad (3.14)$$

where α takes a value between -1 and 1, and is 1 for the case where two signals are in phase, 0 for the orthogonal phase, and -1 for the opposite phase. This situation corresponds to the worst possible case of the proposed algorithm with norm constraint value of U . Although we have examined only the case of one antenna element, Eq. (3.14) can also be applied to a sub-array consisting of multiple antenna elements, because the norm constraint U limits the sum of the weight of sub-array elements.

In the case shown in Fig. 3.5, $G_s = 1$ (0dB) and $U = 0.5$, which gives G_{SNR} of -1.5dB. However, the actual loss is much less than this value as is clear from the figure, because Eq. (3.14) gives the worst case. Fig. 3.6 shows G_{SNR} versus U for the case of $M = 475$, assuming the MU radar, and $G_s = U$.

Apparently, a small constraint is desirable in order to assure a small loss in SNR. If we allow a loss of up to 0.5dB, the norm constraint U should be set to 0.135, 0.120, and 0.105 for the in-phase, orthogonal, and the out-of-phase cases, respectively. As we assumed that the antenna element used for the sub-array has a gain of $G_s = U$ relative to that for the main-array element, it means that the sub-array element should have a relative gain of -9.2dB in the main lobe direction for $U = 0.12$. In the case of the MU radar, as a typical example of VHF MST radars, 3-element Yagi antenna elements with an isotropic gain of 7.2dB are pointed to the zenith, and the main lobe is steered in an angular region of 30° from the zenith. An isotropic gain of less than -2dB is easily achieved in this angular

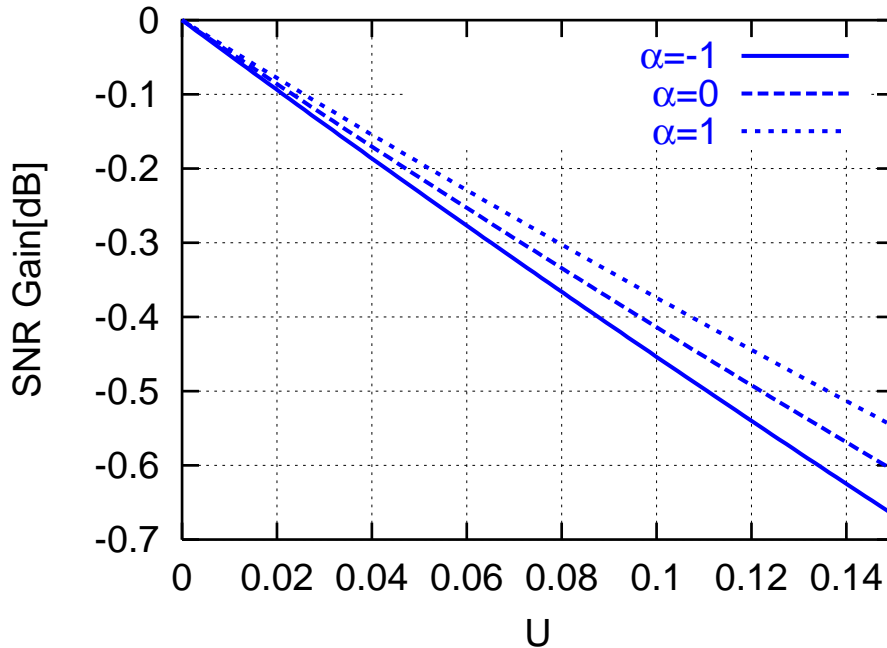


Figure 3.6: SNR loss as a function of constrained norm value U .

region by pointing the same element to the horizontal direction, for example. If a specially designed antenna element which has less sensitivity to the main lobe region is used for the sub-array element, a larger value of U becomes acceptable.

If we apply the proposed DCMP-CN algorithm, the sub-array elements should always be kept in phase with the main antenna because of the directional constraint. The orthogonal and the out-of-phase cases examined above correspond to situations where this constraint is not applied. Fig. 3.6 shows that if we remove the directional constraint from the algorithm with $U = 0.12$, we further lose about 0.13dB, or 3%, of the sensitivity. The advantage of not applying the directional constraint is that a simpler algorithm with only the norm constraint can be used, and that no phase calibration is required for the sub-array elements.

3.7 Suppression of Clutter from Moving Targets

The example shown in the previous section clearly demonstrates the usefulness of the proposed method in rejecting the clutter from stationary targets. As we mentioned, the same algorithm can be applied without any problem to the cases where the undesired echoes are fading as long as they have no correlation with the desired echo.

However, if the direction of arrival of the undesired echoes change in time, as is the case

for the clutter echoes from aircraft or the coherent echoes from ionospheric irregularities, for example, the algorithm has to catch up with this change by modifying the antenna pattern. This limits the time that can be used to average the covariance matrix R_{xx} .

Here we examine a case of aircraft echo, which is the most typical undesired echo with rapid motion for the MST radar environment. As for the MU radar, the major source of aircraft clutter is regular customer jet planes, whose closest route is about 7km from the radar site. Although the aircraft echoes are received through low elevation sidelobes, they are much stronger than the desired weak scattering from atmospheric turbulence.

If we consider a jet plane flying on a linear route whose minimum distance from the radar is 7km at a speed of 280m/s, its maximum angular motion is $2.3^\circ/\text{s}$ at its closest point. Fig. 3.7 shows an example of the echo power spectrum with an aircraft at its closest range of 7.05km. The received data are first coherently averaged for 190 pulses (=76ms), and the power spectrum is computed by using 128-point FFT, then incoherently averaged for 10 times (=7.6s), as is the case for Figs. 3.4 and 3.5. The atmospheric echo was below the noise level on this day at this range, so only the clutter echoes from the aircraft and mountains are present. The dashed line is the original power spectrum observed by the main antenna. As the Doppler velocity of the aircraft echo changes from +42m/s to -42m/s in an interval of 7.6s around its closest point, its echo power spreads over the entire spectral window.

The solid line is after processing by the proposed algorithm with the sub-array signals. In this case the covariance matrix R_{xx} was averaged with the decay factor $\beta = 0.7$, which corresponds to an averaging over only about 10 data samples compared to about 1000 samples used in the previous section, in order to adjust to the rapid motion of the target. The stationary clutter component at 0 Doppler shift is suppressed by 12dB, and the aircraft echo is suppressed by about 15dB. The small reduction in the stationary clutter component is apparently due to the small number of samples averaged to form the covariance matrix. The suppression of the moving clutter component is also limited, but has a substantial effect in estimating one-hour mean wind profiles, for example, because the remaining clutter component can be further suppressed by incoherent integration over one hour period.

One possible means of further reducing the aircraft echoes is to employ faster sampling. Fig. 3.8 is the same as Fig. 3.7 except that the coherent integration time is reduced to 19 times instead of 190. The decay factor and the number of FFT is kept the same, so everything is computed based on 10 times faster sampling and shorter duration. It should be noted that the maximum Doppler velocity is thus 10 times larger, and the power level is 20dB lower because the number of coherent addition is 1/10.

As the Doppler velocity of the aircraft changes only by 8.4m/s during the 0.76s period used for computation, its echo appears as a clear spike at around -40m/s. The peak at +40m/s is its spectral image due to gain imbalance of the two orthogonal channels of the receiver. The aircraft echo is reduced by about 40dB after the adaptive suppression as shown by the solid line. Since the spectral image component is generated inside the

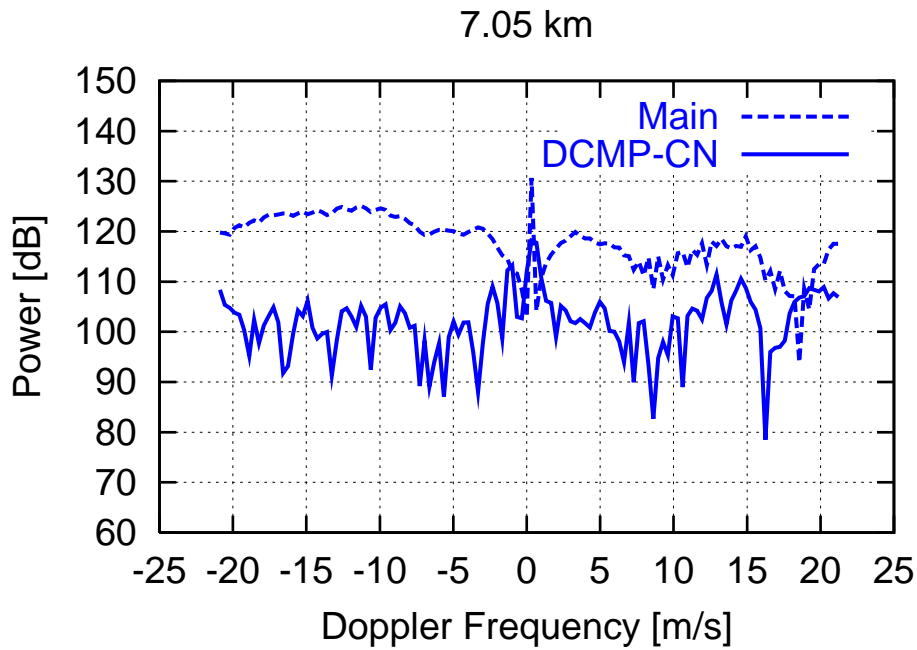


Figure 3.7: Example of the Doppler echo power spectrum with strong aircraft echo at a sampling interval of 76ms from raw main beam data (dashed) and with proposed DCMP-CN algorithm (solid). The y-axis indicates received power in arbitrary units.

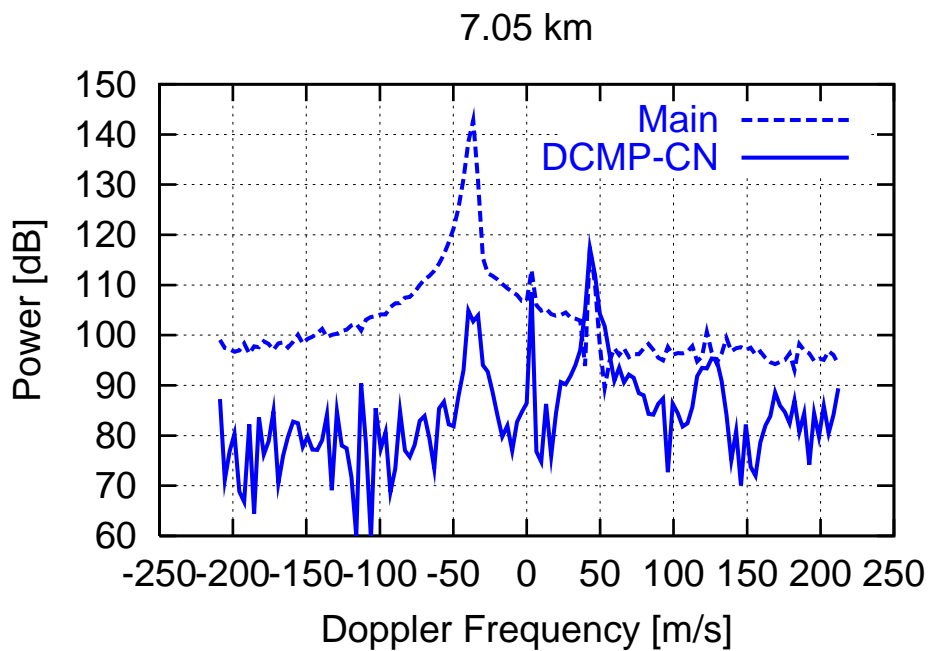


Figure 3.8: Same as Fig.3.7, but for a sampling interval of 7.6ms.

receiver, it cannot be cancelled by the adaptive algorithm, which naturally assumes an ideal receiver and generates a pure signal without the image in cancelling the clutter.

The reason that the stationary clutter from mountains is even less suppressed compared to Fig. 3.7 is probably that the relative magnitude of the mountain echo to the aircraft echo is smaller than the previous case, and the number of sub-array element (=3) is not large enough to cancel this weak interference.

3.8 Averaging of the Covariance Matrix

The examples presented in the previous section clearly show the effectiveness of reducing the time used for adaptation in order to suppress clutter echoes from moving target. On the other hand, reducing the degree of averaging in estimating the covariance matrix R_{xx} causes inaccurate estimation of the signal characteristics, which results in an incomplete cancellation of undesired signals.

Here we examine the effect of the degree of averaging on the performance of the algorithm via numerical simulations. We assume a sub-array consisting of three elements as the actual observation presented in this study. The main beam direction is 10° from the zenith, and a stationary clutter arrives from zenith angle of 75° . The echo power of the desired and interference signals are set to 0dB and 70dB, respectively. The main beam has a one-way gain of 34dB.

As the accuracy of estimating the covariance matrix will be strongly affected by the magnitude of phase rotation of the signal due to Doppler effect, we consider three cases of the line-of-sight Doppler velocity of 0.0m/s, 0.33m/s, and 2.3m/s. Signal is coherently added for 190 pulse samples, or 76ms, before processing. Fig. 3.9 shows the depth of the null in the direction of the clutter assuming that the desired signal and the clutter are pure sinusoid.

For the case of 0.0m/s, there is no means to discriminate the desired signal from the clutter because they are both sinusoid of the same frequency. The algorithm thus cancels the clutter by controlling its amplitude equal to that of the desired signal, and with opposite phase. As the main beam has a gain of 34dB, the undesired clutter component with 70dB higher level is cancelled by controlling the antenna gain to this direction to -36dB, as shown in this figure. Apparently, a larger suppression is required in order to detect the desired signal.

The suppression rapidly increases as the Doppler velocity and the degree of averaging increases. The periodicity found in other cases than zero Doppler agrees with the period of the given phase rotation of the signal. It is found that the number of phase rotation needed to obtain the SIR (Signal-to-Interference Ratio) of 25dB, 30dB, and 35dB during the averaging period is about 5 cycles, 9 cycles, and 17 cycles, respectively.

Since the actual atmospheric echo has a finite spectral width, we also examined such cases. Fig. 3.10 is the same as Fig. 3.9, but the signal has a Gaussian spectrum with

the half-power width of 0.33m/s. The suppression for both 0.33m/s and 2.33m/s cases are roughly equal to those cases in Fig. 3.9, indicating that the mean phase rotation is more important than random phase changes. For the case of zero Doppler shift, however, a steady increase of suppression is found as the degree of averaging increases. This is the effect of the random phase variation. Fig. 3.11 shows the depth of the null for zero mean Doppler velocity and various spectral width. This situation is encountered when the antenna beam is pointed to the zenith in order to observe the vertical wind velocity. It is thus important that the clutter echoes from mountains, which overlaps with the atmospheric echo power spectrum, can be suppressed by this method. For a typical spectral width of 0.33m/s, SIR of 15dB can be obtained by averaging for 10,000 times, or 12.7 minutes.

This integration time is not a problem for stationary targets as mountains, but is clearly not consistent with requirements for suppression of aircraft echoes. We need to develop algorithms which can deal with these different types of interferences simultaneously. A possible solution is to estimate R_{xx} for ground clutters while no aircraft echo is present, and switches to another mode when an aircraft is detected. In the aircraft mode, the aircraft is tracked by an airborne tracking method (Sato (2000), Blackman (1999), for example.), and a null constraint toward the aircraft is applied. This is due to the fact that an aircraft can be regarded as a point source while the direction of ground clutters are apt to spread and a directional null constraint is not suitable.

3.9 Summary

In this study, we applied an adaptive sidelobe suppression algorithm developed for a high-gain antenna to actual data taken by the MU radar as the first attempt to introduce the adaptive antenna technique to atmospheric radar, and confirmed its effectiveness in suppressing the clutter echoes from mountains.

By constraining the weight norm of the sub-array as well as the response of the main antenna to the desired direction, good cancellation of undesired signal is achieved without disturbing the main beam pattern. It should be noted that the proposed algorithm does not require any knowledge on the input signal spectrum.

The proposed method can be easily implemented to existing high-gain antenna systems by adding a small number of receiving antenna elements and a personal computer which performs all necessary computation and control.

Considerations are made on the value of the norm constraint U to achieve the best performance. One of the advantages of the proposed algorithm over other adaptive antenna algorithms is that the controlling parameter is independent of the strength of the interference signal, and depends only on the antenna pattern of the main antenna and the sub-array.

We further examined the possibility of suppressing the aircraft echoes, which rapidly

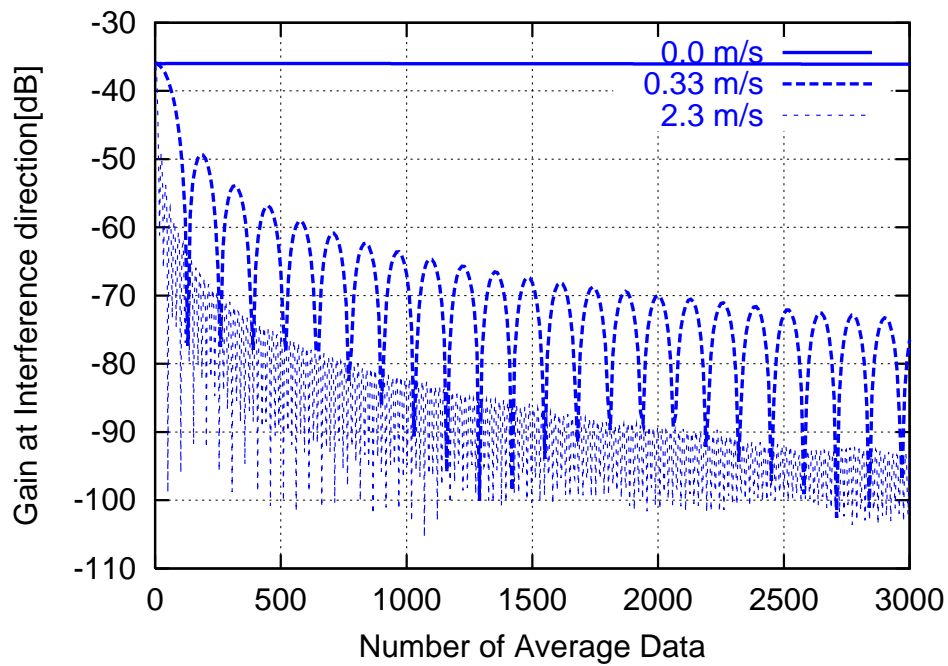


Figure 3.9: Gain in direction of interferer for monochromatic signals with different Doppler velocities.

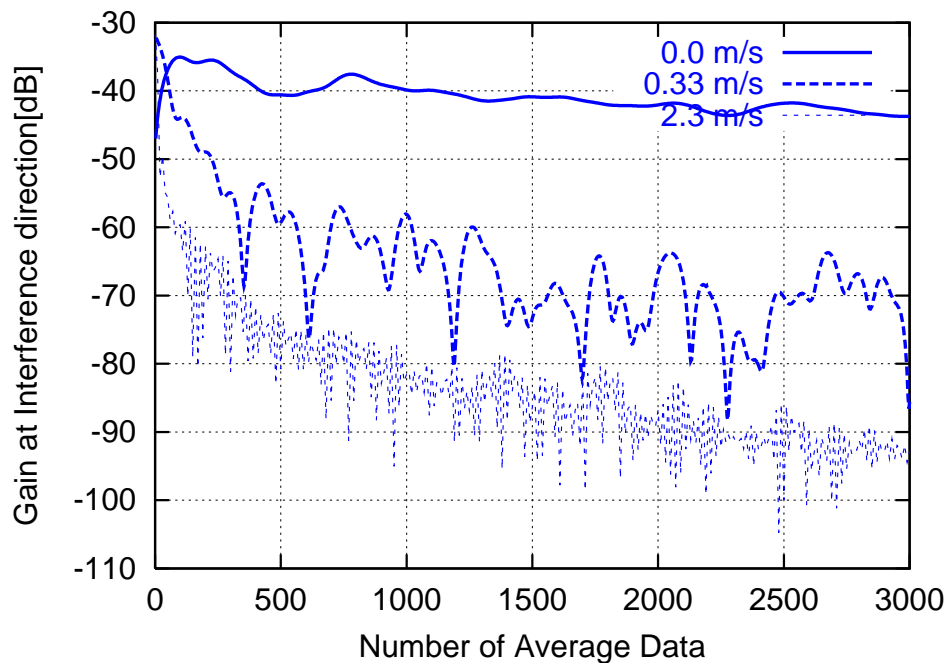


Figure 3.10: Same as Fig.3.9, but for the interferer with spectral width of 0.33m/s.

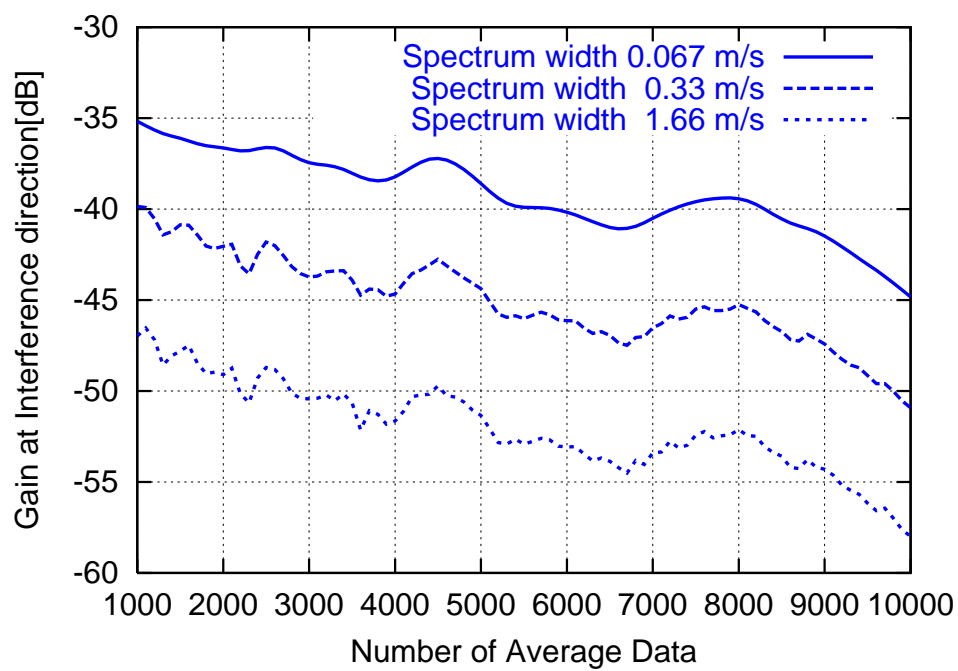


Figure 3.11: Gain in direction of interferer for signals with different spectral width when no mean motion is present.

change their direction of arrival. It is found that it is effective to reduce the time used for averaging the covariance matrix R_{xx} in order to suppress such echoes. However, it contradicts the requirement for suppressing the mountain echoes under a condition of a small Doppler velocity of the atmospheric echo. A different approach is needed to simultaneously cope with these different types of interferences. The effectiveness of the proposed algorithm should be further evaluated with larger data sets at various atmospheric radar situations. For this purpose, we are currently developing digital receive-only array systems to be implemented to the MU radar, and also to the Equatorial Atmosphere Radar in Indonesia.

Chapter 4

Arrangement of Antenna Array

4.1 Introduction

For phased array applications, namely mobile communications, radar, radio telescope and so on, uniformly spaced antenna arrays are the types that have most commonly been utilized. This is because a uniform spacing array has an outstanding performance in terms of average sidelobe response. For two-dimensional array applications, it is generally recognized that the array with a triangular arrangement is the best in this respect.

However, a uniformly arranged array has grating-lobes within its visible region that appear when the mainlobe is tilted. Since a certain distance between one antenna to another is needed for electromagnetic reasons, it is limited to shorten the distance to drive grating-lobes out of the visible region. Hence an optimization is required to arrange an array satisfying these conditions.

Adaptive signal processing techniques for linear sum array, whose system is simply described as

$$\begin{aligned} s(t) &= \sum_{n=1}^N w_n^* s_n(t) \\ &= \mathbf{w}^H \mathbf{s}, \end{aligned} \tag{4.1}$$

where w_n , $s_n(t)$ are the weight and received signal of n -th antenna, respectively, have several different principles according to criteria. The principle of Minimum Mean Square Estimation (MMSE) algorithm is to find a weight vector which minimizes the mean squared error of the resulting signal toward its replica. The solution is given by

$$\mathbf{w}_{\text{MMSE}} = R_{ss}^{-1} \mathbf{r} \tag{4.2}$$

where R_{ss} is a correlation matrix of \mathbf{s} and \mathbf{r} is a vector whose elements are correlations between the replica and input signals.

MMSE results in gathering all the split desired signals which arrive from separate directions with random phases hence it is desirable for mobile communications under multipath environment. However, the gains and phases against incident signals become linearly dependent if their directions-of-arrival (DOA) satisfy the relation of those among mainlobe and grating-lobes. That causes a situation that the algorithm can not cancel an interference if it comes into a grating-lobe, as well as the case some directionally separate desired signals cancel out each other.

Minimum Variance Distortionless Response (MVDR), which is described as a class of Linearly Constrained Minimum Variance (LCMV), is one of the most commonly used algorithm in radio telescope and radar/sonar. The evaluation function of this algorithm is set as,

$$\underset{\mathbf{w}}{\text{minimize}} [P = \mathbf{w}^H R_{ss} \mathbf{w}] \quad (4.3)$$

$$\text{subject to } \mathbf{w}^H \mathbf{c} = 1. \quad (4.4)$$

Its well-known optimal weight \mathbf{w}_{opt} for an array is written as

$$\mathbf{w}_{\text{opt}} = \frac{R_{ss}^{-1} \mathbf{c}}{\mathbf{c}^H R_{ss}^{-1} \mathbf{c}} \quad (4.5)$$

where \mathbf{c} is the steering vector which aims the main beams at the desired direction. This algorithm leads to canceling all the signals in sidelobe such as interference or clutters, while it maintains the gain constant toward the desired direction.

However, in case the array has grating-lobes, it is impossible to control the response independently toward them. Consequently, undesired signals will not be suppressed. Let $\beta(\boldsymbol{\theta})$ be the normalized beam-space response function ($\beta(\boldsymbol{\theta}) = 1$ when $\boldsymbol{\theta}$ matches a grating-lobe or the mainlobe) toward a direction $\boldsymbol{\theta} = (\theta_x, \theta_y)$. Regarding a case in which a strong clutter arrives from the direction $\boldsymbol{\theta}$, a resulting SNR ρ of output after synthesized by MVDR is approximately described as

$$\rho = N\rho_0(1 - |\beta(\boldsymbol{\theta})|^2) \quad (4.6)$$

where N is the number of antennas and ρ_0 is the SNR for each antenna. This expression supports the necessity of constructing an array displacement which does not have grating-lobes within the visible region.

Since the gain of desired is set to be constant as in eq.(4.4), the reduction of SNR is inversely proportional to increment of noise power. Now we set an input signal omitting the desired signal for simplicity as,

$$\mathbf{s} = \rho\mathbf{c} + \sigma\boldsymbol{\nu} \quad (4.7)$$

where \mathbf{c} is a clutter signal vector, $\boldsymbol{\nu}$ is a random signal vector whose elements follows the normal probability distribution function $N(0, 1)$, ρ and σ are their amplitudes. Note that \mathbf{c} is a steering vector such that

$$\mathbf{c}_d = [\exp(j2\pi\mathbf{x}_1 \cdot \boldsymbol{\eta}_d), \exp(j2\pi\mathbf{x}_2 \cdot \boldsymbol{\eta}_d), \dots, \exp(j2\pi\mathbf{x}_N \cdot \boldsymbol{\eta}_d)]^t.$$

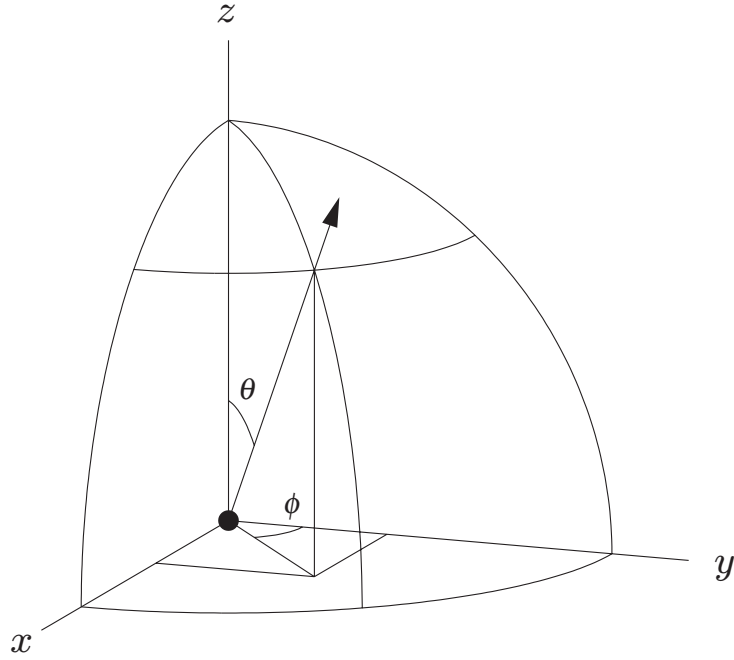


Figure 4.1: Definition of θ (zenith angle) and ϕ (azimuth). An array is placed within x-y plane.

4.2 System Definition

A plane wave observed at (X, Y, Z) that arrives from a direction (Zenith angle, Azimuth) = (θ, ϕ) in Fig.4.1 is described as a complex signal

$$c(X, Y, Z, \theta, \phi) = \exp \left[j \frac{2\pi}{\lambda} \left(\sin \theta \sin \phi \quad \sin \theta \cos \phi \quad \cos \theta \right) \begin{pmatrix} X \\ Y \\ Z \end{pmatrix} \right]$$

where λ is the wavelength. In this chapter, we target a planer array ($Z = 0$) and this equation is rewritten utilizing normalized coordinates $(x, y, z) = (X/\lambda, Y/\lambda, Z/\lambda)$ as

$$c(\mathbf{x}, \boldsymbol{\eta}) = \exp(j2\pi\boldsymbol{\eta} \cdot \mathbf{x})$$

where \mathbf{x} and $\boldsymbol{\eta}$ are two-dimensional variables

$$\mathbf{x} = \begin{pmatrix} x \\ y \end{pmatrix}$$

$$\boldsymbol{\eta} = \begin{pmatrix} \eta_x \\ \eta_y \end{pmatrix} = \begin{pmatrix} \sin \theta \sin \phi \\ \sin \theta \cos \phi \end{pmatrix}.$$

Note that $\boldsymbol{\eta} = \mathbf{0} = (0, 0)^t$ represents the zenith. The visible region for a planer array corresponds to the zenith angle of from $\theta = 0^\circ$ to $\theta = 90^\circ$ and equivalently

$$|\boldsymbol{\eta}| \leq 1.$$

Utilizing Dirac's delta function that is positive infinite at which an antenna is placed, we have an *antenna displacement function* as,

$$a_0(\mathbf{x}) = \sum_{n=1}^N \delta(\mathbf{x} - \mathbf{x}_n).$$

where \mathbf{x}_n is the position of n -th antenna. To examine a response of the array, we define an *antenna function*

$$a(\mathbf{x}) = a(\mathbf{x}, \boldsymbol{\eta}_d) = \sum_{n=1}^N c^*(\mathbf{x}, \boldsymbol{\eta}_d) \delta(\mathbf{x} - \mathbf{x}_n). \quad (4.8)$$

which represents an array steered to a desired direction $\boldsymbol{\eta}_d$ with uniform excitation.

The output of the antenna array $a(\mathbf{x}, \boldsymbol{\eta}_d)$ with an incident signal $c(\mathbf{x}, \boldsymbol{\eta}_i)$, which arrives from a certain direction $\boldsymbol{\eta}_i$, is described by

$$\begin{aligned} s(\boldsymbol{\eta}_d, \boldsymbol{\eta}_i) &= \int a(\mathbf{x}, \boldsymbol{\eta}_d) c(\mathbf{x}, \boldsymbol{\eta}_i) d\mathbf{x} \\ &= \int \sum_{n=1}^N [c^*(\mathbf{x}, \boldsymbol{\eta}_d) \delta(\mathbf{x} - \mathbf{x}_i)] c(\mathbf{x}, \boldsymbol{\eta}_i) d\mathbf{x} \\ &= \sum_{n=1}^N \exp[j2\pi(\boldsymbol{\eta}_i - \boldsymbol{\eta}_d) \cdot \mathbf{x}]. \end{aligned}$$

Obviously, the output becomes maximum $s(\boldsymbol{\eta}_d, \boldsymbol{\eta}_i) = N$ for $\boldsymbol{\eta}_d = \boldsymbol{\eta}_i$. If we see $s(\boldsymbol{\eta}_d, \boldsymbol{\eta}_i)$ in eq.(4.9) as a function of $\boldsymbol{\eta}_i$, the equation can be interpreted as a spatial response of the array; we rewrite the function as $b(\boldsymbol{\eta})$ in this regard. Therefore, the response $b(\boldsymbol{\eta})$ of the antenna array $a(\mathbf{x})$ is defined by a two-dimensional Fourier Transform pair:

$$\begin{aligned} b(\boldsymbol{\eta}) &= \int a(\mathbf{x}) \exp(j2\pi\boldsymbol{\eta} \cdot \mathbf{x}) d\mathbf{x} \\ a(\mathbf{x}) &= \int b(\boldsymbol{\eta}) \exp(-j2\pi\boldsymbol{\eta} \cdot \mathbf{x}) d\boldsymbol{\eta}. \end{aligned}$$

Hereafter, $b(\boldsymbol{\eta})$ is also referred to as a *beam function*. By these equations, we also have a response $b_0(\boldsymbol{\eta})$ such that

$$a_0(\mathbf{x}) \stackrel{\mathcal{F}}{\Leftrightarrow} b_0(\boldsymbol{\eta}).$$

When the main beam is steered to a direction $\boldsymbol{\eta}'$ in eq.(4.8), the corresponding beam function is

$$b(\boldsymbol{\eta}) = b_0(\boldsymbol{\eta} - \boldsymbol{\eta}').$$

Then, the visible region for b_0 is given by $|\boldsymbol{\eta} - \boldsymbol{\eta}'| \leq 1$. If we allow the main beam direction $\boldsymbol{\eta}'$ to steer within $0 \leq \theta \leq \theta_s$, the envelope of the region defined by $|\boldsymbol{\eta} - \boldsymbol{\eta}'| \leq 1$ becomes the inside of

$$|\boldsymbol{\eta}| \leq 1 + \sin \theta_s.$$

Especially, when $\boldsymbol{\eta}'$ is allowed to steer within all the possible directions $0 \leq \theta \leq \pi/2$, the entire visible region for b_0 becomes

$$|\boldsymbol{\eta}| \leq 2.$$

Therefore, grating-lobes and sidelobes of $b_0(\boldsymbol{\eta})$ are to be considered within these regions. Figure 4.2 shows the visible region in $\boldsymbol{\eta}$ -space. The smaller solid circle ($R = 1$) shows the horizon where the main beam is aimed at the zenith.

4.3 Evaluation Function

The objective of this study is to design an array which does not have undesirably large sidelobes including grating-lobes, in a region of beam space discussed in the previous section. This region is subject to applications for which the array is employed, and we hereafter refer to it as D . To evaluate the goodness of an array, we introduce a mean-square function in the region D in $\boldsymbol{\eta}$ -space. Note that this criterion will also result in minimizing the average power of incident noise from the region D . Thus the evaluation function is defined by

$$E = \frac{1}{S} \int_D |b_0(\boldsymbol{\eta})|^2 d\boldsymbol{\eta}, \quad (4.9)$$

where S is the area of D . Using a weight function $\Psi(\boldsymbol{\eta})$, the evaluation function is redefined as,

$$E = \frac{\int |\Psi(\boldsymbol{\eta})b_0(\boldsymbol{\eta})|^2 d\boldsymbol{\eta}}{\int |\Psi(\boldsymbol{\eta})|^2 d\boldsymbol{\eta}}, \quad (4.10)$$

where

$$\Psi(\boldsymbol{\eta}) = \begin{cases} 1 & (\boldsymbol{\eta} \in D) \\ 0 & \text{otherwise} \end{cases}. \quad (4.11)$$

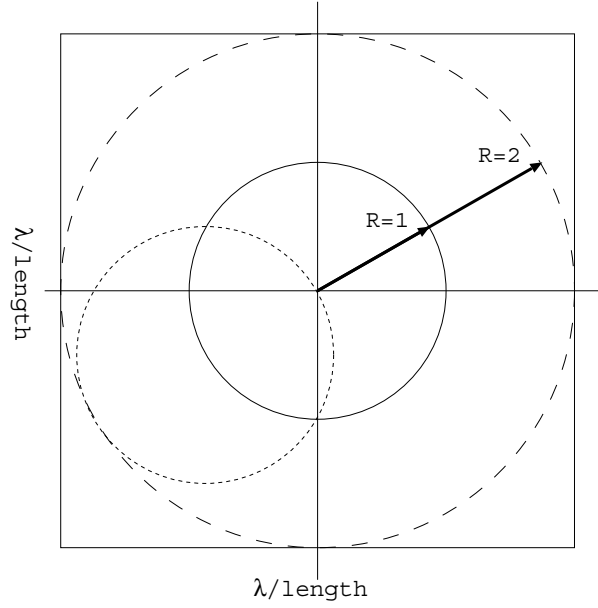


Figure 4.2: The visible region in $b_0(\boldsymbol{\eta})$ in $\boldsymbol{\eta}$ -space. The origin means the direction of the main beam. The solid circle corresponds to the horizon along the plane in which the array is placed when the main beam is assumed to be steered toward the zenith. The smaller dashed circle is the horizon appears when the mainlobe is horizontally tilted. The inside of the larger dashed circle thus corresponds to the entire visible area when all the possible mainlobe directions are allowed.

In this study, we set the region

$$D : R_1 \leq |\boldsymbol{\eta}| \leq R_0.$$

R_1 corresponds to the mainlobe region and R_0 corresponds to the entire visible region. We thus obtain a donut shaped weight function $\Psi(\boldsymbol{\eta})$, which has a cavity with a radius of R_1 for mainlobe, as shown in Fig.4.3.

4.4 An Optimization Algorithm in Beam Space

First, we introduce a simple trial-and-error array optimization algorithm using the evaluation function discussed in previous section. This algorithm mainly consists of random perturbation and evaluation for update.

This algorithm mainly consists of random perturbation and evaluation for update. At each iteration, first, the algorithm suggests a temporary position \mathbf{X} such that $\mathbf{X} = \mathbf{X}^{(\text{prev})} + \Delta\mathbf{X}$ where $\mathbf{X}^{(\text{prev})}$ is the antenna position at the previous iteration and $\Delta\mathbf{X}$

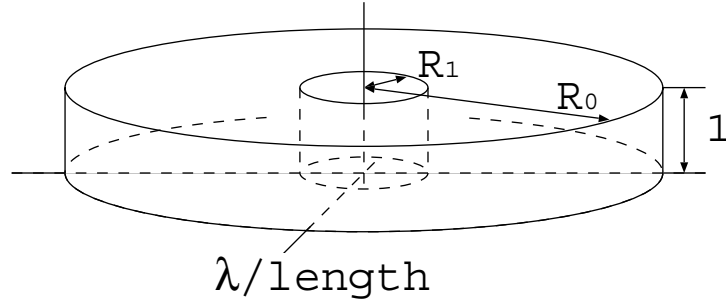


Figure 4.3: Weight function $\Psi(\boldsymbol{\eta})$. R_0 and R_1 should be set to the size of visible region and mainlobe region, respectively.

is a small random perturbation. Second, the temporary position $\mathbf{X}^{(\text{temp})}$ is set to the result of i th step as $\mathbf{X}^{(i)}$ if the evaluation is better than that of $(i - 1)$ -th step or stay at the same position otherwise. In these processes, the standard deviation of $\Delta\mathbf{X}$ is diminished if no update is made during a couple of iterations. For a better convergence, random perturbations and evaluations are made step by step for each antenna in a real implementation. This process repeats until the evaluation E is minimized.

Each step of this algorithm is listed as follows:

Initialization part:

- 1 Set the initial position $\mathbf{X}^{(0)} = \mathbf{0}$.
- 2 Calculate its mean-square evaluation $E^{(0)}$.

Iteration part: (for n th antenna in i th iteration)

- 1 Impose random perturbation $\Delta\mathbf{x}_n$ on top of the previous position such that $\mathbf{x}_n^{(\text{temp})} = \mathbf{x}_n^{(i-1)} + \Delta\mathbf{x}_n$.
- 2 Calculate Fourier transform to obtain $b_0(\boldsymbol{\eta})$.
- 3 Calculate square integration;

$$E^{(\text{temp})} = \int |\Psi(\boldsymbol{\eta})b_0(\boldsymbol{\eta})|^2 d\boldsymbol{\eta}$$

- 4 Set or unset the antenna position according to $E^{(\text{temp})}$.

$$\begin{cases} \mathbf{x}_n^{(i)} \leftarrow \mathbf{x}_n^{(\text{temp})} & (\text{when } E^{(\text{temp})} < E^{(\text{prev})}) \\ \mathbf{x}_n^{(i)} \leftarrow \mathbf{x}_n^{(i-1)} & (\text{when } E^{(\text{temp})} \geq E^{(\text{prev})}) \end{cases}$$

Figure 4.4 shows a flow chart of this algorithm.

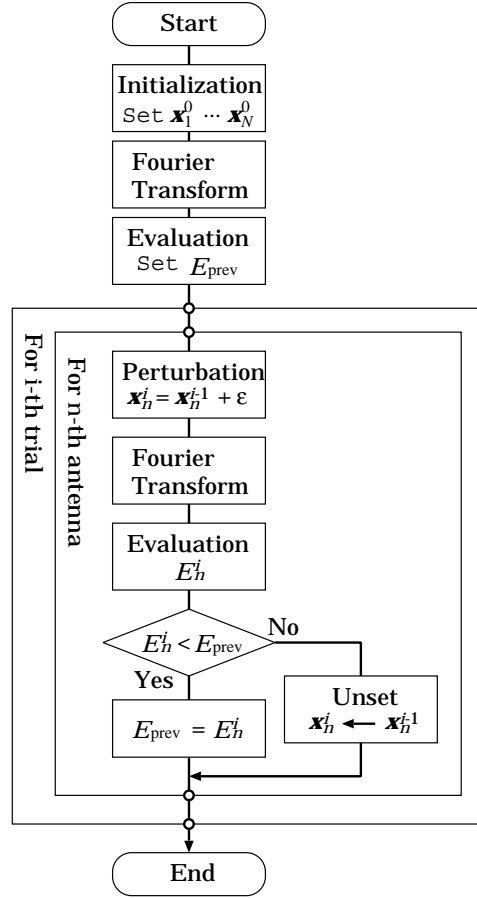


Figure 4.4: Flow chart of the optimization algorithm with beam-space evaluation.

4.5 Fast Evaluation Algorithm based on Potential Function

To evaluate a given array using the evaluation function given by eq.(4.10), numerical Fourier Transform and a numerical integration are required at each time. This time-consuming procedure is not preferable for an array optimization which utilizes an iterative scheme. In this section, we develop a fast optimization algorithm that does not require Fourier transform and numerical integrations.

The mean-square function for the sidelobe region introduced in previous sections re-states

$$E = \int |\Psi(\boldsymbol{\eta})b_0(\boldsymbol{\eta})|^2 d\boldsymbol{\eta}. \quad (4.12)$$

According to Parseval's theorem, squared integration in eq.(4.12) is a preserved quantity

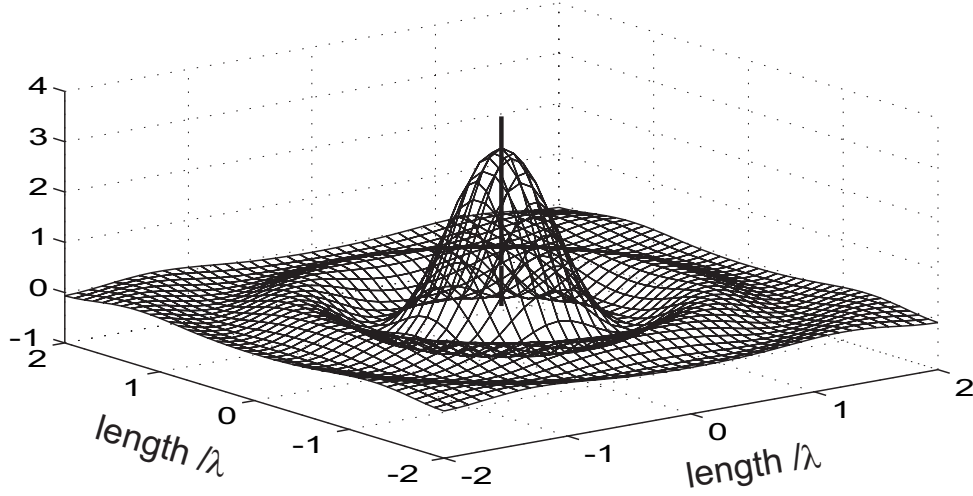


Figure 4.5: A potential function $\psi(\mathbf{x})$ in \mathbf{x} -space as a Fourier transform of $\Psi(\boldsymbol{\eta})$ corresponding to $R_0 = 1$.

for Fourier transform and is written as a function in \mathbf{x} -space using convolution $*$ as,

$$E(\mathbf{X}) = \int |(\psi * a_0)(\mathbf{x})|^2 d\mathbf{x} \quad (4.13)$$

$$= \int \left| \sum_{m=1}^N \psi(\mathbf{x} - \mathbf{x}_m) \right|^2 d\mathbf{x} \quad (4.14)$$

where $\psi(\mathbf{x})$ is the 2D Fourier Transform of $\Psi(\boldsymbol{\eta})$:

$$\psi(\mathbf{x}) = \frac{R_0 J_1(2\pi R_0 |\mathbf{x}|)}{|\mathbf{x}|} - \frac{R_1 J_1(2\pi R_1 |\mathbf{x}|)}{|\mathbf{x}|} \quad (4.15)$$

where J_1 is Bessel's function of the 1st order. Eq.(4.15) rules the relative displacement among antennas therefore this function is hereafter called *potential function*. The equivalence of evaluations in antenna space and beam space is illustrated in Fig.4.6.

This $\psi(\mathbf{x})$ is a two-dimensional real function and is an angular-independent function

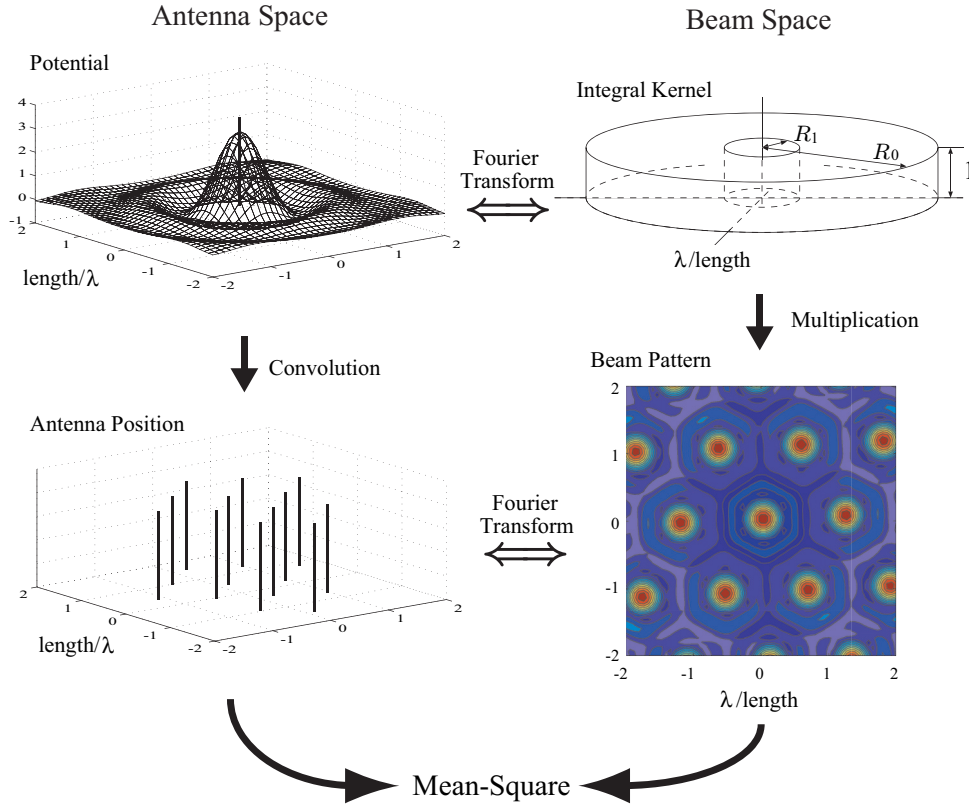


Figure 4.6: The equivalence in antenna space and beam space is illustrated. According to Parseval's theorem, the squared integration of the total potential field, which is a convolution of the potential function and a antenna function, is guaranteed to be equivalent to the squared integration of a beam function multiplied with the kernel function.

around the origin. Therefore, the evaluation function calculated at each iteration holds

$$E(\mathbf{X}) = \int \left[\sum_{m=1}^N \psi(\mathbf{x} - \mathbf{x}_m) \right]^2 d\mathbf{x} \quad (4.16)$$

$$\begin{aligned} &= \sum_{n,m=1}^N \int \psi(\mathbf{x} - \mathbf{x}_n) \psi(\mathbf{x} - \mathbf{x}_m) d\mathbf{x} \\ &= \sum_{n,m=1}^N \int \psi(\mathbf{x}) \psi(\mathbf{x} + \mathbf{x}_n - \mathbf{x}_m) d\mathbf{x}. \end{aligned} \quad (4.17)$$

The integration in eq.(4.17) can be considered as the auto-correlation function of a real function $\psi(\mathbf{x})$. An auto-correlation of a function and squared absolute of its Fourier

transform are a Fourier transform pair as

$$\int \psi(\mathbf{x})\psi(\mathbf{x} + \mathbf{x}_n - \mathbf{x}_m)d\mathbf{x} \stackrel{\mathcal{F}}{\Leftrightarrow} |\Psi(\boldsymbol{\eta})|^2 \quad (4.18)$$

Since the function $\Psi(\boldsymbol{\eta})$ is defined by eq.(4.11), the squared absolute is

$$|\Psi(\boldsymbol{\eta})|^2 = \Psi(\boldsymbol{\eta}). \quad (4.19)$$

We can thus conclude

$$\int \psi(\mathbf{x})\psi(\mathbf{x} + \mathbf{x}_n - \mathbf{x}_m)d\mathbf{x} = \psi(\mathbf{x}_n - \mathbf{x}_m). \quad (4.20)$$

The evaluation function eq.(4.17) is now restated as

$$E(\mathbf{X}) = \sum_{n,m=1}^N \psi(\mathbf{x}_n - \mathbf{x}_m). \quad (4.21)$$

This evaluation function has neither numerical Fourier transform nor integration and can be calculated much faster than the original expression while it provides an identical result. The equation indicates that the mean-square sidelobe can be evaluated by the total potential formed by all the antennas. Therefore the minimization is simply made by moving every antenna in turn to where the total potential is lower.

4.6 Resulting Arrays by the Trial-end-Error Algorithm

Since this algorithm is based on probabilistic method, resulting arrays are differently formed from a trial to another. Figure 4.7 shows the array that is most frequently generated as a result of the trial-and-error algorithm discussed above. While this type of array has the lowest average sidelobe level, however, it has grating-lobes caused by the uniformly spaced antennas. Therefore, this array can not be adopted for the purpose of making a gratinglobe-free adaptive antenna. Figure 4.8 shows some other resulting arrays on the same condition and Fig. 4.9 is a scattering diagram of peak sidelobe vs mean-square sidelobe for 10000 arrays. Because of large degrees of freedom, some arrays have asymmetric appearance despite its low peak sidelobe level.

In order to obtain a symmetric array that has satisfactory properties in terms of sidelobe, we tried the algorithm under some constrained conditions. Figure 4.10 shows the resulting arrays for 12 antennas generated under the condition of 3-fold (120 degrees) rotational symmetry. Under this condition, the most frequent result is also the triangular array that has the same appearance shown in Fig. 4.7. Nevertheless the most frequent

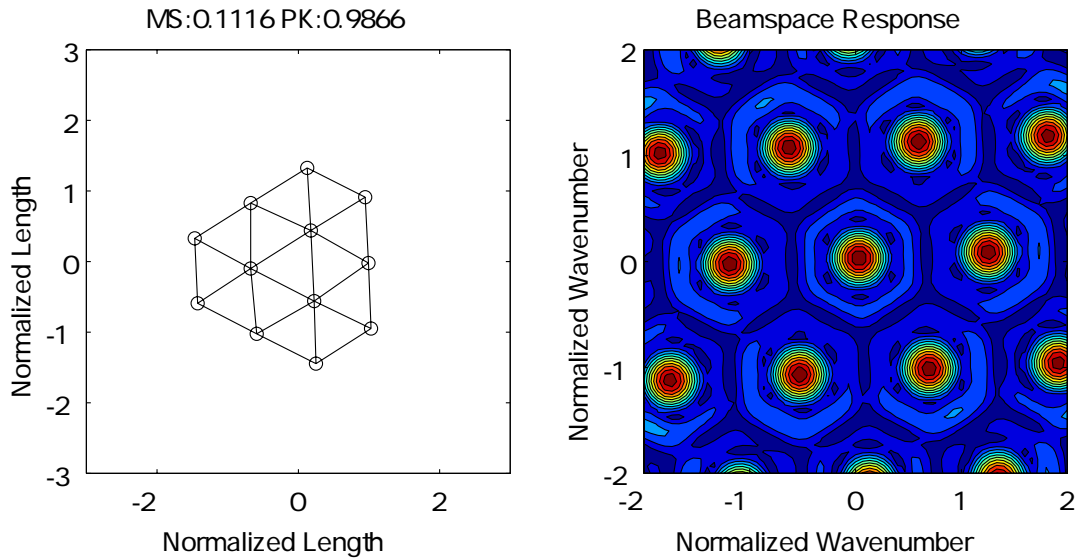


Figure 4.7: A resulting array that the most usually appears as 12-element array with the trial-and-error algorithm. This type of array has grating-lobes because of uniform spacing. In each figure, "DMIN" indicates minimum distance of antennas, "MS" and "PK" indicate mean-square sidelobe within the radius $R \leq 1$ except for the mainlobe region $R \leq 0.1$ and the peak sidelobe level (in power ratio to the main-lobe) within $0.2 < R < 2$.

result is unchanged, one type of resulting array shown in Fig. 4.10 which is not included in the result under no constraint exhibits preferable performance.

Figure 4.11 is the scattering diagram of the peak and mean-square sidelobe response of each result. Points for triangular arrays are distributed around the top-left corner of the scattering diagram. In this diagram, the bottom-left corner is the best in terms of both of peak and mean-square evaluations. The edge at the bottom-left of the distribution is formed by the points which have an appearance such as in the bottom panel in Fig.4.10.

Figure 4.12 shows a scattering diagram for peak sidelobe and the distance of most closely neighboring antennas in the array. Basically, in this region, larger antenna-distance yeilds larger peaks. The triangular-rectangular shaped array shown above has also the best performance in terms of minimum distance.

Computation time with this method is approximately 1000 times as fast as the previous method that utilizes Fourier transform and integrations; 10 ms to 10 s on a PC (a Pentium D processor in it). This fact supports applications to a larger array optimization.

We tried a larger array consisting of 36 elements as a case study under the condition of 3-fold symmetry. Figure 4.13 shows a typical resulting array. It is worth noting that the 12 elements at the center forms almost the same as the array in Fig. 4.10.

In this section, we only made a case study for 12- and 36-element arrays with the

fast method. A larger array optimization that has more than 100 elements is also of our interest for a high-gain radar applications, for example.

4.7 Optimization by the Steepest Descent Method

We saw that the mean-square sidelobe evaluation can be calculated by the total potential formed by all the antennas. Then, we can also minimize the evaluation function only by moving each antenna repetitively so that it would be located at the bottom of the total potential. This is simply achieved by the steepest descent method, for example.

Based on the discussion made in the previous section, the steepest descent method can be given as

$$\underset{\mathbf{X}}{\text{minimize}}[E(\mathbf{X})] : \quad \mathbf{X}^{(n+1)} \leftarrow \mathbf{X}^{(n)} - \alpha \nabla E(\mathbf{X}^{(n)})$$

where $\nabla E(\mathbf{X})$ is a $2N$ -dimensional gradient vector

$$\begin{aligned} \nabla E(\mathbf{X}) &= \left(\frac{\partial}{\partial \mathbf{x}_1} E(\mathbf{X}), \frac{\partial}{\partial \mathbf{x}_2} E(\mathbf{X}), \dots, \frac{\partial}{\partial \mathbf{x}_N} E(\mathbf{X}) \right) \\ &= 2 \left(\frac{\partial}{\partial \mathbf{x}_1} \bar{\psi}(\mathbf{x}_1), \frac{\partial}{\partial \mathbf{x}_2} \bar{\psi}(\mathbf{x}_2), \dots, \frac{\partial}{\partial \mathbf{x}_N} \bar{\psi}(\mathbf{x}_N) \right) \end{aligned}$$

where $\bar{\psi}(\mathbf{x}_n)$ means total potential formed all the antennas except for the n th antenna itself:

$$\bar{\psi}(\mathbf{x}_n) = \sum_{\substack{m=1 \\ m \neq n}}^N \psi(\mathbf{x}_n - \mathbf{x}_m). \quad (4.22)$$

This is not a probabilistic method and yields a particular result depending on the initial state. In most cases, this method results in a uniformly spaced triangular array, which is not preferable for our purpose. We therefore introduce another constraint to restrict the minimum distance between an antenna to others. This constraint is realized as a barrier potential that has a cylindrical shape to increase the evaluation function when an adjacent antenna enters it.

A case study is made for 12-element array based on the potential function corresponding to the kernel function with $R_0 = 1.5$ and $R_1 = 0.15$ that results in a triangular array of an interval of $2/3\lambda$. Figure 4.15 (left) shows a result made without the barrier potentials. We employ a barrier potential given by

$$\phi(\mathbf{x}) = A / (1 + \exp(B * (|\mathbf{x}| - C))).$$

In addition to the barrier potential, we introduce another constraint potential fixed to the \mathbf{x} -space $\varphi(\mathbf{x}) = D|\mathbf{x}|^2$ for the antennas not to be too widely distributed. Thus we obtained a modified potential function in replace to eq.(4.22),

$$\bar{\psi}(\mathbf{x}_n) = \sum_{\substack{m=1 \\ m \neq n}}^N [\psi(\mathbf{x}_n - \mathbf{x}_m) + \phi(\mathbf{x}_n - \mathbf{x}_m)] + \varphi(\mathbf{x}_n) \quad (4.23)$$

Parameters A, B, C and D are set to empirical values 3, 20, 0.8 and 1, respectively. A resulting array shown Fig.4.15 (right) has no grating-lobes and the maximum sidelobe response of less than 0.5 in power.

4.8 Summary

A novel method to design an optimum arrangement for adaptive antenna array was presented. We first introduced a trial-and-error algorithm employing a mean-square evaluation of the sidelobe level in beam space. This algorithm was very simple and has intuitive nature. However, the algorithm requires two-dimensional numerical Fourier transform and squared integration that consumes time. We therefore introduced a mathematical interpretation of this method using the concept of potential that is defined by the Fourier transform of integral kernel for mean-square evaluation. Under the condition that the kernel is a binary function, mean-square evaluation of total potential can be calculated without integration and it result in reducing computation time by a great amount.

Since the algorithm is based on probabilistic procedures, resulting arrays differ from a trial to another. Some of these array have preferable properties regarding the peak sidelobe. Case studied were made for 12- and 36-element arrays. For 12-element case, a triangular-rectangular-combined array that has low peak/average sidelobe and sufficient clearance between each antenna appears as a typical result. In an experiment for 36-element array, a similar array exhibits remarkable performance in this respect. Approximately 1000 times as fast as the method with Fourier transform and integrations, the proposed method is needed for a larger array applications.

In the last section, the steepest descent method is employed for the minimization problem. Since this method is no longer probabilistic, resulting arrays are uniformly spaced in a triangular form, which is not preferable for adaptive array. We thus utilized potential barrier that limit the distance between an antenna and another with a potential corresponding to a kernel that encompasses wider sidelobe region. A resulting array has a shape that is almost the same as that made with probabilistic method.

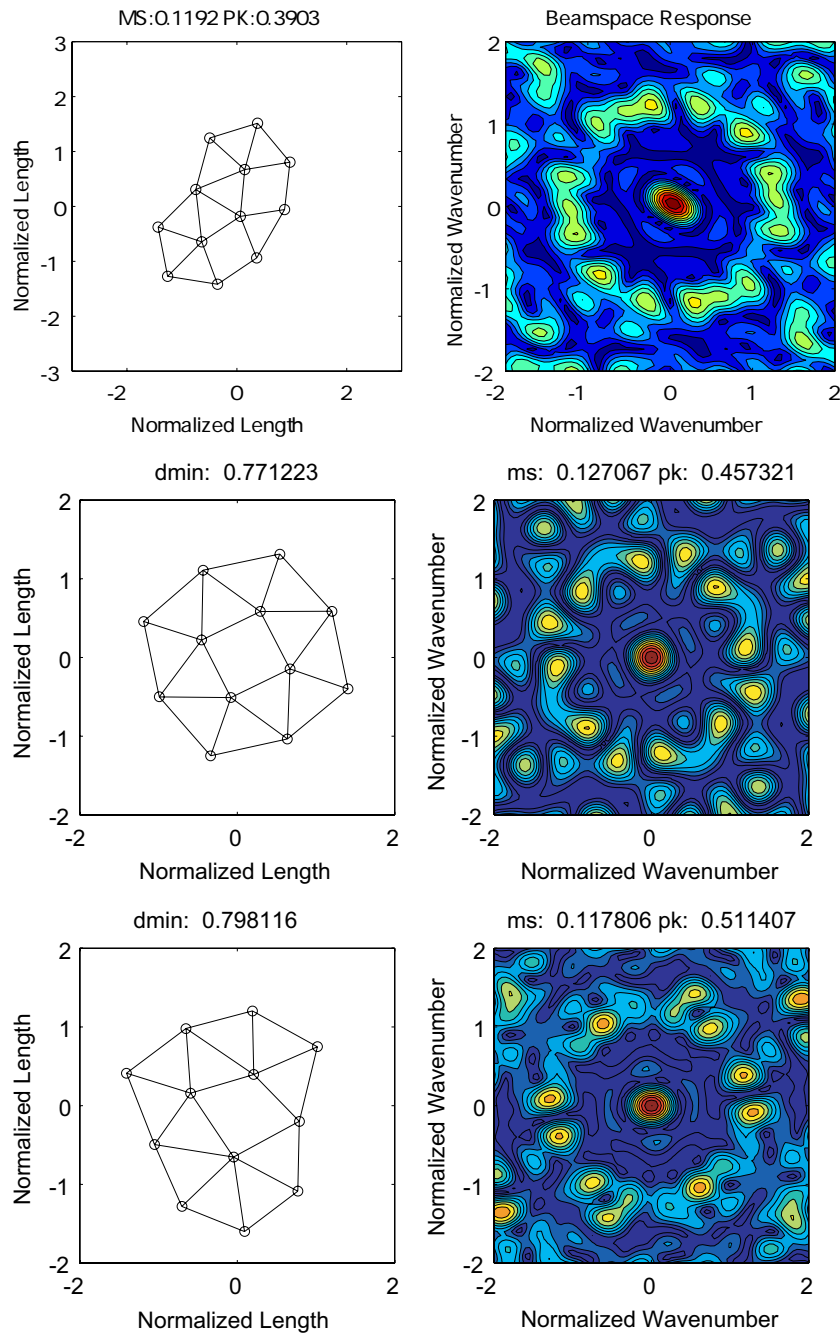


Figure 4.8: Resulting arrays generated by the try-and-error algorithm. The performance of each array is evaluated by mean-square sidelobe response and the peak sidelobe response which are noted on top of its left panel. Top panels show a triangular array that has the minimum mean-square sidelobe response and appears most frequently as a result.

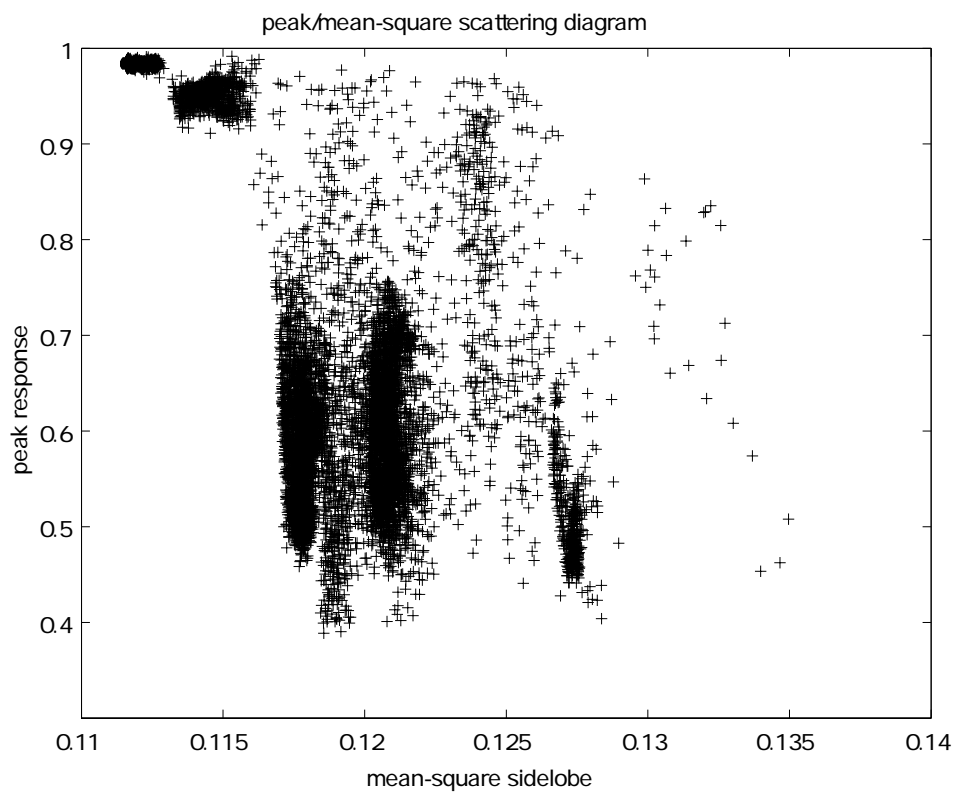


Figure 4.9: The scattering diagram for the peaks vs. mean-square sidelobe responses of 10,000 arrays generated by the iteration algorithm.

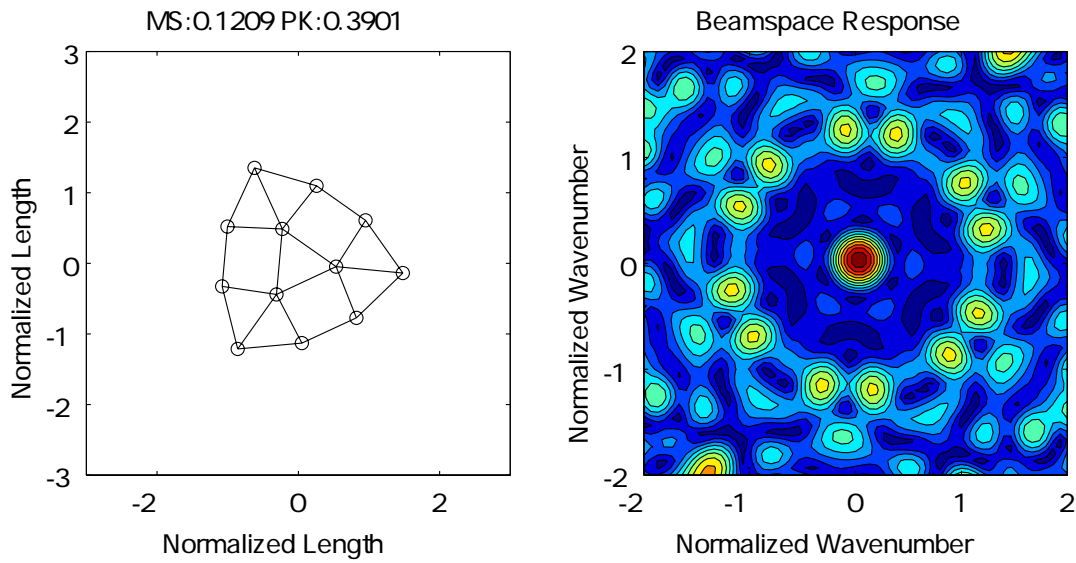


Figure 4.10: Resulting arrays generated by the same algorithm in Fig.4.8 but under the constraint of 3-fold (120 degrees) rotational symmetry.

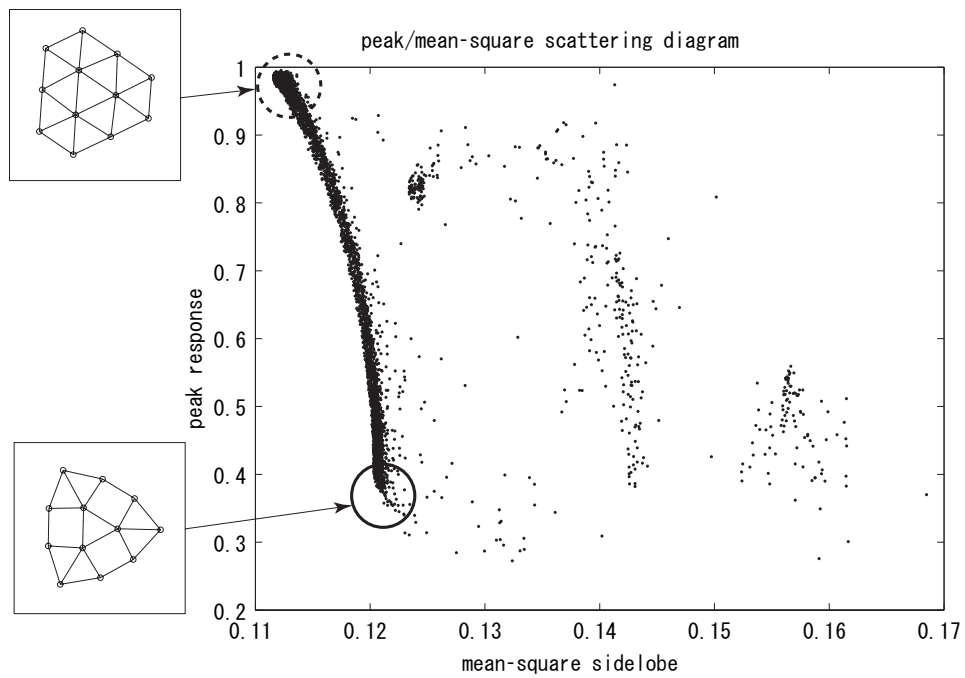


Figure 4.11: The scattering diagram for the peaks vs. mean-square sidelobe responses of 10,000 arrays generated by the iteration algorithm.

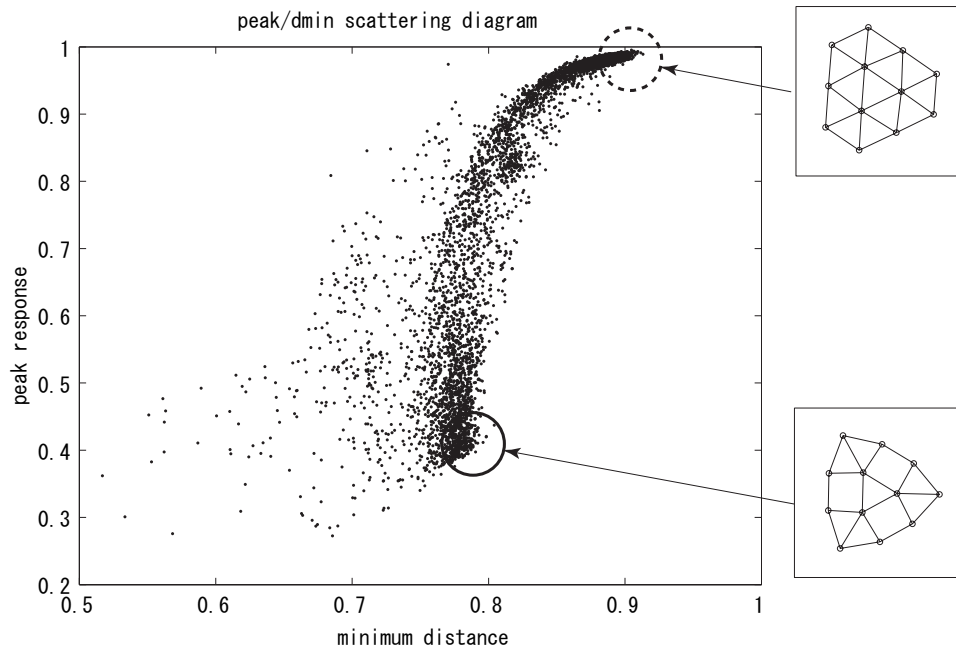


Figure 4.12: The scattering diagram for the peaks vs. minimum distance of adjacent antennas in the array. The data is the same as for Fig.4.11. The corner at the right-bottom is the best.

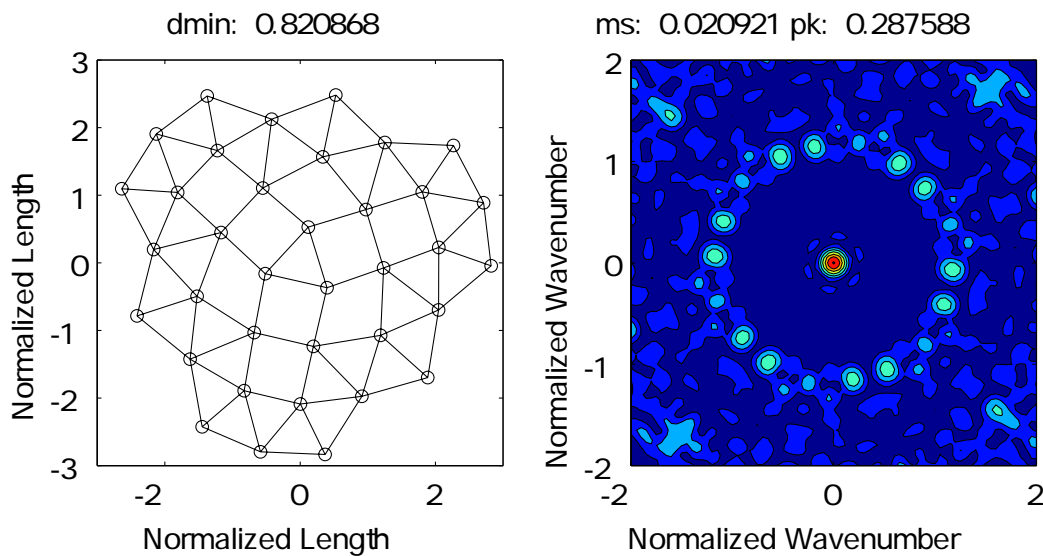


Figure 4.13: An example of 12-element array generated under the condition of 3-fold symmetry. This type of array has remarkably low sidelobe response.

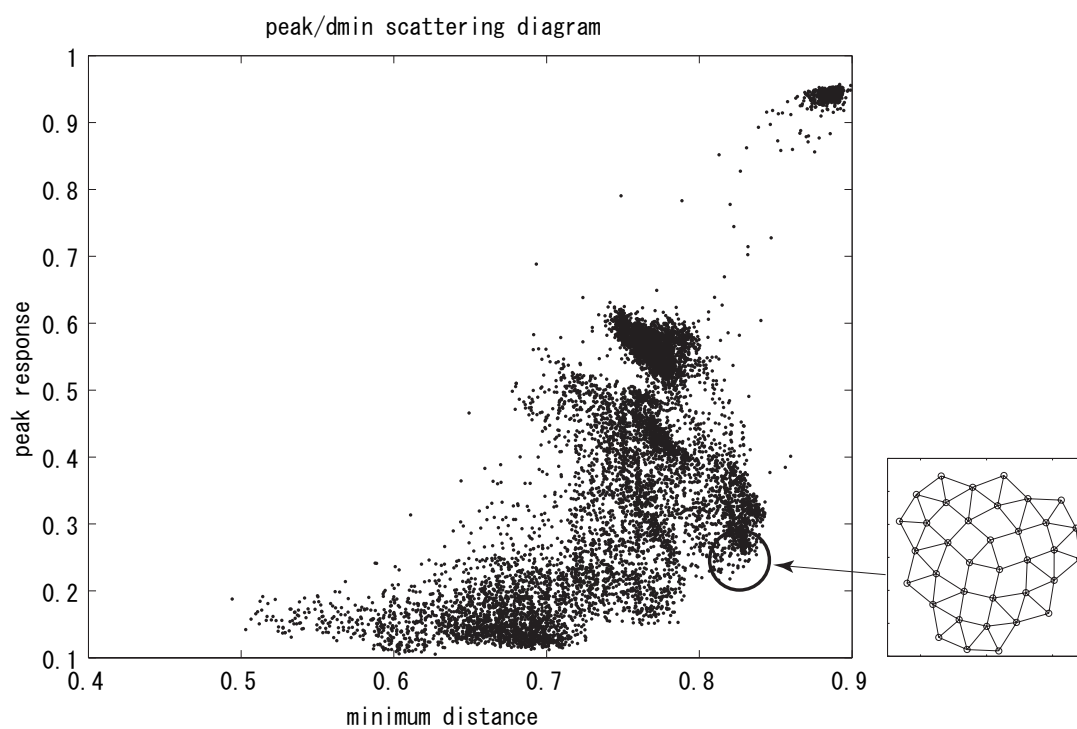


Figure 4.14: A scattering diagram of peak-sidelobe vs minimum distance between antennas. The array of Fig. 4.13 is located at around the right bottom corner.

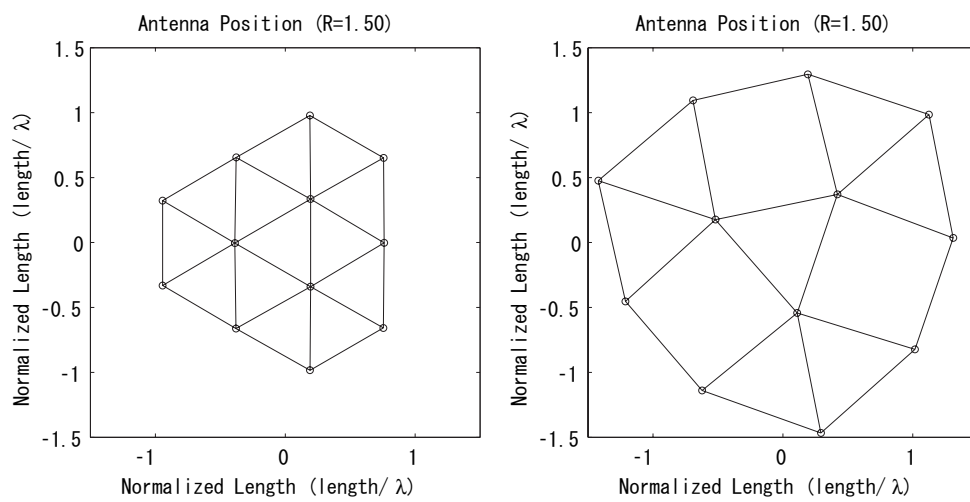


Figure 4.15: Antenna displacement ($N = 12$) generated by proposed algorithms. Circles indicate antenna positions. Lines which link two adjacent antennas closer than 1λ are put for visibility. Left and right panel show the case $R_0 = 1.5$ without and with potential barriers, respectively.

Chapter 5

Multistatic Observation of the Atmosphere

5.1 Settings of Receiver Arrays

The signal of atmospheric echo is a stochastic process whose power spectrum is well approximated by a Gaussian distribution function with a standard deviation of σ_r , and a fluctuation proportional to its power spectral density. In a real analysis, an incoherent integration or a smoothing of the spectra must be done to obtain an accurate estimate of the Doppler shift.

Estimation error of the radial Doppler velocity, measured with each receiver array, is described by spectral resolution δ_f , spectral width of the signal σ_r and the number of incoherent integration N as follows:

$$E = k\sqrt{\frac{\lambda\sigma_r\delta_f}{2N}} \quad (5.1)$$

where λ is the wave length of the radio that is 6.38 m and k is a constant characteristic of an estimation method. According to Yamamoto et al. (1988), the constant k is 0.38 and 0.63 for the moment and the fitting methods, respectively.

In this study, to determine the radial velocity, we used a fitting of a parabolic function in a log-scale spectrum and also manual corrections in some part. Therefore, it is rather unclear which k is best to chose. Erring on the side of safety, we chose the larger constant of 0.63 to represent k for our entire fitting process. In our data processing process, we divide a single period of 81.6 sec into 8 of 10.2 sec periods which corresponds to δ_f of 0.098 Hz and N of 8. Substituting $\lambda = 6.38$ m, $N = 8$, $\delta_f = 0.098$ Hz, and $\sigma_r = 0.7$ m/s which is typical for tropospheric observations, into eq.(5.1), $E=0.104$ m/s.

In a multistatic system, the estimation error of 3D wind velocity is evaluated by substituting normal stochastic variables n_i , with a standard deviation of E , into v_i of eq. (2.16). For examining the location of receivers, we first evaluate the estimation error

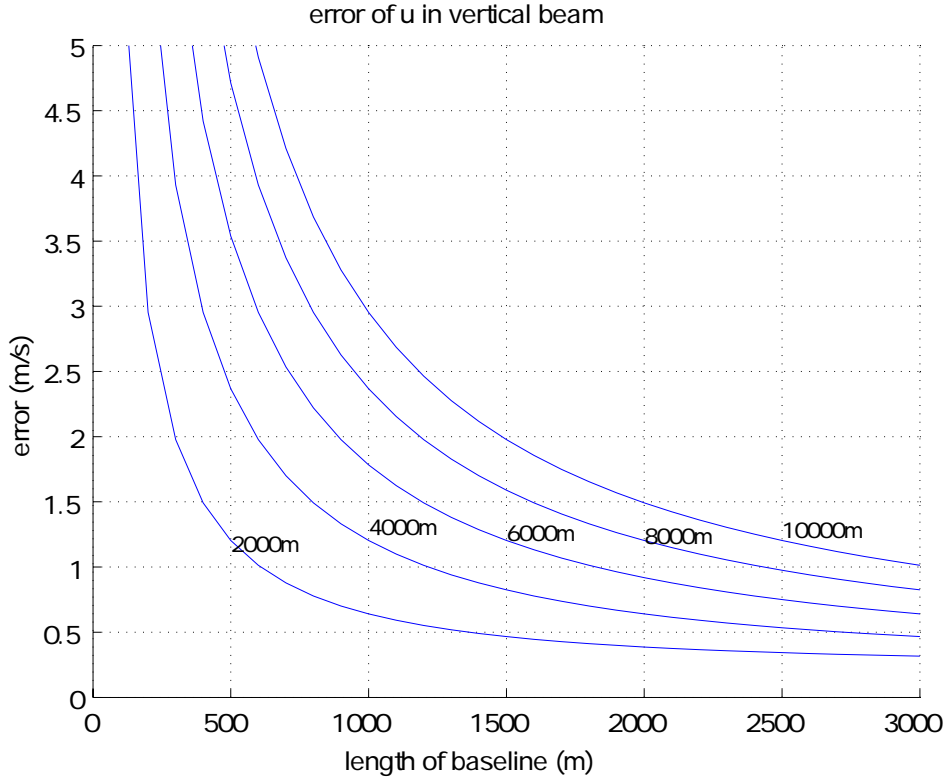


Figure 5.1: Estimation error of the horizontal wind velocity in a vertical beam versus the length of the baseline.

of 2D wind velocity in a bistatic system model. For observation with a vertical beam from the radar, the estimation error of the vertical component is given by

$$\langle (w - \tilde{w})^2 \rangle = E^2, \quad (5.2)$$

where \tilde{w} is an estimate of the vertical component w , and that of horizontal component u is expressed as

$$\langle (u - \tilde{u})^2 \rangle = \frac{1}{b^2} (6h^2 + 2h\sqrt{h^2 + b^2} + 5b^2) E^2, \quad (5.3)$$

where \tilde{u} is an estimate of u , h is the altitude of the target volume, and b is the length of the base line between the radar and the receiver, respectively.

Baselines affect the estimation accuracy of 3D wind velocity; a longer length effectively provides a higher accuracy as shown in Fig. 5.1. However, we have a height ceiling for sensitivity that depends on the number of antennas. The profile of signal-to-noise ratio (SNR) measured by the EAR, which is equivalent to a receiver consisting of 560 antennas,

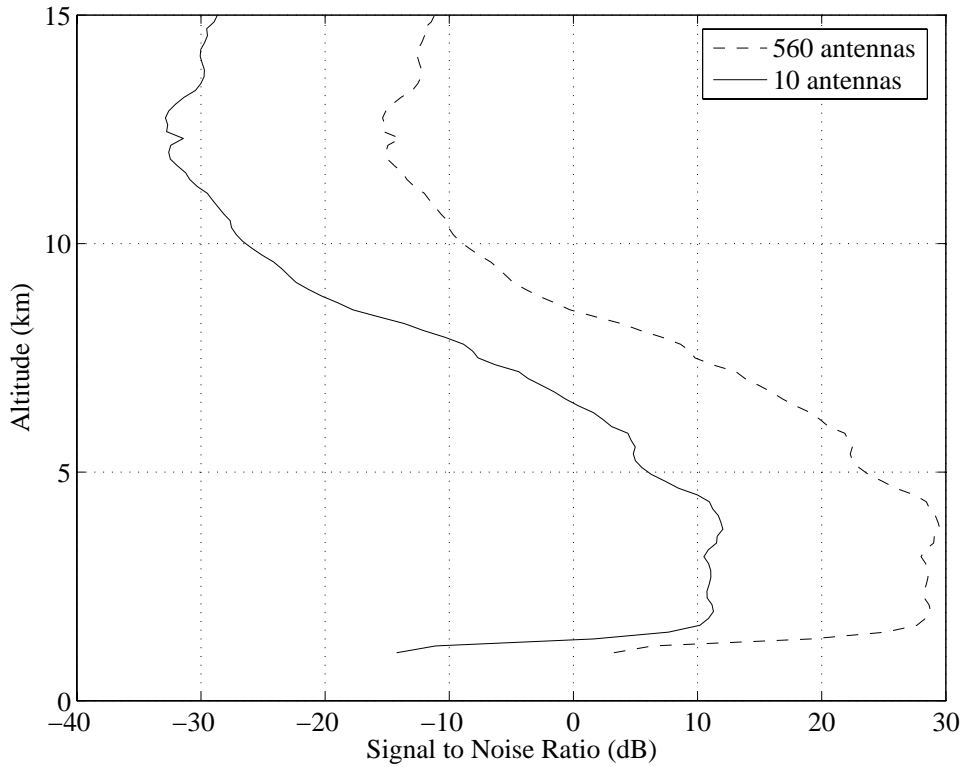


Figure 5.2: Signal-to-noise ratio profile measured by the EAR in a monostatic observation using Spano code (dashed). The solid line shows an SNR which is shifted by -17.5dB ($=10 \log_{10}(560/10)$) from the dashed line assuming 10 antennas are used in a receiver site.

is shown in Fig.5.2. In this observation, each multistatic receiver consists of 10 antennas; Therefore, the SNR profile is shifted -17.5dB ($=10/560$) from that in Fig.5.2. Since the detection limit of atmospheric echo is around -15dB in SNR, the height ceiling for sensitivity reaches 8 km.

Considering the accuracy effect and the height ceiling for sensitivity, we chose two suitable places that are approximately 1300 m away to the west and the south of the EAR, respectively. Within the lower than 8 km altitude limit for sensitivity, these two positions give an estimation error of better than 2 m/s for the horizontal wind components. The relative position of the two places to the EAR is $(-1278, -6, -57)$ and $(306, -1296, 15)$, respectively, in (x, y, z) coordinates (in meters). Hereafter, these two sites for the receiver arrays (see Figure 5.3) are referred to as Site-A (west) and Site-B (south).

Each of the receiver sites consists of 10 antennas that are aligned roughly in a triangular form with an interval of 0.7λ ($\approx 4.5\text{m}$) that theoretically has optimal sidelobe suppression. (Fig. 5.4)

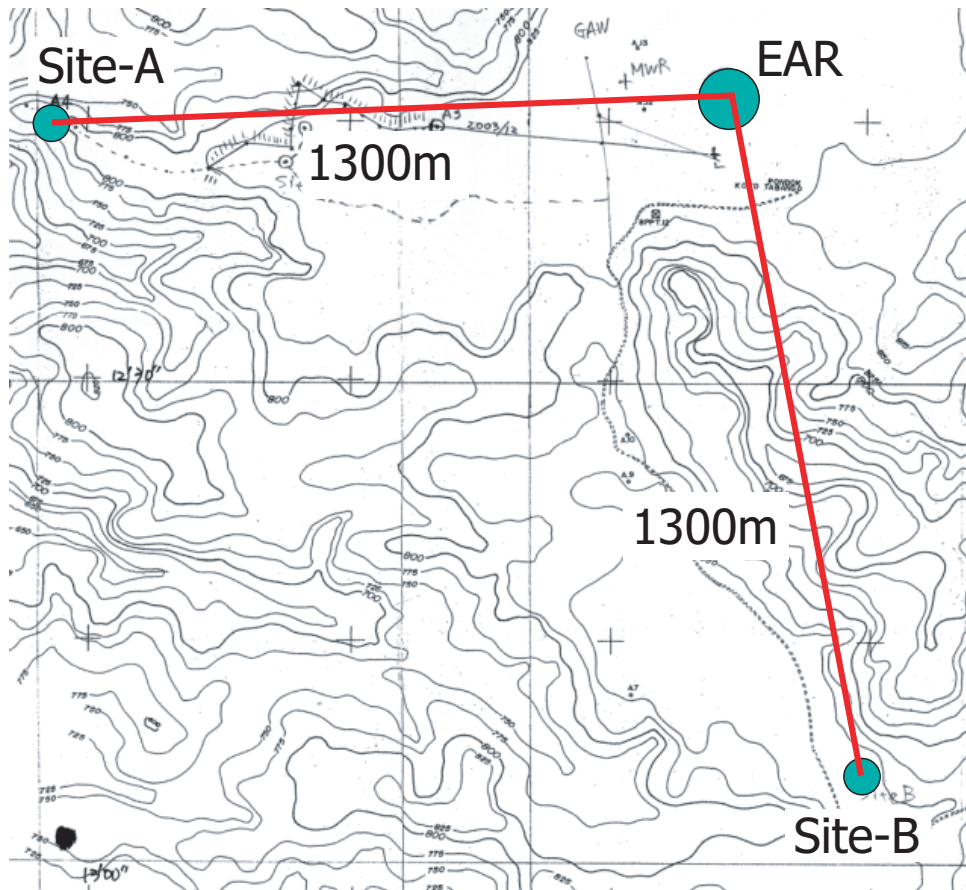


Figure 5.3: A plan view of the EAR, site-A and B.

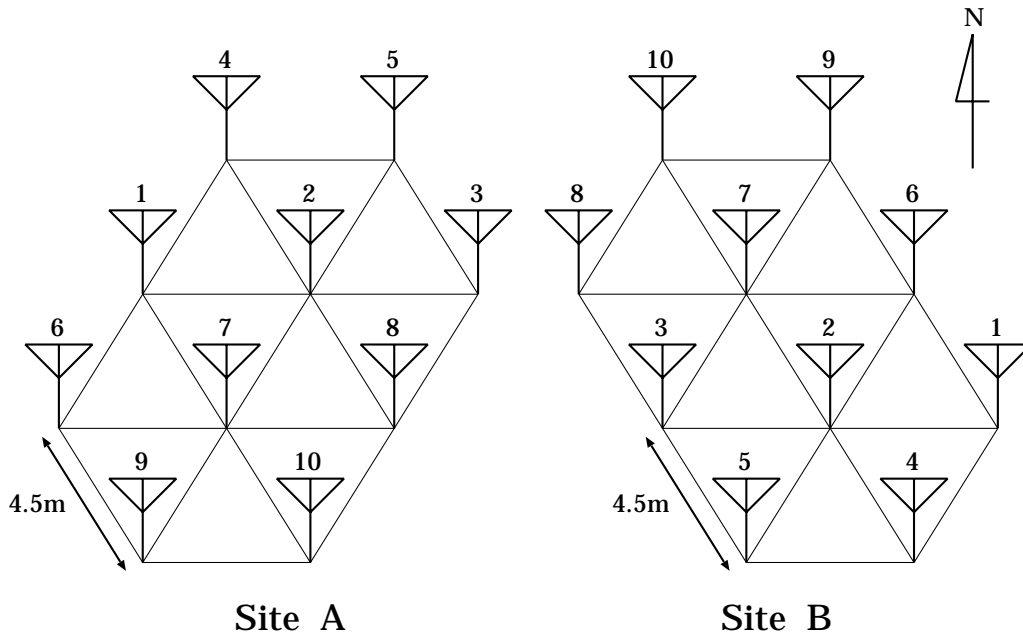


Figure 5.4: Arrangement of the antenna at Site-A and Site-B.

5.2 Design of Digital Receivers

A digital receiver, which generally means one that has a numerical mixer, has remarkable advantages over an analog receiver. The largest advantage is the capability of balanced I/Q demodulation that is required for coherent radar applications. Inevitably, in an analog receiver, the I/Q demodulation suffers an imbalance output caused by incomplete adjustment of two channel gains or phases. In a digital receiver, on the other hand, this imbalance does not occur due to numerical process of the I/Q demodulation.

In general, however, digital receiver systems with a fully adaptive capability for radar are quite expensive. For our observations, we developed a highly cost-effective digital receiver system consisting of a PC and ready-made digital receiver PCI boards (Echotek ECDR-214PCI) with onboard A/D converters and digital down-converters. Figure 5.5 is a schematic diagram of the system. The PCI board has two analog inputs intended for IF signals, A/D converters and 4 independent signal processing units. Hence each board is used as two receiver systems with I/Q channels. Each receiver system consists of an antenna, a band-pass filter with a band width of 10 MHz and a low noise amplifier with a gain of approximately 25 dB, followed by the board.

The sampling clock is generated by a GPS receiver system with a reference clock output of 10 MHz followed by a digital direct synthesizer (DDS) that up-converts the clock signal to 64 MHz. The 47 MHz RF signal received by the antenna is directly

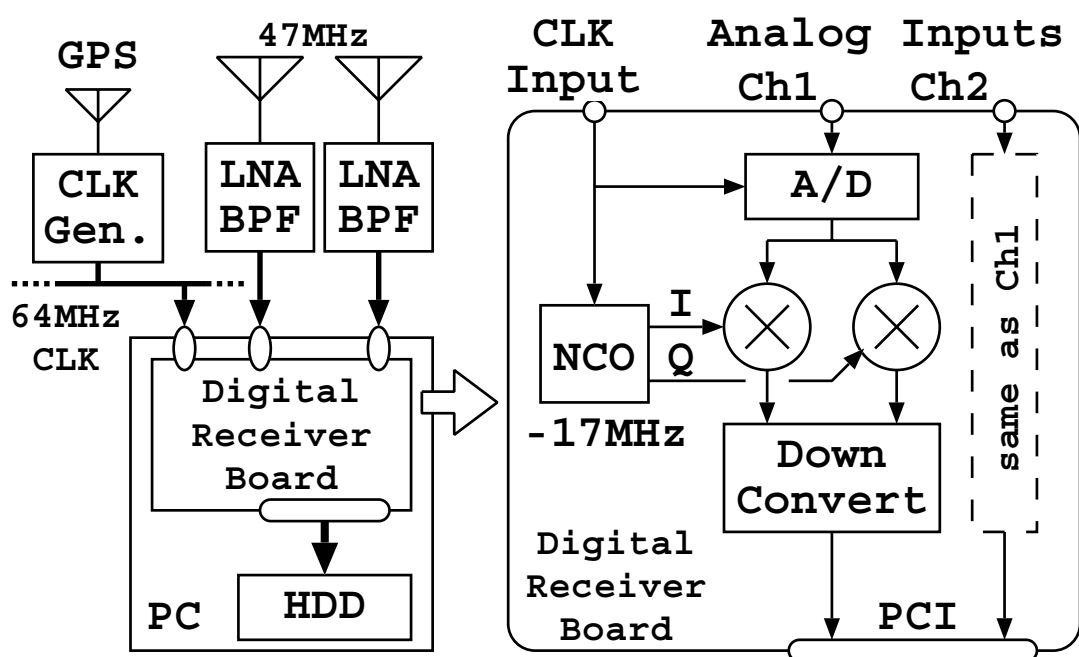


Figure 5.5: Schematic diagram of a digital receiver board and the entire digital receiver system.

sampled and quantized by the A/D converter on-board at this clock frequency with a resolution of 14 bits. It should be noted that the RF frequency of 47 MHz corresponds to the second half of the Nyquist frequency range from 32 to 64 MHz.

The Dynamic range of the A/D converter must widely cover the level from the galactic noise to ground clutter. At the frequency of 47 MHz, which is used by the EAR, the largest noise source is galactic radiation that has an average temperature T_g roughly represented by 7500 K. The power of galactic noise is given by

$$P = k_B T_g B \quad (5.4)$$

$$= 1.05 \times 10^{-9} \text{ mW} , \quad (5.5)$$

where k_B is the Boltzmann constant and B is the bandwidth of the receiver. The bandwidth of the band-pass filter is set to 10 MHz in order to keep the galactic noise sufficient for dithering. Maximum transmission loss caused by cables and connectors is estimated to be 3 dB; Therefore, galactic noise at the output of antenna is approximately -93 dBm where 0 dBm is equal to 1 mW. The digital receiver has analog-to-digital (A/D) converters with resolution of 14 bits, which corresponds to the dynamic range of 84 dB, and the maximum input level of $+10$ dBm.

The average power of quantization noise is approximately 11 dB lower than the minimum quantization scale. To avoid losing the SNR in the atmospheric echo, the input galactic noise level should be sufficiently higher than the quantization noise level. Thus we set the gain of pre-amplifier to 25 dB which increases the galactic noise to -75 dBm. Related parameters are shown in Table 5.1.

Sampled and quantized signal is then filtered and down-converted to the baseband with a band width of 2 MHz by a 4-channel digital down-converter (DDC) chip (GRAYCHIP GC4016) on the ECDR-214PCI board. Each DDC channel of the GC4016 consists of three sets of digital filters and decimators. The first part of the filter set is a 5-stage cascaded-integration-comb filter with a programmable decimation factor N_{dec} . Figure 5.6 shows a block diagram of CIC filter in a 1-stage representation. An N_{sta} -stage CIC filter consists of three parts: an N_{sta} -stage integrator, a decimator and an N_{sta} -stage differentiator. This type of digital filter is suitable for a high speed processing needed at the front stage of a down-converter since a long register array is not required as is in ordinary finite-impulse-response (FIR) filters. The fixed parameter $N_{\text{sta}} = 5$ specifies the level of the spectral sidelobe, therefore, it is the factor to controls spectral contamination along with the temporal decimation process.

The second digital filter is a symmetric 21-tap (or an asymmetric 11-tap) FIR filter followed by a decimator with the factor of 2. The third digital filter is a symmetric 63-tap (or an asymmetric 31-tap) FIR filter also with a decimator of the factor 2. These two FIR filters can be used to form a spectral mask with sharp cutoffs to meet, for example, a specific wireless communication standard. In our observations, this spectral window is designed to used almost entire band width in the output signal of 2 MHz. The coefficients of these filters are listed in appendix. Though a resampler follows the three sets of digital

Table 5.1: System parameters for digital receivers.

Antenna	4-element Yagi
Bandpass Filter	
Band Width	10 MHz
Pre-Amplifier	
Gain	25 dB
Noise Figure	< 2 dB
AD Converter	
Analog Input	2 channels
Resolution	14 bits
Maximum Allowed Input	+10 dBm
Sample Rate	64 MHz
Digital Down Converter	
Conversion Rate	1/32
Recording	
Coherent Integration	30 times
Resolution	32 bits
Sample Rate	2 MHz

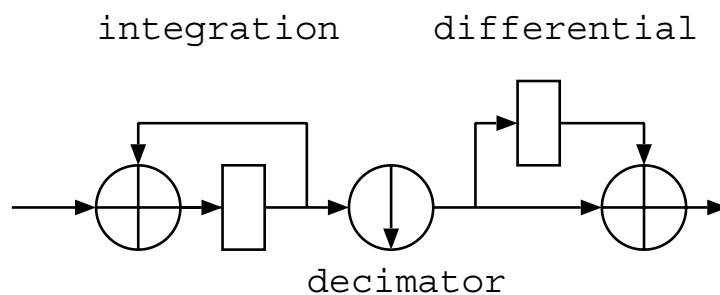


Figure 5.6: Block diagram of a 1-stage Cascaded-Integration-Comb filter. Rectangles show delay elements.

Table 5.2: Observational modes of EAR. NCOH, NICOH and NFFT are the parameters used in the EAR side. (IPP: Inter-Pulse Period, PL: Pulse Length, SPL: Sub-Pulse Length, NCOH: Number of Coherent Integration, NICOH: Number of Incoherent Integration, NFFT: FFT data length)

Mode	Target	IPP(μ s)	SPL(μ s)	PL(μ s)
A	Troposphere	200	1	1
B	Stratosphere	400	1	16
C	Stratosphere	400	1	16

Mode	NCOH	NICOH	NFFT	Compression
A	64	5	256	no
B	32	5	256	complementary
C	32	5	256	complementary

Mode	Beam Directions (Azimuth, Zenith Angle)				
A	(0,0)	(45,30)	(135,30)	(225,30)	(315,30)
B	(0,0)	(0,30)	(90,30)	(180,30)	(270,30)
C	(0,0)	(0,10)	(90,10)	(180,10)	(270,10)

filters mentioned above, in the last part of the DDC chip, this function is not used in this study. Down-converted signal is thus read from a CPU via a PCI bus, and is coherently averaged over 30 times to compress the data with repetition intervals of 1 msec.

5.3 Observational scheme

Observations were made from 25 through 29th September 2004. Observational modes of the EAR are shown in Table 5.2. The modes were altered in order from A to C every 82 seconds. The Mode-A is aimed for tropospheric observations that utilize a short pulse of 1 μ sec. Modes-B and -C are mainly aimed for stratospheric observations that make use of longer pulses of 16 μ sec, which have a gain of 16 times as much as that of Mode-A. In every mode, the direction of the transmitting beam changes in a pulse to pulse manner in the order shown in Table 5.2.

The observational scheme differs between the monostatic EAR and the multistatic receivers. For the monostatic EAR, received signals are sampled and quantized at the rate of 1 MHz after de-modulation. A pulse compression process of a complementary

code pair follows only for Modes-B and -C. Signals are further coherently averaged at the interval of the IPP \times the number of beam directions ($=5$), which corresponds to 1, 2 and 2 msec for Modes-A, -B and -C, respectively, prior to being stored on HDDs.

For the multistatic receivers, received signals are oversampled and quantized at a rate of 2 MHz via onboard down-converters. After being transferred into the memory of a PC via a PCI bus, the 16-bit digitized signal is coherently averaged over 30 times with a constant interval of 1 ms, then stored on HDDs. In this observation, pulse compression process for complementary codes was not employed because of difficulty of the absolute time synchronization between the EAR and receiver. We have mistakenly set this value to 1 ms although it should have been set to 4 ms to cover the complementary code sequences alternately repeating at the interval of 2 ms. As a result, the coherent averaging worked well only for Mode-A and led to sum up both of the complementary codes. Influences of this unexpected process will be discussed in later sections.

5.4 Post-observational signal processing

5.4.1 Pre-processing

Since an absolute-time synchronization is not established between the EAR and the receiver sites and even between the each receiver, firstly it is necessary to seek ground pulses, which directly propagate on the surface of the ground to receivers without being scattered, to mark reference time in the data at each receiver. Although ground pulses are much larger than ground clutters, we set the reference point in the middle of increasing slope by fitting a Gaussian function to avoid choosing a point contaminated by ground clutters. Secondly, to solve a cyclic ambiguity of the beam directions, patterns of amplitude sequence of ground pulses are compared and sorted so as to match each other.

In addition to the time synchronization, the reference frequency was not completely synchronized. Although the EAR and each receiver site were synchronized by GPS receiver systems, the accuracy of the reference clocks were about 10^{-9} and it corresponds to a Doppler velocity of 0.15ms^{-1} . Furthermore, the GPS reference clock shows several strange behavior such as small frequency hops at every one second and eventual frequency change. The second phenomena seems to occur when a satellite set is changed to another. Figures 5.7 and 5.8 shows an example of phase measured at the ground pulses.

To compensate the frequency instability, each signal is adjusted so that the reference phases measured at the ground pulses become constant. The adjustment phase is calculated using summed signal over all the antennas in order to decrease the influence of noise (Fig. 5.9).

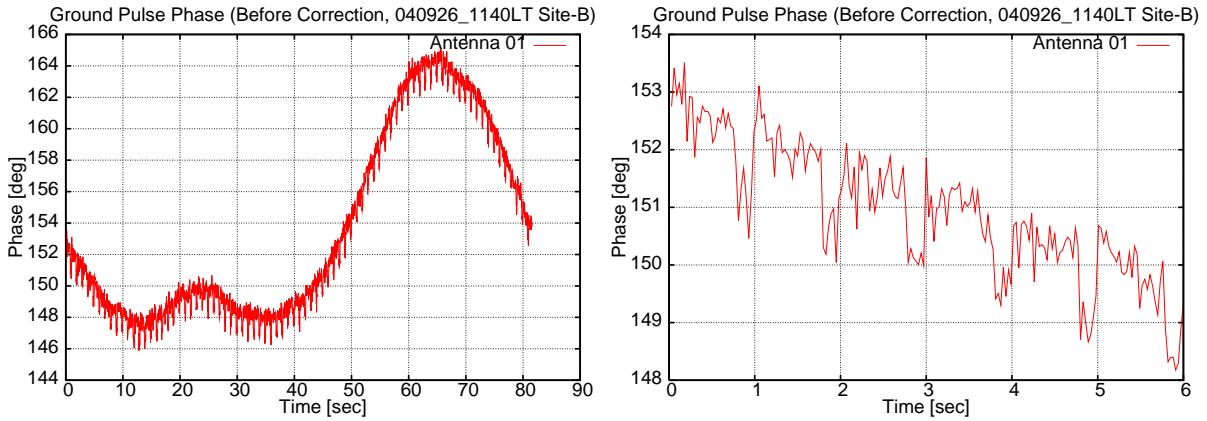


Figure 5.7: Phases measured at ground pulses by the antenna No.1. The right panel magnifies the first 6 s of the left panel. A periodical leap with an interval of 1 s appears overlaid with long time fluctuation.

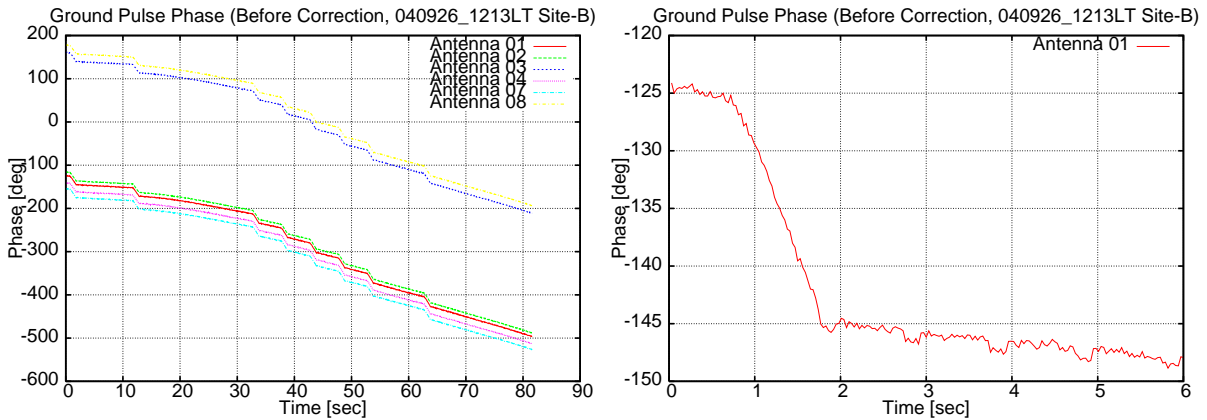


Figure 5.8: Phases measured at ground pulses by several antennas. The right panel magnifies the first 6 s of antenna No.1. Sporadic phase variations are observed which seem to be caused by transitions of sets of the GPS satellites.



Figure 5.9: Phase of ground pulses after the compensation process. Fluctuations are removed compared to Fig. 5.7(right).

5.4.2 Array Signal Processing

The procedure for post-observation signal processing to derive an altitude-velocity spectrum from the received signals is as follows. All the signals are first divided into samples in a range-by-range manner at each beam direction. Second, to gain the SNR, the phase of the signal of each antenna is rotated to match the relative phase angle considering a plane wave from the corresponding target volume. Here, let \mathbf{d}_n be the relative displacement of the n -th antenna; thus the relative phase rotation of an echo is derived as,

$$\phi_n = \mathbf{k} \cdot \mathbf{d}_n \quad (5.6)$$

where \mathbf{k} is the wave number of the echo from a target volume. This process is equivalent to what is called post beam steering, in which the desired direction of the plane wave is different depending on not only the transmitted beam direction, but also the observation height.

Third, taking advantage of independently recorded signals for every antenna, ground clutter is eliminated using an adaptive spatial filtering technique (Kamio et al., 2004; Cheong et al., 2006). This process is especially important for multistatic observations, because each multistatic receiver array consists of only 10 antennas and thus its sidelobe level is approximately 15 dB higher than that of the monostatic EAR (see Figures 5.10 and 5.11) This sidelobe level is not sufficiently low to suppress ground clutter, resulting in a serious contamination from clutter in the atmospheric echo. To provide an accurate estimate of wind velocity, we employed an adaptive signal processing technique that forms a spatial filter to eliminate ground clutter.

The procedure is described as the problem of finding optimal weights which are used in the weighted sum of signals received at the antennas which make up a receiver array. \mathbf{x} denotes a set of signals associated with the n -th antenna as

$$\mathbf{x}(i) = (x_1(i), x_2(i), \dots, x_N(i))^t, \quad (5.7)$$

and thus \mathbf{w} a set of weights for summation as

$$\mathbf{w} = (w_1, w_2, \dots, w_N)^t. \quad (5.8)$$

The optimal weight vector is given as a solution that minimizes the resulting average power

$$P = \mathbf{w}^H \mathbf{R} \mathbf{w} \quad (5.9)$$

where \mathbf{R} is an averaged covariance matrix given by

$$\mathbf{R} = \begin{pmatrix} \Sigma x_1(i) x_1^H(i) & \Sigma x_1(i) x_2^H(i) & \dots & \Sigma x_1(i) x_N^H(i) \\ \Sigma x_2(i) x_1^H(i) & \Sigma x_2(i) x_2^H(i) & \dots & \Sigma x_2(i) x_N^H(i) \\ \vdots & \vdots & \dots & \vdots \\ \Sigma x_N(i) x_1^H(i) & \Sigma x_N(i) x_2^H(i) & \dots & \Sigma x_N(i) x_N^H(i) \end{pmatrix} \quad (5.10)$$

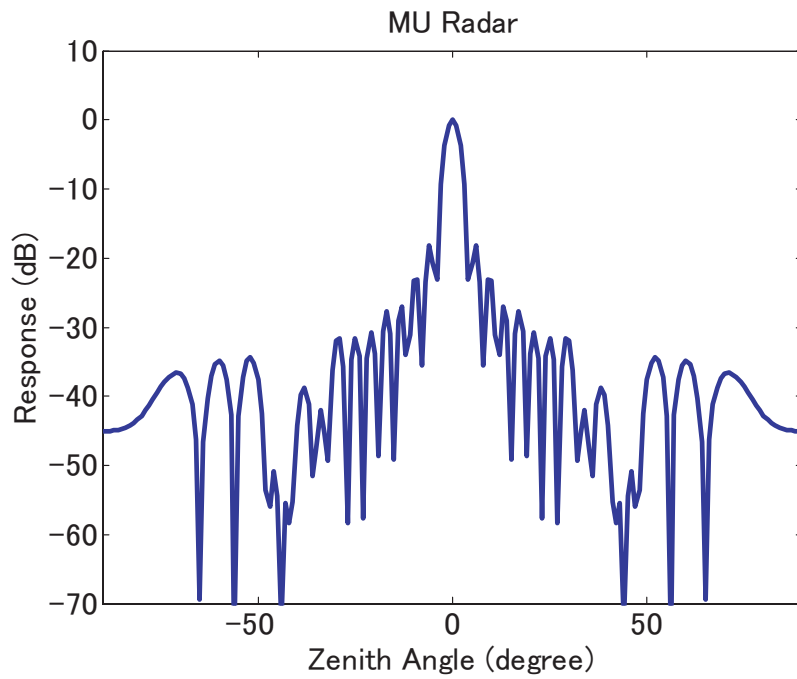


Figure 5.10: The beam pattern of MU radar.

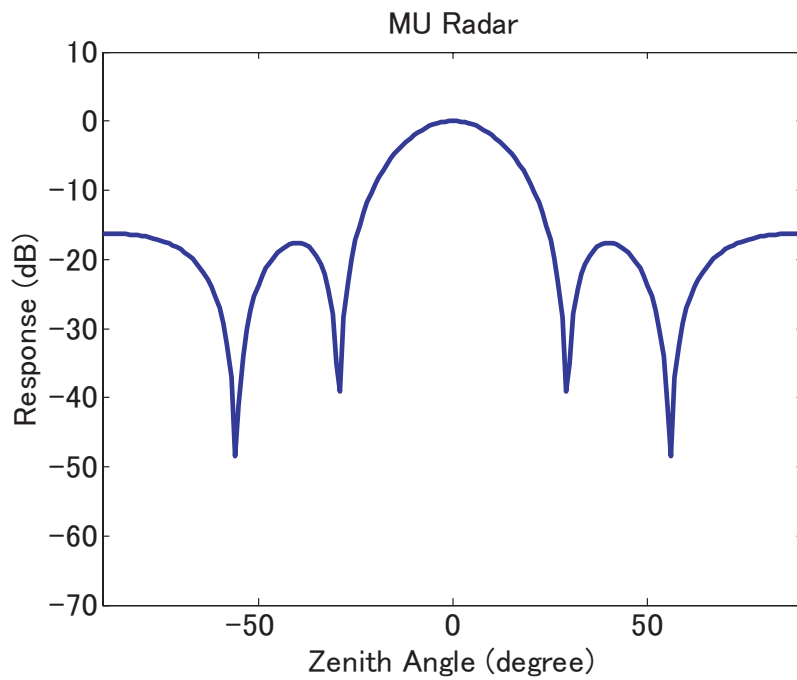


Figure 5.11: A beam pattern of a two-dimensional array with 10 antennas.

under the condition of constant gain to waves coming from the target volume, which is given by

$$\mathbf{c}^H \mathbf{w} = 1, \quad (5.11)$$

where

$$\mathbf{c} = (e^{-i\phi_1}, e^{-i\phi_2}, \dots, e^{-i\phi_N})^t. \quad (5.12)$$

The optimal weight \mathbf{w}_{opt} is given by

$$\mathbf{w}_{\text{opt}} = \frac{R^{-1} \mathbf{c}}{\mathbf{c}^H R^{-1} \mathbf{c}}. \quad (5.13)$$

Figure 5.15 and Fig. 5.16 show altitude-velocity spectra before and after, respectively, the adaptive clutter suppression process. A strong ground clutter component, which is dominant at and around the zero Doppler component in Fig. 5.15 is almost completely suppressed in Fig. 5.16. It should be noted that the atmospheric echo components with zero Doppler frequency seen at 2.5–3.5 km height are conserved in this processing. There is a slight depression of the SNR as seen in the echoes at 6–7 km, which is the side effect of controlling the phase of individual antenna elements.

Doppler velocity is, basically, estimated by fitting the Gaussian function to a spectrum around the peak of the echo. This procedure is done by fitting a parabolic function in a logarithmic scale to the spectral peak and an adjacent component on each side. It should be noted that the Doppler velocity in some data used in this study are corrected manually to eliminate an obvious misestimate with this algorithm.

5.5 Resulting 3D wind field

During the observation from 25 through 29th September 2004, of over 100 hours of data, it exceeds 3 tera bytes, were obtained. In this study, it is beyond the scope to examine in detail the fine scale wind velocity field. Here we only show preliminary examples of the 3-D wind velocity field to demonstrate the capability of the multistatic radar system.

By combining the three observational modes, A–C, listed in Table 5.2, 15 horizontal locations are sampled at each height with a time resolution of about 4 minutes. Fig. 5.17 shows an example of the 3-D wind velocity field thus obtained for three consecutive observation cycles at a height of 3.8 km. Three arrows in the insets at the corners of each figure denote the wind velocity vectors determined by the monostatic EAR. The solid arrows show the horizontal wind velocity components, and the dashed arrows show the vertical component.

The three arrows starting from the origin represent the three estimates with Modes A, B, and C, all of which include this location. The differences among these arrows indicate

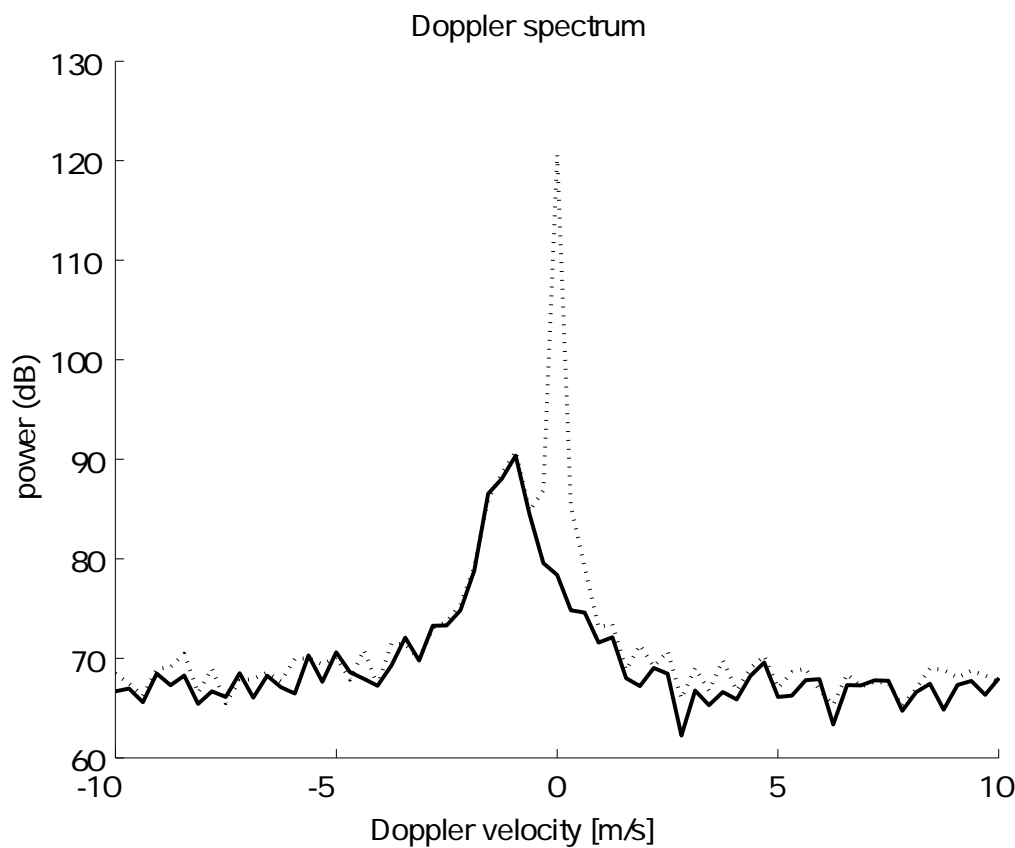


Figure 5.12: Doppler spectra (altitude=2136m) observed by Site-B made with no adaptation (dashed) and with the adaptive clutter suppression technique. The conspicuous clutter component at the center of Doppler velocity has been cancelled by the algorithm.

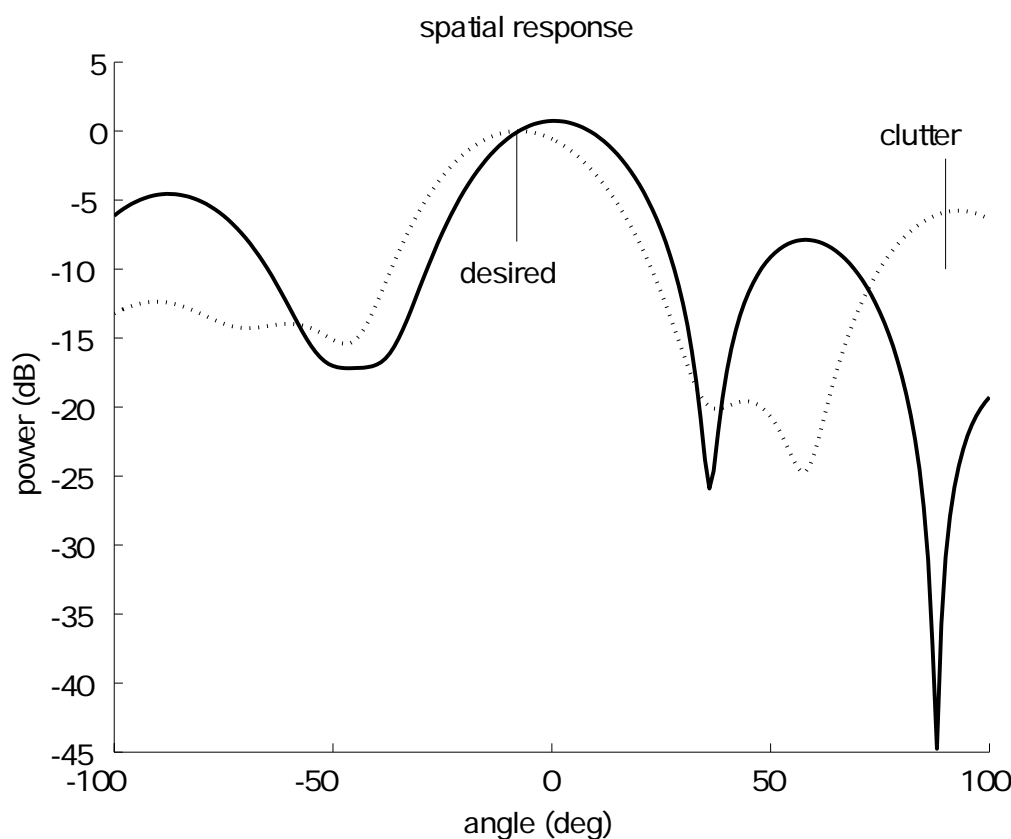


Figure 5.13: Spatial responses of the array with no adaptation (dashed) and with the adaptive clutter suppression technique (solid) corresponding to the data utilized in Fig.5.12. This pattern is swept in the plane including the receiver (site-B) the target (shown as desired) and a clutter. This clutter is found by Capon's imaging algorithm. A clear null is formed by the adaptation.

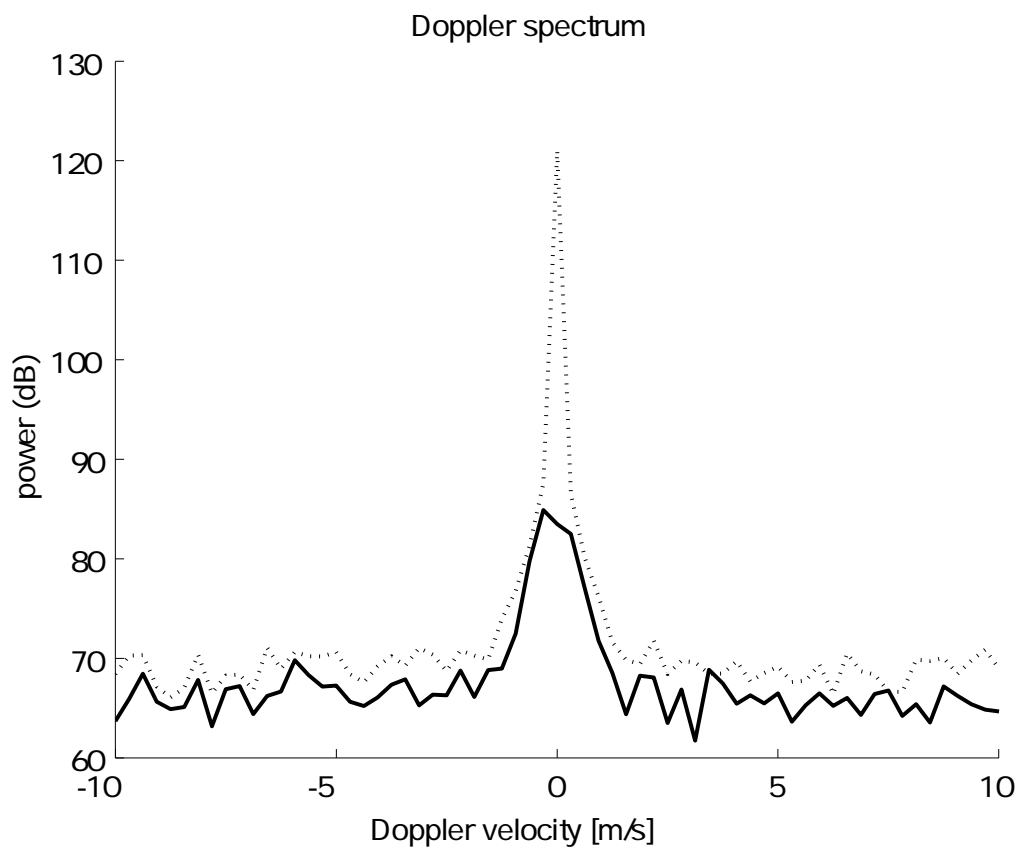


Figure 5.14: Doppler spectra (altitude=3295m) observed by Site-B made with no adaptation (dashed) and with the adaptive clutter suppression technique. A case that the Doppler velocity of the atmospheric echo is around the zero.

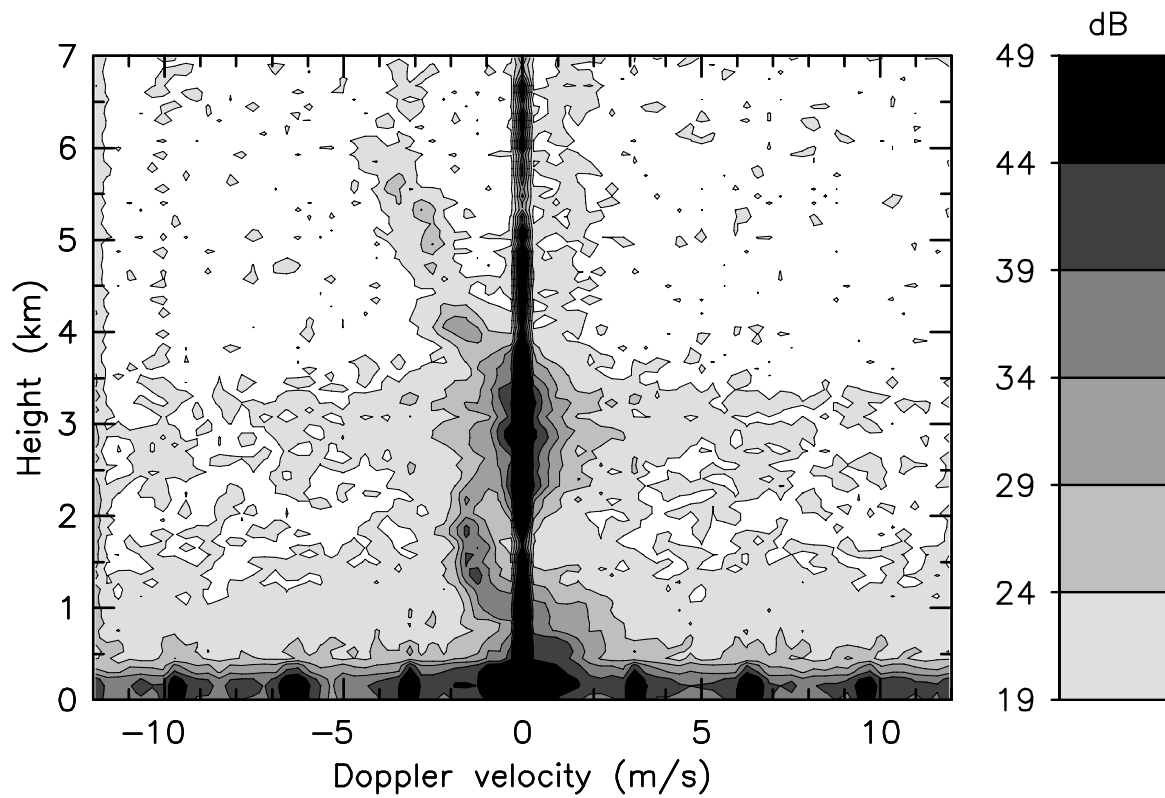


Figure 5.15: An altitude-velocity spectrum observed at site-B at 12:00 LT 26, Sep, 2004, in mode-A for the direction (225,30), after a coherent sum of 8 antennas out of 10. (For reasons of the stability of the equipment, only 8 antennas worked at this period.)

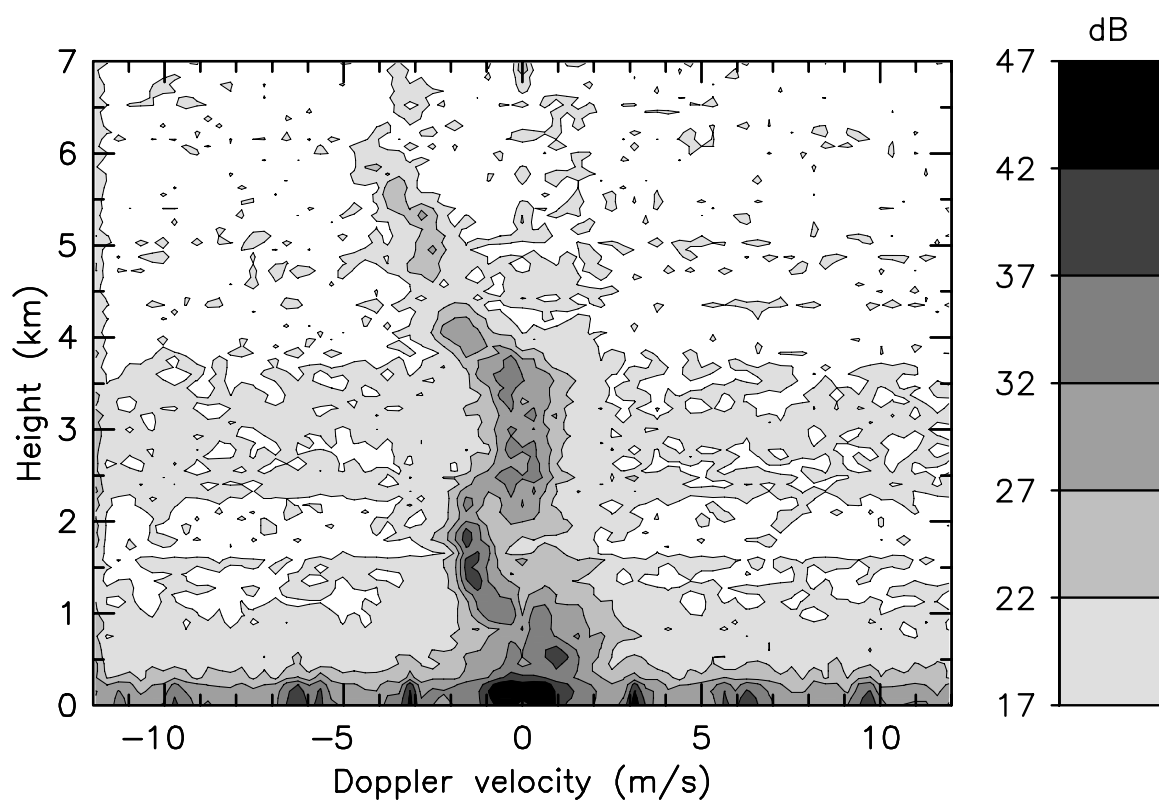


Figure 5.16: The same as Fig.5.15 but with the adaptive spatial filtering procedure.

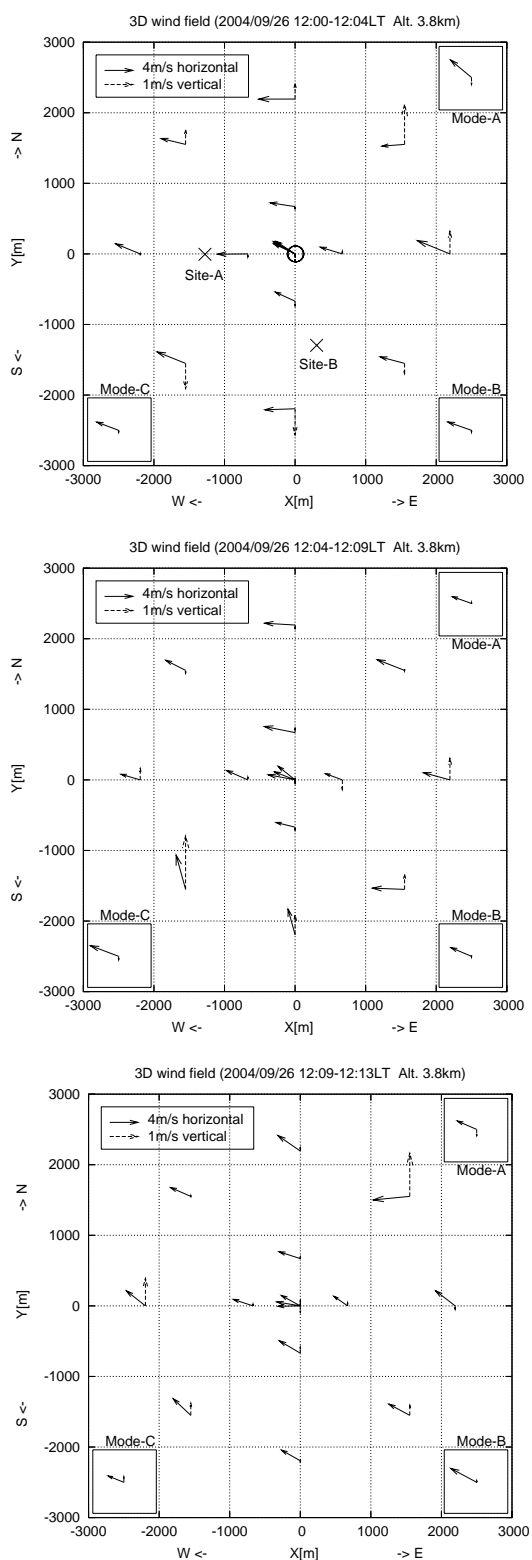


Figure 5.17: Example of a horizontal section of the wind velocity field at three consecutive observation cycles. The origin of each arrow is the center of the target volume. The arrow with solid line shows a 2D horizontal velocity vector (u,v) , and that with a dashed line shows a vertical component w . In the top panel, the small circle at the origin shows the 3dB diameter of The transmitted beam (one way) and the two crosses show the position of the receiver sites.

temporal variations of the wind velocity over the observation cycle of 4 minutes, as well as the random errors. It should be noted that the vertical component is magnified by 4 times compared to the horizontal component. As the beam width of 3.4° corresponds to the horizontal resolution of 240 m at this height, the wind velocity field may be under-sampled especially at around the 8 locations on the outer circle.

The height of 3.8 km is chosen because the echo power profile shows a clear peak at this altitude, and thus the problem of range sidelobes can be eliminated in Modes B and C of Table 5.2. While, in principle, the pulse compression scheme of the 16-element complementary codes used in these modes has no range sidelobe, we mistakenly averaged the echoes of the complementary pulse pair in the real-time signal processing before the pulse compression. The two sequences that constitute the complementary codes have the same pattern for the first 8 elements, and the same pattern with the opposite sign for the latter 8 elements. As a result, the pulse compression turned into an 8-element binary code with a fairly high range sidelobe level after the averaging.

Since Mode A employs a single pulse, there is no problem regarding the range sidelobe. Instead, the signal-to-noise ratio of Mode A is 9 dB lower than those of Modes B and C. The estimation error of the wind velocity at the directions measured with Mode A, which are at the diagonal locations in Fig. 5.17, is thus larger than those of the other locations measured with Modes B and C.

The errors are for data with sufficiently high signal-to-noise ratios, which is the case for Modes B and C that are evaluated according to the discussion in section 2.4. Fig. 5.18 shows the expected random errors of the three wind components as a function of the observation point at a height of 3.8 km. The difference in the zonal and meridional components is due to the non-orthogonal alignment of the two baselines between the EAR and the receiver arrays. The error of the estimated zonal and meridional wind components is about 1.0 m/s at near the center of the illuminated area, and increases to about 1.4 m/s at the outer edge.

While the mean horizontal wind is consistently westward with a slight northward offset at all locations in the three observation cycles in Fig. 5.17, there is a substantial perturbation superimposed on the mean wind field even at the non-diagonal locations observed with Modes B and C. Although the magnitude of the perturbation falls within the limit of accuracy indicated by Fig. 5.18 at some locations, there are cases exceeding this limit such as a clear trend along the Y -axis from -2200 m toward $+2200$ m during 12:04–12:09LT. It should be noted that large perturbations at diagonal locations observed with Mode A contain larger random errors than at other locations, and thus require further verification.

The error of the vertical wind component depends largely on the relative location of the observation point with respect to the baseline. While it is less than 0.2 m/s above the center of the baseline, the error increases rapidly as the distance increases, and exceeds 0.4 m/s when the point is above outside the baseline. In our current observations, the vertical wind component is most reliable at the locations in and around the fourth

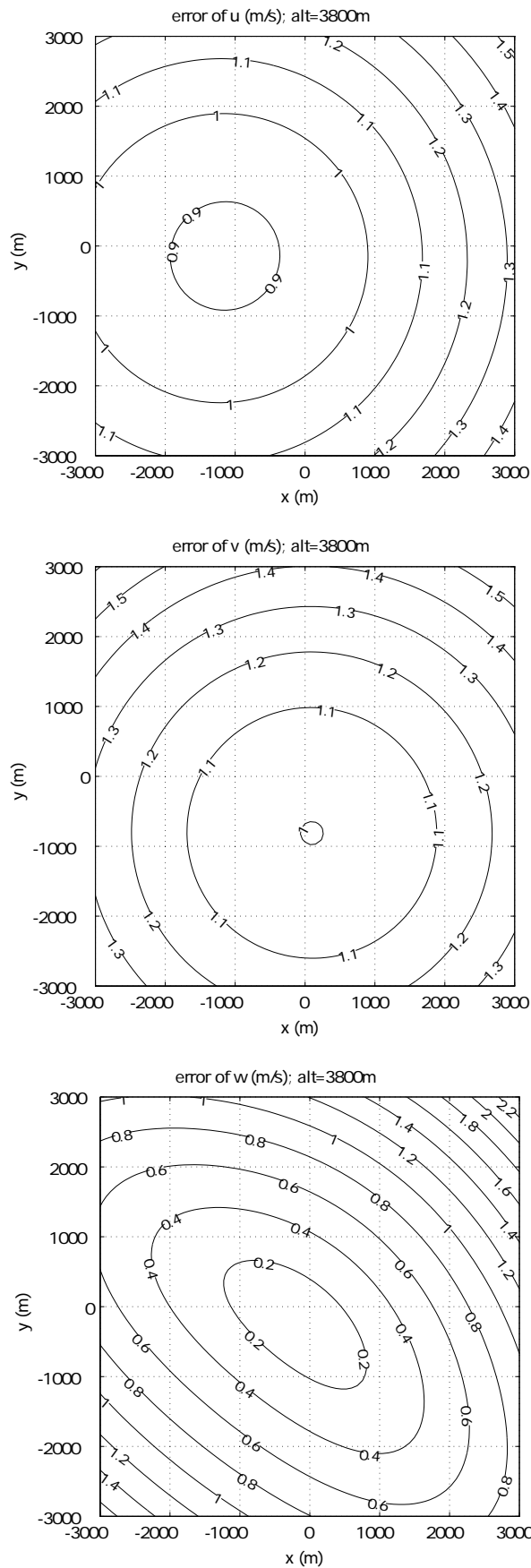


Figure 5.18: Estimation error of u , v and w in a horizontal section at 3800 m in altitude. Estimation error of each radial velocities is assumed to be 0.104 ms^{-1} .

quadrant. The downward velocity of 1.0 m/s at the south point at 12:00-12:04, and the upward velocity of 0.9 m/s at the west point at 12:09-12:13 seem to be examples of real perturbations, which are most likely due to weak local convections. However, more careful verification is required to assess perturbations in the vertical component.

To further examine the significance of the perturbation wind field, we compared the vertical profiles of the wind field estimated by the proposed multistatic and by the monostatic methods using the EAR alone. Fig. 5.19 shows the vertical profile of the two horizontal wind components observed by Modes-A, -B, and -C for the period of the middle panel of Fig. 5.17. The multistatic method is applied to the data of the vertical beam position, which is included in all three modes. The solid line is the monostatic estimate assuming horizontal uniformness using the five beams observed by the EAR, and the dotted line is the multistatic estimate. It is clear from this figure that the wind profiles estimated by these two methods often show clear and persistent differences over a large height interval of more than 1 km. As the height resolution is 150 m, this persistent difference is clear evidence that these are due to horizontal inhomogeneity of the wind field, and not due to random errors in the estimates. This comparison suggests that instantaneous profiles observed by the DBS method with a monostatic radar may have an error of up to 3 m/s. The large vertical extent of this perturbation suggests that it is related to convective motions, but we need to avoid speculative discussions as no supporting meteorological data from during the observation period is available.

It should be noted that the profiles of 12:04LT are taken by Mode-A, which has a significantly lower SNR because it uses a single pulse. The data with detectability of less than 3 is removed from the profile, which is the case for the data around heights of 4.5 km. On the other hand, data of 12:06LT and 12:07LT are processed with pulse compression of 8 bits. As described before, this mode may suffer from code sidelobes, and thus should be interpreted with care. If the echoes are contaminated with code sidelobes, the wind velocity estimate is biased to that of a different altitude, differing by up to 1.2km from the center of the scattering volume. However, if a layer with a strong echo power affects neighboring heights, they would show the same wind velocity as that of the affecting layer, resulting in a constant velocity profile with height. The profiles shown here always show a clear and continuous trend with height, which is direct evidence that the code sidelobes do not have any significant effect in this case. Similar persistent difference between the two methods is also found in data of 12:04LT, which is free from the problem of code sidelobe.

5.6 Observation for CPEA-II in 2005

For about one month from November 24, 2005, we made another multistatic observations at the EAR as part of the CPEA-II campaign, with modified equipment based on the knowledge raised in preceding observations in 2004. The receiver site structure is rather

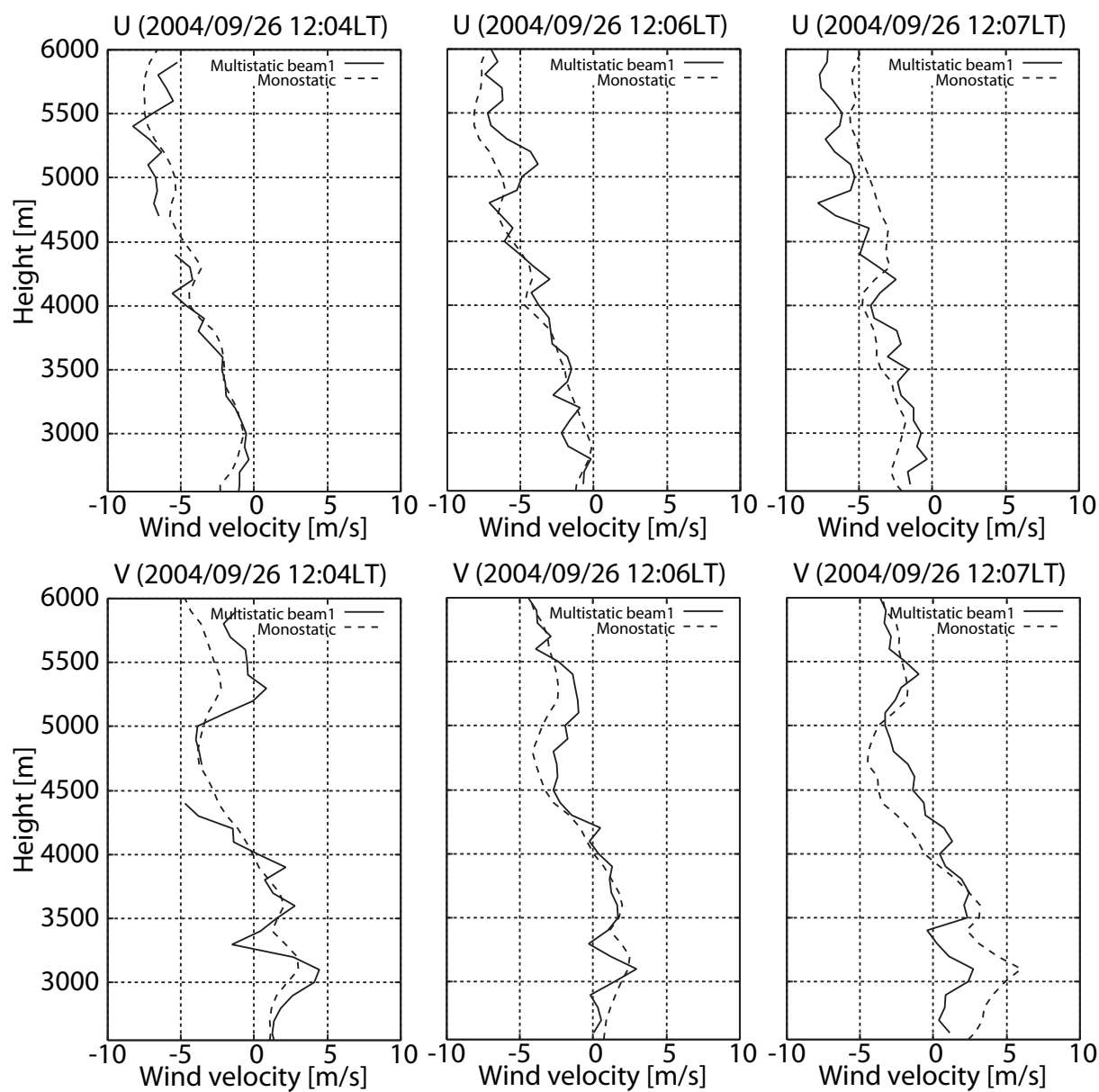


Figure 5.19: Vertical profiles of the zonal (top row) and the meridional (bottom row) wind components estimated by the two observation methods. The solid line is by the monostatic method using the data of the EAR alone, and the dotted line is by the proposed multistatic method.

Table 5.3: The number of antennas at each site for observations in 2005.

	Site-A	Site-B	Site-C
Yagi	12	13	1
dipole	2	3	1

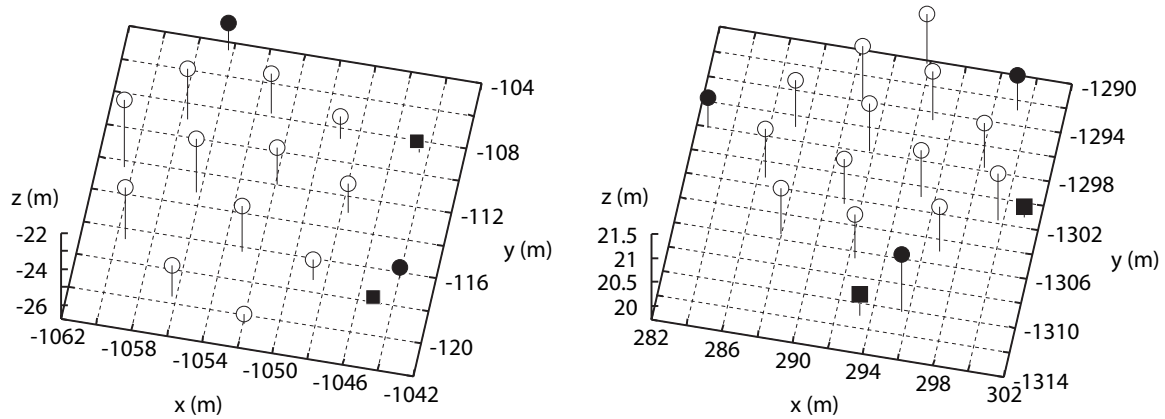


Figure 5.20: Antenna displacement of Site-A and Site-B in the observations for CPEA-II. Open and closed circles show positions of Yagi and dipole antennas, respectively. Closed squares are the reference points used for the measurement.

changed; Site-A is moved approximately 200 m in the east for access and security reasons, and a small auxiliary receiver set named Site-C is added just beside the EAR. At each site, not only Yagi antennas, but also dipole antennas are added as shown in Table 5.3. Dipole antennas are vertically set particularly for clutter rejection making use of its beam pattern that is in a level omni-directional and has very low gain toward the zenith. It is intended to utilize this property in the arrays to subtract a clutter signal traveling from a low elevation without affecting atmospheric echo which mostly arrives from a high elevation in Yagis.

For the arrays at Site-A and -B, a newly developed antenna arrangement that does not have grating-lobes as discussed in Chapter 4. Figure 5.20 illustrate the arrangement measured using a theodolite and the direction of the Sun. Dipole antennas are set in the peripheral areas.

Observation scheme is to a large extent modified. Table 5.4 shows the beam modes employed the observations. Mode-B is an observation mode specialized for this multistatic observation. In this mode, beam directions are concentrated at south-west area from the EAR where this tri-static system has the best accuracy in 3D wind field estimation.

Table 5.4: Observational modes in 2005.

Mode	Target	IPP(μs)	SPL(μs)	PL(μs)
A	Tropo/Stratosphere	400	1	16
B	Tropo/Stratosphere	400	1	16
C	Troposphere(RASS)	200	1	8

Mode	NBEAM	NCOH	NICOH	NFFT	Compression
A	6	64	5	256	Spano
B	8	32	5	256	Spano
C	5	32	5	256	Spano

Mode	Beam Directions (Azimuth, Zenith Angle)				
A	(0,0)	(0,10)	(90,10)	(0,0)	(180,10)
	(270,10)				
B	(0,0)	(135,20)	(225,20)	(315,20)	(180,30)
	(210.1,30)	(240.1,30)	(270,30)	(270,10)	

5.7 Summary

The first VHF tristatic atmospheric radar observations were made in September 2004, at the EAR, Indonesia, using newly developed digital receiver systems with a fully independent data recording capability. The two receiver sites named Site-A and -B, both consisting of 10 of 3-element Yagi antennas, are installed approximately 1300m away in the west and south, respectively, from the EAR. Data of over 100 hours were obtained in these observations made with pulse modes of a single pulse mode and complementary pulse modes. Analyses were made mainly for the single pulse mode because the coherent integration interval was mistakenly set for the pulse mode which does not fit for complementary pulse pairs.

In the data processing procedure, time and fine frequency synchronization was made using directly received ground pulses and coherent syntheses were made in each array by the post-set beamforming technique. Together with these techniques, an adaptive array processing technique with the MVDR algorithm was applied and strong ground clutters were successfully canceled as a result. After Doppler velocity estimation on these data, snapshots of high resolution 3D wind velocity were obtained across a volume of about 4 km in diameter. Compared to theoretical estimation errors, the result suggests the existence of significant perturbations within this field.

Based on these experiments, we made modified multistatic observations at the EAR for November to December 2005. The major points of the modifications are as follows:

1. Introduction of Spano code and required modification on softwares of the digital receivers for real-time pulse compression.
2. Introduction of grating-lobe free antenna array for a more robust clutter rejection with the adaptive processing.
3. Introduction of vertical dipole antennas also for a robust clutter rejection taking advantage of their different beam pattern from that of Yagis.

Chapter 6

Concluding Remarks

A high-resolution 3D wind field observation technique using fully adaptive small antenna arrays composed of low-gain passive receiver together with a rapid scanning high-gain large VHF wind profiler was presented. Due to its adaptive capability, an adaptive clutter rejection technique and a post-set beam steering technique are utilized simultaneously to obtain the maximum gain to a target and null gain to ground clutters. Employing these techniques, the first tropospheric observations were successfully made at the Equatorial Atmosphere Radar site and 3D vector wind fields were retrieved. These result imply the existence of small scale perturbation in the wind field, which was previously ignored in practical monostatic radar observations, and supports a further investigation.

In each chapter, we discussed separate techniques in detail and also some peripheral topics. In chapter 1, we briefly reviewed basic knowledge of adaptive beamforming technique and early work on high-resolution radar and bistatic/multistatic radar.

In chapter 2, characteristics and estimation errors of a bistatic radar in comparison to those of a dual-Doppler radar that has two independent radars. Directionally dependent estimation errors were described as error ellipses and we discussed drawback in accuracy of multistatic radar compared to multi-Doppler radar. With reference to the target shape in multistatic atmospheric radar, the deformation effect due to its systematic asymmetry were discussed. In conclusion, it is found that the effect result in degrading the vertical resolution in low altitude region compared to the base line between the radar and receivers.

In chapter 3, adaptive array processing techniques for clutter rejection and high-resolution analysis were discussed. A possible instability in atmospheric radar applications was presented, and a solution employing a norm constraint was introduced. This robust algorithm was demonstrated in a real observation with the MU radar and it showed largely better performance in the regard of noise suppression without losing its clutter rejection capability.

In chapter 4, a new look on antenna arrangement for adaptive array applications was introduced and a simple trial-and-error optimization algorithm based on a beam-space evaluation function was investigated. In a case study on specific number of antennas, a

particular array was obtained as an optimum arrangement that has exceptional performance in its peak-sidelobe. In addition, a mathematical interpretation of this algorithm using a potential function was introduced, and it is shown a fast optimization algorithm based on steepest descent of the potentials is equivalent to a minimization in the beam-space evaluation. This technique is expected to be utilized for a large scale planer array.

In chapter 5, based on the observations made in the EAR site, development of digital receivers, observational schemes, signal processings and data analyses were described. In addition, 3D vector wind field retrieved in these observations were presented within a space in which usually uniformity assumption is applied with monostatic observations. As a result, fine perturbations appeared which have conventionally been ignored appeared.

Appendix

Derivation of Error Ellipses

When 2D velocities v_x and v_y and observed components u_0 and u_1 are linearly related, the observation equation is written as

$$\begin{pmatrix} u_0 \\ u_1 \end{pmatrix} = \begin{pmatrix} a & b \\ c & d \end{pmatrix} \begin{pmatrix} v_x \\ v_y \end{pmatrix}. \quad (6.1)$$

Then, the *true* velocities are obtained from observed components by

$$\begin{pmatrix} v_x \\ v_y \end{pmatrix} = \begin{pmatrix} a & b \\ c & d \end{pmatrix}^{-1} \begin{pmatrix} u_0 \\ u_1 \end{pmatrix}. \quad (6.2)$$

Taking observation errors into account, the linear estimation is given by

$$\begin{pmatrix} v_x + T_x \\ v_y + T_y \end{pmatrix} = \begin{pmatrix} a & b \\ c & d \end{pmatrix}^{-1} \begin{pmatrix} u_0 + S_0 \\ u_1 + S_1 \end{pmatrix} \quad (6.3)$$

where we refer to T_x and T_y as *estimation errors*, and to S_0 and S_1 as *observation errors*. The relation between these errors is

$$\mathbf{T} = A^{-1} \mathbf{S} \quad (6.4)$$

where

$$\mathbf{T} = \begin{pmatrix} T_x \\ T_y \end{pmatrix}, \quad A = \begin{pmatrix} a & b \\ c & d \end{pmatrix} \quad \text{and} \quad \mathbf{S} = \begin{pmatrix} S_0 \\ S_1 \end{pmatrix}. \quad (6.5)$$

We here assume that the probability variable S obeys a Gaussian distribution of $\mu = 0$ and $\text{Var} = \sigma_0^2$, which is

$$P[S_0] = p_0(s_0) = \frac{1}{\sqrt{2\pi}\sigma_0} \exp\left[-\frac{s_0^2}{2\sigma_0^2}\right], \quad (6.6)$$

and, in the same manner, S_1 obeys

$$P[S_1] = p_1(s_1) = \frac{1}{\sqrt{2\pi}\sigma_1} \exp\left[-\frac{s_1^2}{2\sigma_1^2}\right]. \quad (6.7)$$

We also assume S_0 and S_1 are independent, in other words, the covariance is given by

$$\Sigma_{ss} = \begin{pmatrix} \sigma_0^2 & 0 \\ 0 & \sigma_1^2 \end{pmatrix}. \quad (6.8)$$

Therefore the joint pdf can be written as

$$p_{01}(\mathbf{s}) = p_{01}(s_0, s_1) = p_0(s_0)p_1(s_1) = \frac{1}{2\pi\sigma_0\sigma_1} \exp\left[-\frac{s_0^2}{2\sigma_0^2} - \frac{s_1^2}{2\sigma_1^2}\right]. \quad (6.9)$$

An error ellipse is derived by a contour of this joint pdf. When we define an error ellipse to be a contour that gives the level of $e^{-1/2}$ from the top of the pdf, the ellipse for eq.(6.9) is given by

$$\frac{s_0^2}{\sigma_0^2} + \frac{s_1^2}{\sigma_1^2} = 1. \quad (6.10)$$

In a matrix representation, it is

$$\mathbf{s}^t \Sigma_{ss}^{-1} \mathbf{s} = 1. \quad (6.11)$$

According to the random variable theory, a linear transform eq.(6.4) gives a transform of pdf;

$$p_{xy}(\mathbf{t}) = p_{xy}(t_x, t_y) = |\det A^{-1}| p_{01}(A\mathbf{T}) \quad (6.12)$$

$$= \frac{1}{2\pi\sigma_0\sigma_1 |\det A|} \exp\left[-\frac{(at_x + bt_y)^2}{2\sigma_0^2} - \frac{(ct_x + dt_y)^2}{2\sigma_1^2}\right]. \quad (6.13)$$

The equation of the ellipse for \mathbf{t} is thus given by

$$\left(\frac{a^2}{\sigma_0^2} + \frac{c^2}{\sigma_1^2}\right) t_x^2 + 2\left(\frac{ab}{\sigma_0^2} + \frac{cd}{\sigma_1^2}\right) t_x t_y + \left(\frac{b^2}{\sigma_0^2} + \frac{d^2}{\sigma_1^2}\right) t_y^2 = 1. \quad (6.14)$$

Clearly it is

$$\mathbf{t}^t A^t \Sigma_{ss}^{-1} A \mathbf{t} = 1. \quad (6.15)$$

Woodbury's formula

$$(A + UV^H)^{-1} = A^{-1} - [A^{-1}U(1 + V^H A^{-1}U)^{-1}V^H A^{-1}] \quad (6.16)$$

The dimensions of A , U and T must be compatible. It is reduced as

$$(A + UV^H)^{-1} = A^{-1} - \frac{A^{-1}UV^H A^{-1}}{1 + V^H A^{-1}U}, \quad (6.17)$$

when U and T are vectors.

Derivation of SN ratio (with a signal-noise-clutter model)

Assuming a signal received by an antenna is a composite of noise and clutter, it is described as

$$\mathbf{s}(t) = \sigma \boldsymbol{\nu}(t) + \alpha_d \mathbf{c}_d s_d(t) + \alpha_c \mathbf{c}_c s_c(t) \quad (6.18)$$

where $\boldsymbol{\nu}(t)$ is a random signal vector whose elements obey $N(0,1)$, σ is the standard deviation the random signal, \mathbf{c}_c is the steering vector corresponding to the clutter, $s_c(t)$ is the time series of the clutter, α_d and α_c are their amplitudes, respectively.

Auto-correlation matrix of the signal $\mathbf{s}(t)$ is derived as follows:

$$\begin{aligned} R_{ss} &= E[\mathbf{s}\mathbf{s}^H] \\ &= \sigma^2 I + \alpha_d^2 \mathbf{c}_d \mathbf{c}_d^H + \alpha_c^2 \mathbf{c}_c \mathbf{c}_c^H. \end{aligned} \quad (6.19)$$

When we substitute the first two terms with A , its inverse A^{-1} can be derived as,

$$A^{-1} = \frac{1}{\sigma^2} \left[I - \frac{\mathbf{c}_c \mathbf{c}_c^H}{(\sigma/\alpha_c)^2 + N} \right]. \quad (6.20)$$

The inverse of R_{ss} can be derived by the Woodbury formula as,

$$\begin{aligned} R_{ss}^{-1} &= A^{-1} - \alpha_d^2 A^{-1} \mathbf{c}_d (1 + \alpha_d^2 \mathbf{c}_d A^{-1} \mathbf{c}_d)^{-1} \mathbf{c}_d A^{-1} \\ &= A^{-1} - \frac{\alpha_d^2}{B\sigma^4} \left[\mathbf{c}_d \mathbf{c}_d^H + \left\{ \frac{|\beta|}{(\sigma/\alpha_c)^2 + N} \right\}^2 \mathbf{c}_c \mathbf{c}_c^H - \frac{1}{(\sigma/\alpha_c)^2 + N} (\beta \mathbf{c}_c \mathbf{c}_d^H + \beta^* \mathbf{c}_d \mathbf{c}_c^H) \right] \end{aligned} \quad (6.21)$$

where

$$\begin{aligned} B &= 1 + \alpha_d^2 \mathbf{c}_d \mathbf{c}_d^H \\ &= 1 + \frac{\alpha_d^2}{\sigma^2} \left[\mathbf{c}_d^H \mathbf{c}_d - \frac{\mathbf{c}_d^H \mathbf{c}_c \mathbf{c}_c^H \mathbf{c}_d}{(\sigma/\alpha_c)^2 + N} \right]. \end{aligned} \quad (6.22)$$

For an atmospheric radar application, in which a clutter would generally be much stronger than an atmospheric echo, say $\alpha_c \gg \sigma$, \mathbf{w}_{opt} can be reduced as,

$$\begin{aligned} \mathbf{w}_{opt} &= \gamma \left[\frac{1}{\sigma^2} \left(\mathbf{c}_d - \frac{\beta}{N} \mathbf{c}_c \right) - \frac{N\alpha_d^2}{B\sigma^4} (1 - \cos^2 \Theta) (\mathbf{c}_d - \beta \mathbf{c}_c) \right] \\ &= K \left(\mathbf{c}_d - \frac{\beta}{N} \mathbf{c}_c \right) \end{aligned} \quad (6.23)$$

where $\beta = \mathbf{c}_c^H \mathbf{c}_d$.

The output of array synthesized by MVDR controller is written as

$$s_{out} = \sigma \mathbf{w}_{opt} \boldsymbol{\nu}(t) + \alpha \mathbf{w}_{opt} \mathbf{c}_c s_c(t). \quad (6.24)$$

The first term and the second term describe the noise and a clutter, respectively. The first term is

$$\text{first term} = \frac{\gamma^*}{\sigma^2} \sigma (\mathbf{c}_d^H - \frac{\beta^* \mathbf{c}_c^H}{(\sigma/\alpha)^2 + N}) \boldsymbol{\nu}(t). \quad (6.25)$$

The second term is

$$\text{second term} = \frac{\gamma^*}{\sigma^2} \alpha \beta^* \left[1 - \frac{N}{(\sigma/\alpha)^2 + N} \right] s_c(t) \quad (6.26)$$

$$\simeq 0 \quad \text{when } \alpha \gg \sigma. \quad (6.27)$$

Derivation of Eqs. (5.2) and (5.3)

A bistatic system is described by

$$\begin{pmatrix} u \\ v \end{pmatrix} = \begin{pmatrix} \beta_{11} & \beta_{12} \\ \beta_{21} & \beta_{22} \end{pmatrix} \begin{pmatrix} v_0 \\ v_1 \end{pmatrix} = \begin{pmatrix} \frac{e_{x0}}{2} & \frac{e_{z0}}{2} \\ \frac{e_{x0} + e_{x1}}{2} & \frac{e_{y0} + e_{z1}}{2} \end{pmatrix}^{-1} \begin{pmatrix} v_0 \\ v_1 \end{pmatrix}, \quad (6.28)$$

and its error variance is specified by,

$$\begin{pmatrix} \epsilon_0^2 \\ \epsilon_1^2 \end{pmatrix} = \begin{pmatrix} \beta_{11}^2 & \beta_{12}^2 \\ \beta_{21}^2 & \beta_{22}^2 \end{pmatrix} \begin{pmatrix} \sigma_0^2 \\ \sigma_1^2 \end{pmatrix} \quad (6.29)$$

where e_{xi} and e_{zi} are the components of \mathbf{e}_i . To evaluate estimation error in the vertical beam in respect to the baseline between the radar and a receiver, we set 2 parameters h and b which are the height of the target and the length of the baseline, respectively. Now we obtain $e_{x0} = 0$, $e_{z0} = 1$, $e_{x1} = -b/\sqrt{b^2 + h^2}$ and $e_{z1} = h/\sqrt{b^2 + h^2}$. Letting E represent the standard deviation of error σ_0 and σ_1 , the error variance is derived by substituting them into eq.(6.28),

$$\begin{aligned} \epsilon_0^2 &= E^2 \\ \epsilon_1^2 &= \frac{1}{b^2} (6h^2 + 2h\sqrt{h^2 + b^2} + 5b^2) E^2. \end{aligned} \quad (6.30)$$

Reference

- Abe, K., K. Hirasawa, and H. Watanabe, 1995: Radar sidelobe canceller characteristics in high power interference, *IEICE Trans. Commum.*, E78-B, pp. 1507–1512.
- Alcayde, D., J. Fontanari and P. Bauer, 1982: High latitude neutral atmosphere temperature and concentration measurements from the first EISCAT incoherent scatter observations, *Ann. Geophys.*, Vol. 38, pp. 473–479.
- Amayenc, P., J. Fontanari, D. Alcayde, 1973: Simultaneous neutral wind and temperature oscillations near tidal periods in the F-region over St Santin, *J. Atmos. Terr. Phys.*, Vol. 35, pp. 1499–1505.
- Applebaum, S. P., and D. J. Chapman, 1976: Adaptive Arrays with Main Beam Constraint, *IEEE Trans. Antennas Propagat.*, Vol. AP-24, No. 5, Sep.
- Ares-Pena, F. J., J. A. Rodriguez-Gonzalez, E. Villanueva-Lopez, and S. R. Rengarajan, 1999: Genetic Algorithm in the Design and Optimization of Antenna Array Patterns, *IEEE Trans. Antennas Propagat.*, Vol. 47, No. 3, March.
- Bienvenu, G. and L. Kopp, 1983: Optimality of High Resolution Array Processing Using the Eigensystem Approach, *IEEE Trans. Acoust. Speech Signal Process.*, Vol. ASSP-31, No. 5, pp. 1235–1248, October.
- Blackman, S. and R. Popoli, 1999: *Design and Analysis of Modern Tracking Systems*, Artech House, Norwood, MA.
- Capon, J., 1969: High resolution frequency-wavenumber spectrum analysis, *Proc. IEEE*, vol. 57, pp. 1408–1418, Aug.
- Cheong, B. L., M. W. Hoffman, R. D. Palmer, S. J. Frasier and F. J. Lopez-Dekker, 2006: Phased array design for biological clutter refraction: simulation and experimental validation, *J. Atmos. Oceanic Technol.*, in press.
- Cox, H., R. M. Zeskind, and M. M. Owen, 1987: Robust Adaptive Beamforming, *IEEE Trans. Acoust., Speech, Signal Processing*, Vol. ASSP-35, pp.1365–1376, Oct.

- Chu, Y, and W. Fang, 1999: A novel wavelet-based generalized sidelobe canceller, *IEEE Trans. Antennas Propagat.*, Vol. 47, pp. 1485–1495.
- Compton, R., 1978: Adaptive array in a spread-spectrum communication-system, *Proc. IEEE*, Vol. 66, No. 3, pp. 289–298.
- Doviak, R. J., J. Goldhirsh and A. R. Miller, 1972: Bistatic-radar detection of high-altitude clear-air atmospheric targets, *Radio Sci.*, Vol. 7, No.11, pp.993–1003.
- Fudge, G. L., and D. A. Linebarger, 1996: Spatial blocking filter derivative constraints for the generalized sidelobe canceller and MUSIC, *IEEE Trans. Signal Process.*, Vol. 44, pp51–61.
- Fukao, S., T. Sato, T. Tsuda, S. Kato, K. Wakasugi, and T. Makihira, 1985: The MU radar with an active phased array system: 1. Antenna and power amplifier, *Radio Sci.*, Vol. 20, No. 6, pp. 1155–1168.
- Fukao, S., T. Sato, T. Tsuda, S. Kato, K. Wakasugi, and T. Makihira, 1985: The MU radar with an active phased array system: 2. In-house equipment, *Radio Sci.*, Vol. 20, No. 6, pp. 1169–1176.
- Fukao, S., M. Inaba, I. Kimura, P. T. May, T. Sato, T. Tsuda and S. Kato, 1988: A systematic error in MST/ST radar wind measurement induced by a finite range volume effect: 1. Observational results, *Radio Sci.*, Vol. 23, No. 1, pp. 59–73.
- Fukao, S., H. Hashiguchi, M. Yamamoto, T. Tsuda, T. Nakamura, M. K. Yamamoto, T. Sato, M. Hagio, and Y. Yabugaki, 2003: Equatorial Atmosphere Radar (EAR): System description and first results, *Radio Sci.*, Vol. 38, No.3, 1053, doi:10.1029/2002RS002767.
- Fukao, S., Coupling Processes in the Equatorial Atmosphere (CPEA): A Project Overview, *J. Meteor. Soc. Japan*, in press.
- Griffith, L. J. and C. W. Jim, 1982: An alternative approach to linearly constrained adaptive beamforming, *IEEE Trans. Antennas Propagat.*, Vol. 30, pp. 27–34.
- Haykin, S., 2001: *Adaptive filter theory, 4th Ed.*, Prentice Hall New York, 995, 2001.
- Haupt, R. L., 2005: Interleaved Thinned Linear Arrays, *IEEE Trans. Antennas Propagat.*, Vol. 53, No. 9, September.
- Haupt, R. L., 1995: Unit Circle Representation of Aperiodic Arrays, *IEEE Trans. Antennas Propagat.*, Vol. 43, No. 10, October.
- Hudson, J. E., 1981: *Adaptive Array Principles.*, London, U.K., Peter Peregrinus.
- Howells, P. W., 1965: Intermediate Frequency Sidelobe Canceller, U.S. Patent No. 3202990.

- Kamio, K., K. Nishimura, and T. Sato, 2004: Adaptive sidelobe control for clutter rejection of atmospheric radars, *Ann. Geophys.*, Vol. 22, No. 11, pp. 4005–4012.
- Lagnus-Hernandez, M. A., and A. Gasull-Llampallas, 1984: An improved maximum likelihood method for power spectral density estimation, *IEEE Trans. Acoust. Speech Signal Process.*, Vol. 32, pp.170–173.
- Li, J., P. Stoica, and Z. Wang, 2003: On Robust Capon Beamforming and Diagonal Loading, *IEEE Trans. Signal Processing*, Vol. 51, No. 7, pp.1702–1715.
- Luce, H, M. Yamamoto, S. Fukao, D. Helal, and M. Crochet, 2001: A frequency domain radar interferometric imaging (FII) technique based on high-resolution methods, *J. Atmos. Solar-Terr. Phys.*, 63, pp. 221–234.
- Palmer, R. D., S. Gopalam, T.-Y. Yu, and S. Fukao, 1998: Coherent radar imaging using Capons's method, *Radio Science*, Vol. 33, No. 6, pp.1585–1598.
- Protat, A., Zawadzki, I, 2000: Optimization of Dynamic Retrievals from a Multiple-Doppler Radar Network, *J. Atmos. Ocean. Tech.*, Vol. 17, pp. 753–760, June.
- Riegler, R. and R. Compton, 1973: Adaptive array for interference rejection, *Proc. IEEE*, Vol. 61, No. 6, pp. 748–758.
- Röttger, J. and R. A. Vincent, 1978: VHF radar studies of tropospheric velocities and irregularities using spaced antenna techniques, *Geophys. Res. Lett.*, 5, pp.917–920.
- Sato, T., and R. F. Woodman, 1982: Spectral parameter estimation of CAT radar echoes in the presence of fading clutter, *Radio Science*, Vol. 17, No. 4, pp.817–826.
- Sato, T., A. Ito, W. L. Oliver, S. Fukao, T. Tsuda, S. Kato and I. Kimura, 1989: Ionospheric incoherent scatter measurements with the middle and upper atmosphere radar: Technique and capability, *Radio Science*, Vol. 24, No. 1, pp.85–98, January–February.
- Sato, T., T. Nakamura and K. Nishimura, Orbit determination of meteors using the MU radar, *IEICE Trans. Commun.*, Vol. E83-B, No. 9, pp. 1990–1995, September, 2000.
- Schmidt, R. O., 1986: Multiple Emitter Location and Signal Parameter Estimation, *IEEE Trans. Antennas Propagat.*, Vol. 34, No. 3, pp. 276–280, March.
- Smaïni, L., H. Luce, M. Crochet and S. Fukao, 2002: An Improved High-Resolution Processing Method for a Frequency Domain Interferometric Imaging (FII) Technique, *J. Atmos. Ocean. Tech.*, Vol. 19, pp. 954–966.

- Steinberg, B. D., 1972: The Peak Sidelobe of the Phased Array Having Randomly Located Elements, *IEEE Trans. Antennas Propagat.*, Vol. AP-20, No. 2, March.
- Steinberg, B. D., 1973: Comparison Between the Peak Sidelobe of the Random Array and Algorithmically Designed Aperiodic Arrays, *IEEE Trans. Antennas Propagat.*, Vol. 21, Issue 3, pp. 366–370, May.
- Steinberg, B. D. and E. H. Attia, 1983: Sidelobe Reduction of Random Arrays by Element Position and Frequency Diversity, *IEEE Trans. Antennas Propagat.*, Vol. AP-31, No. 6, November.
- Takao, K., M. Fujita, and T. Nishi, 1976: An Adaptive Antenna Array under Directional Constraint, *IEEE Trans. Antennas Propagat.*, Vol. AP-24, No. 5. Sep.
- Takao, K., and N. Kikuma, 1986: Tamed Adaptive Antenna Array, *IEEE Trans. Antennas Propagat.*, Vol. AP-34, No. 3, Mar.
- Wang, Y. and W. Fang, 2000: Wavelet-based broadband beamformers with dynamic subband selection, *IEICE Trans. Commum.*, Vol. E83-B, pp. 819-826.
- Widrow, B., P. Mantey, L. Griffith, and B. Goode, 1967: Adaptive antenna systems, *Proc. IEEE*, Vol. 55, No. 12, p. 2143.
- Woodman, R. F., and A. Guillen, 1974: Radar observation of winds and turbulence in the stratosphere and mesosphere, *J. Atmos. Sci.*, Vol. 31, pp. 491–505.
- Woodman, R.F., 1980: High-altitude-resolution stratospheric measurements with the Arecibo 2380-MHz radar, *Radio Sci.*, Vol. 15, No.2, pp.423–430.
- Woodman, R. F., 1985: Spectral moment estimation in MST radars, *Radio Science*, Vol. 20, No. 6, pp.1185–1195.
- Wurman, J., S. Heckman and D. Boccippio, 1993: A bistatic multiple-Doppler radar network, *J. Appl. Meteor.*, Vol. 32, 1802–1814.
- Wurman, J., M. Randall, C. L. Frush, E. Loew, and C. L. Holloway, 1994: Design of a Bistatic Dual-Doppler Radar for Retrieving Vector Winds Using One Transmitter and a Remote Low-Gain Passive Receiver, *Proc. IEEE*, Vol. 82, No. 12, pp. 1861–1872, December.
- Wurman, J, 1994: Vector winds from a single-transmitter bistatic dual-Doppler radar network, *Bull. Amer. Meteorological Soc.*, Vol. 75, pp. 983–994.
- Yang, H. and Ingram, M. A., 1997: Design of partially adaptive arrays using the singular-value decomposition, *IEEE Trans. Antennas Propagat.*, Vol. 45, pp. 843–850.

Yamamoto, M., T. Sato, P. T. May, T. Tsuda, S. Fukao, and S. Kato, 1988: Estimation error of spectral parameters of mesosphere-stratosphere-troposphere radars obtained by least squares fitting method and its lower bound, *Radio Sci.*, Vol. 23, No. 6, pp. 1013–1021.

